LUNDS UNIVERSITET

Study of an electron-muon resonance in a R-parity violating supersymmetric model using ATLFAST-II

by

Genessis M Perez Rivera

A thesis submitted in partial fulfillment for the
Master Degree in Physics

in the
Physics Department
Div. of Particle Physics
Supervisor: Dr. Bernhard Meirose

August 2012

The worthwhile problems are the ones you can really solve or help solve, the ones you can really contribute something to. ... No problem is too small or too trivial if we can really do something about it.

Richard P. Feynman

LUNDS UNIVERSITET

Abstract

by Genessis M Perez Rivera
Supervisor: Dr. Bernhard Meirose

Supersymmetry (SUSY) is one of the best theoretically motivated beyond the Standard Model (BSM) scenarios, and a favored candidate to be discovered by the experiments at the Large Hadron Collider (LHC). The ATLAS collaboration has been extensively searching for SUSY signatures using 2010, 2011 and 2012 data from LHC proton-proton collisions at a center-of-mass energy of 7 TeV and recently at 8 TeV. However, so far no signs of SUSY or any other BSM physics has been found.

Monte Carlo simulation provides a way to design new physics analyses and quantify expected detector performance. The constraints on SUSY models are one of the main reasons for the production of a large number of Monte Carlo simulated samples, as there is the need to increase the analyses sensitivity to more challenging topologies. The simulation of a large number of Monte Carlo samples represents a big challenge in terms of central processing unit (CPU) time consumption and end-user waiting time. Then, it is of extreme importance to find a fast and accurate way to simulate SUSY signal samples. The ATLAS collaboration has been developing a fast simulation package: ATLFast-II, where the above mentioned times are significantly reduced. However, the use of ATLFast-II for signal sample production must be evaluated in a case by case basis and its use is justified only when there is no loss of accuracy in simulating physics objects.

The current work investigates the performance of ATLFast-II in a particular R-parity violating (RPV) SUSY model predicting the existence of a heavy neutral short-lived resonance (a tau sneutrino) that decays to an electron-muon pair with opposite charges. It is the first dedicated study of the performance of ATLFast-II using a RPV SUSY model.

LUNDS UNIVERSITET

Abstract

by Genessis M Perez Rivera
Supervisor: Dr. Bernhard Meirose

Supersymmetri (SUSY) är en av de teoretiskt bäst motiverade modellerna för fysik bortom standardmodellen (BSM), och en lovande kandidat för upptäckt vid Large Hadron Collider (LHC). ATLAS-kollaborationen har utfört omfattande sökningar efter SUSY-signaturer med hjälp av data från proton-proton kollisioner i LHC, tagna under 2010, 2011 och 2012 års tid vid energier på 7 TeV och mer nyligen 8 TeV. Dock har inga tecken på SUSY eller annan BSM-fysik kunnat påvisas än så länge.

Monte Carlo-simuleringar erbjuda en möjlighet att utforma nya analysmetoder och kvantifiera förväntad detektorprestanda. En av de främsta anledningarna till att producera stora mängder Monte Carlo-simulerad data är att kunna sätta starkare gränser på befintliga SUSY-modeller, samt att utveckla analysmetoder som är känsliga för mer utmanande topologier. Detta innebär stora kostnader vad gäller processortid, och kan resultera i lång väntetid fr användaren. Det är därmed av stor vikt att finna en snabb och precis metod för simulering av SUSY-data. ATLAS-kollaborationen har utvecklat ett snabbt simuleringspaket, ATLFast-II, som kraftigt reducerar ovannämnda väntetid. Användning av ATLFas-II för simulering av SUSY-data kan dock endast motiveras om det inte skulle innebära reducerad precision, och slutresultatet måste bedömas från fall till fall.

Det aktuella arbetet undersöker hur väl ATLFast-II presterar för en viss R-paritetsbrytande SUSY-modell som förutsäger existensen av en tung, neutral och kortlivad resonans (en tau-sneutrino) som faller sönder till ett elektron-myonpar med motsatta laddningar. Detta är den första studien av prestandan hos ATLFast-II i en R-paritetsbrytande SUSY-modell.

Acknowledgements

First, I would like to thank God, because when I was needing the strenght to keep going or I was feeling lost I always found the light on my way. Because when I was feeling desperate and I wanted to give up I found the grace and peace through all the people who surrounded me.

I would like also to thank my home university, Simon Bolivar University, because without them I would not be here doing my project and also thank Lund University for welcoming and giving me the chance to be part of this.

I am truly indebted and heartily grateful to my supervisor, Bernhard Meirose, who gave me the opportunity to work with him and to discover a whole new world in physics. This would not be possible without him, his advices and support. Besides I owe sincere and earnest thankfulness to Anders Floderus who was always there to help me along my months working in this project together with my supervisor, and who was always patient to explain the small details.

I would like to thank all the persons in the High Energy Physics Department, because they supported me through this process and gave me the opportunity to be part of the group, and I am truly thankful. Also, I would like to show my gratitude with people on ATLAS experiment who helped me to meet my goals, and specially I thank Dongliang Zhang, Micheal Duehrssen-Debling, Xavier Portell Bueso and Shimpei Yamamoto.

But nothing of this would be possible without the truly support of my Mother and my Grandmother, they have been with me in every step: thank you for being there always helping me to keep my head up and keep walking.

I am obliged to many of my friends who have supported me in Sweden and in Venezuela, to Fernando Febres Cordero who helped me when I need to work with my project back in Venezuela, and every one of those persons who have been walking by my side during all these years.

Thank you all for your support.

Contents

List of Figures

List of Tables

Nomenclature

AF-I	**A**TL**F**ast-I Simulation
AF-II	**A**TL**F**ast-II Simulation
AMI	**A**TLAS **M**etadata **I**nterface. Tool to find datasets and obtain detailed information on them
AOD	**A**nalysis **O**bject **D**ata. Reduced size output of physics quantities from the reconstruction
Athena	ATLAS offline software framework
ATLFAST	Software package for fast particle-level simulation
Barrel	The central-rapidity region of the ATLAS detector
Beam 1	the LHC beam which rotates clockwise when seen from above. In ATLAS it goes from positive z to negative z
Beam 2	The LHC beam which rotates anti-clockwise when seen from above. In ATLAS it goes from negative z to positive z
B-Layer	The innermost layer of the Pixel detector
C++	Primary programming language used in ATLAS
CA	Certification Authority (Grid)
Calorimeter cell	The smallest unit of calorimeter information to be read out
CERN	European Laboratory for Particle Physics
CMT	**C**onfiguration **M**anagement **T**ool. Use for building software releases, package dependency management, and setup of the run-time environment
DF	**D**ata **F**low System. All software and hardware required for the management, transportation and monitoring of physics data
DPD	**D**erived **P**hysics **D**ata
ECal	Liquid Argon **E**lectromagnetic **Cal**orimeter

EDM	**E**vent **D**ata **M**odel
EMB	Liquid Argon **E**lectro**m**agnetic **B**arrel Calorimeter
EMEC	Liquid Argon **E**lectro**m**agnetic **E**ndCap **C**alorimeter
endcaps	The high-rapidity regions of the ATLAS detector
ESD	**E**vent **S**ummary **D**ata
event	The data resulting from a particular bunch crossing
fullSim	**full** Geant4 **Sim**ulation
Gaudi	Data Processing Applications Framework. Originally developed by and share with LHCb experiment
GEANT	Pan-European Gigabyte Research and Education Network
Geant4	A general Monte Carlo simulation package for describing detector geometry and tracking particles through detector material
GUI	**G**raphical **U**ser **I**nterface
HCal	**H**adronic **Cal**orimeter
HEC	Liquid Argon **H**adronic **E**ndcap **C**alorimeter
HEP	**H**igh **E**nergy **P**hysics
HERWIG	A MC package for simulating **H**adron **E**mission **R**eactions **w**ith **I**nterfering **G**luons
ID	**I**nner **D**etector
LAr	**L**iquid **Ar**gon, Liquid Argon Calorimetry
LHC	**L**arge **H**adron **C**ollider
MC	**M**onte **C**arlo Simulation
POOL	Pool of persistent Objects for LHC
PV	**P**rimary **V**ertex
PYTHIA	A MC program used to generate simulated proton-proton interactions for various physics processes
PANDA	**P**roduction **AN**d **D**istributed **A**nalysis System
Python	An interpreted, interactive, object-oriented, open-source programming language
Raw Data	Data provided by the front-end electronics to the readout buffer
RDO	**R**aw **D**ata **O**bject
ROOT	A class library for data analysis
RPC	Supersymmetric **R**-**P**arity **C**onservation Model

RPV	Supersymmetric **R**-**P**arity **V**iolating Model
SCT	**S**emiconductor **T**racking **D**etector
SDO	**S**imulation **D**ata **O**bjects
SIM	**Sim**ulated Data, in RAW Format
SUSY	**SU**per**Sy**mmetries
TAG	Event-level metadata
TileCal	**Tile Cal**orimeter
TRT	**T**ransition **R**adiation **T**racker of the Inner Detector
UI	**U**ser **I**nterface

To my family

Chapter 1

Introduction

The Standard Model (SM) of particles is one of the successful theories in physics, which describes the fundamental particles and their interactions. Though it gives a description of nearly all the phenomena known in particle physics nowadays, it is conceptually incomplete: it still has a lot of questions to be answered and understood, which makes one think that a greater description of nature is needed, and it remains to be discovered.

Different models beyond the Standard Model have emerged, but one of the most successful theoretically motivated is Supersymmetry (SUSY), a hypothetical symmetry of nature, which has become a favoured candidate to be discovered by the experiments at the Large Hadron Collider (LHC) at CERN. This symmetry predicts for each known particle of the Standard Model a partner called "superpartner", and it will exist with identical quantum numbers but differing by half a unit of spin. Supersymmetry transformation turns a boson (or bosonic state) into a fermion (or fermionic state), and vice versa, by an operator acting over each state.

Supersymmetric signatures have been searched by the ATLAS collaboration using data from proton-proton collisions at a center-of-mass energy of 7 TeV and nowadays 8 TeV, but with no greater success. This has led to doubt about which SUSY models are favoured to be discovered at the experiments, and various theories have appear as an answer to the SUSY searches in the colliders.

Certain theories refer to the existence of a parity called "R-Parity" [1], which allows a more realistic description of the supersymmetric Lagrangian and implies a violation of the baryonic number and the leptonic number at the same time.

In the Minimal Supersymmetric Standard Model (MSSM) [2], the R-parity could be conserved or violated; none of them is theoretically favoured over the other. However,

the choice of one of them has several differences on the expected signals at the experiments. The conservation of the R-Parity, with respect to R-Parity violation, involves large imbalance in the momentum conservation (called missing transverse momentum), multiple relatively high energetic jets and the possible presence of leptons of relatively high transverse momentum. The early strategy for SUSY searches was heavily dedicated to RPC SUSY, but the absence of any experimental signals put significant constraints on it, imposing new challenges for future.

Monte Carlo simulation provides a way to design new physics analyses and quantify expected detector performance; and due to the constraints on many SUSY models a large number of Monte Carlo (MC) simulated samples are requested by the ATLAS SUSY Working Group [3]. But, the simulation of a large number of MC samples implies a challenge in terms of central processing unit (CPU) time consumption and end-user waiting time. So it becomes of extreme importance to consider the simulation using fast detector simulation tools, where the samples must be produced in less time but with same accuracy.

One of the main motivations of this study is that, although a dedicated study testing the suitability of ATLFAST-II within the minimal supergravity (mSUGRA) SUSY framework (assuming R-parity conservation) was performed in ATLAS [4], no dedicated study of the performance of ATLFAST-II in the context of a RPV SUSY model has been made before. The important difference in a RPV SUSY model compared to a RPC SUSY model with respect to ATLFAST-II use is the absence of large missing transverse momentum. This is a very important difference because in the Standard Model the tails of the distributions are important and this is usually difficult to model. However the "bulk" of RPC SUSY will fall at high missing transverse momentum, so if one describes well the bulk of the distribution, this is acceptable. The tails add information but usually less and given that we are dealing with low cross sections, the bulk is what counts the most. For RPV SUSY (without many neutrinos, as it is the case of the model investigated in this thesis) there is no high missing transverse momentum and tails could be of importance as its distributions would be more similar (w.r.t. RPC SUSY) to the Standard Model ones. Given the fact that tails of distributions (as it will be explained in chapter 6) is where ATLFAST-II encounters its most difficulties, this makes a dedicated study of RPV SUSY using ATLFAST-II of the highest importance.

The specific objective of the thesis is to investigate the performance of ATLFAST-II in a particular RPV SUSY model predicting the existence of a heavy neutral short-lived resonance [1] (the tau sneutrino) that subsequently decay to an electron-muon pair with opposite charges. One advantage of this model is the clean signature it predicts. The invariant mass distribution of the electron-muon pair should unmistakeably show a

clear peak at the tau sneutrino mass. A study using full detector simulated samples for this model was performed by the ATLAS collaboration [5] using data collected between March and June 2011.

Chapter 2

The Standard Model of Particle Physics

In modern particle physics the main focus is the study of elementary particles[1]. The term "elementary particle" is used to define a particle without substructure: it is not made up from smaller particles. Then the elementary particles must be the fundamental building blocks of nature out of which all other particles are formed. Any theory of elementary particles must be consistent with special relativity, and it will be a combination of quantum mechanics, electromagnetism and special relativity.

The theories which describe the particles and their interactions seem to be gauge theories, a special class of quantum theories where there is an invariance principle that necessarily implies the existence of interaction mediated through an exchange of particles called gauge bosons. Then, the gauge forces are those which respect the gauge symmetry, and in addition, forces whose strengths are proportional to a "charge" of some kind.

This could be intuitively explained [6]: suppose various particles which can interact with one another, and a push is given to one of them. The forces, due to that particle, that act on nearby particles cannot produce instantaneous changes in their motions, since no signal can travel faster than the speed of light. Instead, it is possible to say the pushed particle is the source of various fields which carry energy through the surrounding space; and eventually the field interacts with other particles. Because of the quantum theory, the energy (and perhaps other quantum numbers) is carried by discrete quanta, which become identified with the particles transmitting the force. Thus in quantum field theory, the elementary particle interactions are interpreted in terms of exchanges of (some of the) particles themselves.

[1] Considering the wave-particle duality, this is a misnomer

To understand the structure of the natural universe, it could be considered a three part problem: first, to identify the basic particles that are the constituents of matter; second, to know what forces those particles feel and third, to understand the behaviour of the particles given the forces.

2.1 Fundamental particles and interactions

2.1.1 Fundamental interactions

The interactions known so far are four: **gravity**, which acts over all particles; **electromagnetism**, which acts on all electrically charged particle; **weak interaction**, which acts over all the fermions and some gauge bosons; and **strong interaction** which acts over all particles with some kind of charge called colour.

FIGURE 2.1: The fundamental forces.

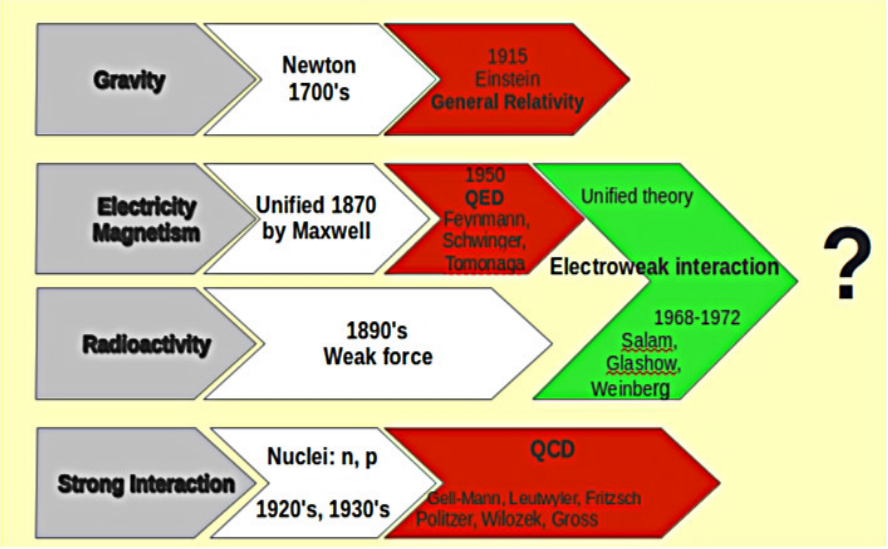

Weak interactions are observed to exist explaining physics phenomena that would not occur if only gravitational and electromagnetic interactions existed; e.g., neutron decay ($n \rightarrow pe\bar{\nu}$). Those interactions play a critical role in the process of hydrogen fusion in starts, it is responsible for the radioactive decay of subatomic particles and also in the building up of heavy elements.

Nuclear forces have been known for longer, since a nucleus containing several protons would hold together in spite of their electrical repulsion, another force (attractive) stronger than electromagnetism must exist. The strong interaction has explained this with the existence of quarks, the force between quarks is called *colour* force. The quarks carry the colour charge and they combine to make colour neutral hadrons.

Even when four types of interaction field have been distinguished in nature, on the scales of particle physics, gravitational forces (so far) are insignificant. The theory of weak interactions and electromagnetic interactions have been unified into one, the electroweak theory. And the success of this unification has encouraged scientists to try to unify the electroweak theory and QCD into one unified theory.

2.1.2 The Fundamental particles

In general terms, the particles can be put into two categories, matter particles and gauge bosons.

Quarks and leptons are the fundamental objects of which all matter is composed, thereby they are called **the matter particles**. They interact via the exchange of gauge bosons. The forces that significantly affect them are the unified electroweak force, whose gauge bosons are the photon and the $W^{\pm}$ and Z^0 bosons, and the strong force. The theory of the strong force is called quantum chromodynamics (QCD), and the gauge bosons of the strong force are the (eight) gluons.

The Matter Particles

Quarks and leptons belong to the fermionic part of the Standard Model (SM), and it consists of twelve fermions categorised into three generations: particles from the first generation are the lightest and do not decay, hence all ordinary (baryonic) matter is made of such particles. Second and third generation charged particles decay with very short half lives and are observed only in very high-energy environments[2].

Generation	Leptons		Quarks	
1st	e	ν_e	u	d
2nd	μ	ν_μ	c	s
3rd	τ	ν_τ	t	b
Electromagnetic charge	-e	0	$\frac{2}{3}$e	$-\frac{1}{3}$e

TABLE 2.1: The quarks generations and their electric charge in terms of the magnitude of the electron's charge (e); and the leptons generations and their electric charge.

Quarks can be interpreted as a fermion that carries the colour charge of QCD, while a lepton is a fermion with no colour charge. There are six kinds ("flavors") of quarks and six kinds ("flavors") of leptons. Both have spin $\frac{1}{2}$.

[2] An exception to these generations are the neutrinos, which are stable but only interact weakly.

The quarks flavors are called (for historical reasons): up (u), down (d), strange (s), charmed (c), bottom (b) and top (t). And each quark flavor comes in three colours: red (r), green (g) and blue (b).

The leptons flavors are also six, and it is believed that leptons preserve electric charge. As the separate lepton types do not undergo transitions into one another, then lepton number can be defined for each family and it has been observed experimentally to be conserved[3], though the fundamental reasons are not known yet. Leptons do not carry colour, they do not participate in strong interactions.

The Gauge Bosons

The quanta of the electromagnetic (EM) interaction field between electrically charged fermions are the massless photons. The quanta of the weak interaction fields between fermions are the charge W^+ and W^- bosons and the neutral Z^0 boson. Since these carry mass, the weak interaction is short ranged ($\sim 10^{-3}\ fm$). The quanta of the strong interaction field, the gluons, have zero mass and, like photons, might expected to have infinite range. But, unlike the EM field, the gluons are confined. The gluons were predicted to exist, but they were not observed until 1979 at the electron-positron collider in Hamburg.

In addition to the quarks, leptons and gauge bosons, it turns out that one more class of particle is needed to make a consistent theory of particle masses and interactions, the spin-zero or scalar boson called Higgs boson. Detecting them experimentally and understanding their properties is the major remaining gap in the electroweak theory. In July 2012 announcements from CERN about the discovery of a new heavy particle which signature is consistent with a Higgs-like particle [7].

In the current work, the physical constants to be used are in the *natural units*: Speed of Light, $c = 3 \times 10^8$ ms^{-1} $= 1$. And reduced Planck constant, $\hbar = 6.6 \times 10^{-16}$ eV s $= 1$.

2.2 Symmetries: Noether's Theorem

Symmetries have always played an important role in the development of physics. Not only have they provided a useful tool when deriving solutions to a specific problem but additionally the *Noether's theorem* establishes that symmetries implies conservation laws.

[3] There is an exception to this rule, and it is applied to neutrinos. They do not respect family number conservation.

The importance of Noether's theorem leads on the fact that whenever there is an invariance of the theory under some transformation for a system described by a Lagrangian, a conserved current arises and can be written down in terms of appropriate derivatives of the Lagrangian: thus if there is a symmetry, there is a conserved quantity; and vice versa, if there is a conserved quantity observed, there is an associated symmetry.

2.3 The Standard Model Lagrangian

2.3.1 Internal symmetries of the theory

In order to describe the particles and interactions known, three internal symmetries are needed: $U(1)_Y \otimes SU(2)_L \otimes SU(3)_C$.

All particles appear to have $U(1)$ invariance [6], or phase invariance. This is related to the *electromagnetic interaction*. The gauge boson required will be called B^μ, where B^μ transforms under spatial rotations the same way the ordinary derivative ∂^μ does. Y refers to the generator of $U(1)$ transformations, and it is a constant[4] called the $U(1)$ hypercharge generator.

All particles also appear to have a second internal invariance [6], under a set of transformations that form an $SU(2)$ group. The associated gauge boson necessary to maintain the invariance of the theory are called W_i^μ[5]; as the generators of the $SU(2)$ are three, it must exist three gauge bosons related therefore i=1,2,3.

A third internal invariance [6] that all particles appear to have are under a set of transformations that form an $SU(3)$ group. The associated gauge boson are labelled g_a^μ, where a = 1,2,..., 8 since there is one spin-one boson for each of the eight generators of $SU(3)$.

Knowing all the local gauge symmetries of the theory, now it is possible to write the covariant derivative[6] of the Standard Model.

[4] This constant differs for different fermions.

[5] Here μ is a label for space-time transformations.

[6] A covariant derivative is an equation similar to Schrödinger equation, which is invariant under gauge transformations. The covariant derivative are helpful when the Lagrangian of the system is being written, and it is need to be invariant under gauge transformations in all internal spaces [6].

2.3.2 The Lagrangian

The fermion states can be written in terms of their chirality, as a left-handed or right-handed fermion. The Standard Model treats left-handed fermions differently from right-handed fermions. The left-handed and right-handed states transform differently under the electroweak symmetry. Right-handed are electroweak singlets, while left-handed are in electroweak doublets.

Then, for instance it is possible to write the left- and right-handed components of the electron:

$$e_R^- = \text{electroweak singlet} \tag{2.1}$$

$$L = \begin{pmatrix} \nu_e \\ e^- \end{pmatrix}_L \tag{2.2}$$

In analogous way, all fermions can be written in this way. Then, each fermion generation would look like this

$$f = \ L,\ e_R,\ Q_L,\ u_R,\ d_R$$

The Standard Model Lagrangian [6] can be then written for the interaction of quarks and leptons with the gauge bosons, according to the description of the internal symmetries, as

$$\begin{aligned}
\mathcal{L} = & \sum_{f=\nu_e,e,u,d} eQ_f \left(\hat{f}\gamma^\mu f\right) A^\mu \\
& + \frac{g_2}{\cos\theta_\omega} \sum_{f=\nu_e,e,u,d} \left[\bar{f}_L\gamma^\mu f_L \left(T_f^3 - Q_f \sin^2\theta_\omega\right) + \bar{f}_R\gamma^\mu f_R \left(-Q_f \sin\theta_\omega\right)\right] Z_\mu \\
& + \frac{g_2}{\sqrt{2}} \left[\left(\bar{u}_l\gamma^\mu d_L + \bar{\nu}_{eL}\gamma^\mu e_L\right) W_\mu^+ + \left(\bar{d}_L\gamma^\mu u_L + \bar{e_L}\gamma^\mu \nu_{e_L}\right) W_\mu^-\right] \\
& + \frac{g_3}{2} \sum_{q=u,d} \bar{q_\alpha}\gamma^\mu \lambda^a_{\alpha\beta} q_\beta G^a_\mu
\end{aligned} \tag{2.3}$$

where Q_f is the electric charge of the fermion, T_f^3 is the weak isospin term $(0,\ \pm\frac{1}{2},\ 1)$ and θ_ω is the electroweak mixing angle. Further, g_2 and g_3 are the strength coupling constants.

2.4 Beyond the Standard Model

Though the SM gives a good description of nearly all the phenomena that are known in particle physics, there are several questions that have not been answered satisfactorily by the SM, and that indicates that more fundamental physics remains to be discovered. Some of the problems that are not conceptually complete follows.

- There are nineteen free parameters in the SM. But those parameters can only be experimentally measured. So, it is unsatisfactory to believe that these parameters can only be determined by measurement. A more elegant theory could predict them.
- $U(1)_Y \otimes SU(2)_L \otimes SU(3)$ local invariance gives a very good match between theory and experiment, but there is not explanation within the SM for this choice.
- The **hierarchy problem** of the SM is the statement that the Higgs mass is unnaturally small. The Higgs boson mass of the Standard Model is unstable to quantum loop corrections and if we consider the SM as an effective theory which is valid to a high energy scale, in order to have a small mass it needs to be extremely fine-tuned.

  To illustrate [8], [9], consider a calculation of the mass of the Higgs boson from the SM Lagrangian. At a first order the Higgs mass is,

  $$m_H = \frac{\sqrt{2}\mu h}{2\pi}$$

  To compute the mass of the Higgs every particle which couples with the Higgs must be included, and the Higgs-fermion coupling takes the form $-\lambda_f H \bar{f} f$. Then, every loop correction for all particles coupling to the Higgs boson is needed. The function to calculate the fermionic contributions gives an integral over all possible momentum states, which diverges quadratically. The integral should be cut-off at an energy Λ, the scale where new physics is expected.

  Then, evaluating for Λ as a fixed value, the Higgs mass under this cut-off would be given by equation 2.4,

  $$\Delta m_H^2 = \frac{|\lambda_f|^2}{16\pi^2}\left(-2\Lambda + 6m_f ln\left(\frac{\Lambda}{m_f}\right) + \dots\right) \tag{2.4}$$

  where m_f is the mass of the fermion in the loop, and λ_f the Higgs fermion coupling. Λ is related with the Planck scale, where gravitation effects become strong and which value is $\mathcal{O}(10^{19} GeV)$. Then the mass correction to the order of the Planck

scale will be in the order of $\approx (10^{19}\ GeV)$ when the SM requires $m_H \lesssim \mathcal{O}$ (1 TeV) as upper limit. Then the correction is not acceptable, and because of the extreme difference in the energy (hierarchy) is called the hierarchy problem of the Standard Model.

Then it is reasonable to think that the SM is incomplete.

Chapter 3

Supersymmetry (SUSY)

3.1 The Minimal Supersymmetric Standard Model

Supersymmetry is a symmetry which relates fermions and bosons, and it appears as an answer to the "hierarchical problem" of the Standard Model (SM). A supersymmetry transformation turns a bosonic state into a fermionic state, and vice versa. Then, it must exist and operator, Q, such that

$$\begin{aligned} Q|\text{Boson}> &= |\text{Fermion}>, \\ Q|\text{Fermion}> &= |\text{Boson}> \end{aligned} \tag{3.1}$$

The operator Q is a anticommuting spinor, then its hermitian conjugated $Q^\dagger$ is also a symmetry generator. As Q and $Q^\dagger$ are fermionic operators they carry spin angular momentum $\frac{1}{2}$ and therefore that supersymmetry must be a space-time symmetry.

In a theory, as SM, with chiral fermions, the possible forms for these symmetries are restricted to generators Q and $Q^\dagger$ which satisfy the following algebra of anticommutation and commutation relations

$$\begin{aligned} \{Q, Q^\dagger\} &= P^\mu \\ \{Q, Q\} = \{Q^\dagger, Q^\dagger\} &= 0 \\ [P^\mu, Q] = [P^\mu, Q^\dagger] &= 0 \end{aligned}$$

where P^μ is the four-momentum generator of space-time translations.

The single-particle states of a supersymmetric theory fall into irreducible representations of the supersymmetry algebra, called supermultiplets. Each supermultiplet contains both fermion and boson states, which are commonly known as superpartners of each other [2]; that is, if two states are members of the same supermultiplet,for instance $|\Omega>$ and $|\Omega'>$, one of them is proportional to a combination of Q and $Q^\dagger$ acting on the other state (and vice versa).

Then members of the same supermultiplet have the following inherent properties [2],

- The squared-mass operator P^2 commutes with the operators Q, $Q^\dagger$ and with all space-time rotation and translation operators; it ensures that particles in the same irreducible supermultiplet have equal eigenvalues of P^2, and therefore equal masses.
- The Q, $Q^\dagger$ operators commute with all the generators of gauge transformations, then all the states in a supermultiplet are in the same representation of the gauge group, and must have same electric charges, weak isospin and colour degrees of freedom.
- Each supermultiplet contains an equal number of fermion and boson degrees of freedom.

A supersymmetric extension of the SM includes each of the known fundamental particles and assigned them to supermultiplets, with a superpartner with spin differing by $\frac{1}{2}$ unit. The spin-0 partners of the SM are called in the same way as in the SM, but prepending an "s", for scalar; then they are called squarks and sleptons, and even sometimes sfermions. Both the left-handed and right-handed quarks and leptons must have a superpartner; and they are still labelled by the handedness of their standard model counterpart, for instance a left-handed labelled slepton does not refer to the helicity of the slepton, they are spin-0 particles. These supermultiplets are called chiral or matter supermultiplets.

Squarks and sleptons use the same symbols as the quarks and leptons, but they differ by drawing a $\sim$ over the top of the symbol (Table 3.1).

The partner of the SM gluon is called a gluino, and it has spin $\frac{1}{2}$, while the partner of the SM $W^\pm$ are the winos; the partners of the SM gauge bosons are also a representation of the gauge group, and they are called gauginos.

In a supersymmetric extension of the SM, each of the known fundamental particle is therefore in either a chiral or a gauge supermultiplet, and must have a superpartner with spin differing by $\frac{1}{2}$ unit. Then, each particle fits into a supermultiplets according with its SM properties:

Particle	Supersymmetric Partner	Spin of the partner	Name
e_L	$\tilde{e}_L$	0	selectron
u_R	$\tilde{e}_R$	0	up squark
ν_μ	$\tilde{\nu}_\mu$	0	muon sneutrino
	$\vdots$		
γ	$\tilde{\gamma}$	$\frac{1}{2}$	photino
g	$\tilde{g}$	$\frac{1}{2}$	gluino
	$\vdots$		

TABLE 3.1: Supersymmetric States.

- Only chiral supermultiplets can contain fermions whose left-handed parts transform differently under the gauge group than their right-handed parts. Then, as all the SM fermions have this property they must be members of chiral supermultiplets.

  It is important to realise that the left-handed and right-handed pieces of the fermions are separate two-component Weyl fermions with different gauge transformation properties in the SM, so each part must have its own complex scalar partner.

- The gauge supermultiplet includes the gauge bosons of the SM. The gauge interactions of each of these sfermion fields are the same as for the corresponding SM fermions: the left sfermion couple to the W boson, while the right does not.

Realistic description of the SM in a supersymmetric extension must contain supersymmetry breaking; theoretically if supersymmetry exists at all, should be an exact symmetry that is broken spontaneously [2]; then the model should have a Lagrangian density invariant under supersymmetry, but a vacuum state that is not.

If the supersymmetry is not broken at all, every of the quarks, leptons and gauge bosons would have a partner that will only differ in spin but otherwise will be identical. Then, it would be possible to find selectrons, e.g., with masses exactly equal to the SM electron. Since no supersymmetric particle has yet been discovered this is not possible.

The Minimal Supersymmetric Standard Model (MSSM) is the SM extension which adds the minimum extra particle content to the SM.

Unbroken supersymmetry guarantees a lot of information needed, so it is considered a "soft" supersymmetry breaking. That means that the effective Lagrangian of the MSSM could be written like

$$\mathcal{L} = \mathcal{L}_{SUSY} + \mathcal{L}_{SOFT} \tag{3.2}$$

where $\mathcal{L}_{SUSY}$ contains all of the gauge and Yukawa interactions and preserves supersymmetry invariance, and $\mathcal{L}_{SOFT}$ violates supersymmetry but contains only mass terms and coupling parameters with positive mass dimension.

The possible soft supersymmetry-breaking terms in the Lagrangian of a general theory are [2]:

$$\mathcal{L}_{SOFT} = \left(-\frac{1}{2}M_a\lambda^a\lambda^a + \frac{1}{6}a^{ijk}\phi_i\phi_j\phi_k + \frac{1}{2}b^{ij}\phi_i\phi_j + t^i\phi_i\right) + C.C. - (m)^i_j\phi^{j*}\phi_i \tag{3.3}$$

where M_a are gaugino masses for each gauge group, scalar squared-mass terms $(m)^i_j$ and b^{ij}, and (scalar) couplings a^{ijk} and c^{jk}_i and tadpole[1] t^i.

The MSSM Superpotential

The superpotential for the MSSM is given by

$$W_{MSSM} = \bar{u}\mathbf{y_u}QH_u - \bar{d}\mathbf{y_d}QH_d - \bar{e}\mathbf{y_e}LH_d + \mu H_uH_d \tag{3.4}$$

The objects H_u , H_d , Q, L, u, d, e are chiral superfields corresponding to the chiral supermultiplets in Table 3.2. The dimensionless Yukawa coupling parameter y_u, y_d, y_e are 3x3 matrices in family space, identical to those of the standard model and μ a constant [2]. This superpotential (equation 3.4) is minimal in the sense that it is sufficient to produce a phenomenologically viable model; however, additional gauge invariant terms could be added to this potential, but these are terms which violate either baryon or lepton number [8].

3.1.1 R-Parity Supersymmetric models

The conservation of the baryon (B) and lepton (L) number in the Standard Model is not assumed, but a consequence of the fact that there are no possible renormalizable Lagrangian terms that violate them, and it has not been seen experimentally B- and L-violating processes. In fact, the non-observation of proton decay, which violates both B and L by 1 unit, is the most obvious experimental constraint.

[1] Tadpole is a one-loop Feynman diagram with one external leg coupling

Particle Names		Spin 0	Spin $\frac{1}{2}$	$SU(3)_C, SU(2)_L, U(1)_Y$
Squarks, quarks	Q	$(\tilde{u_L}, \tilde{d_L})$	(u_L, d_L)	$(3,2,\frac{1}{6})$
	$\bar{u}$	$\tilde{u_R^*}$	$u_R^\dagger$	$(\hat{3}, 1, -\frac{2}{3})$
	$\bar{d}$	$\tilde{d_R^*}$	$d_R^\dagger$	$(\hat{3}, 1, \frac{1}{3})$
Sleptons, leptons	L	$(\tilde{\nu}, \tilde{e_L})$	(ν, e_L)	$(1,2,-\frac{1}{2})$
	$\bar{e}$	$\tilde{e_R^*}$	$e_R^\dagger$	$(1,1,1)$
Higgs, Higgsinos	H_u	(H_u^+, H_u^0)	$(\tilde{H_u^+}, \tilde{H_u^0})$	$(1,2,\frac{1}{2})$
	H_d	(H_d^0, H_d^-)	$(\tilde{H_d^0}, \tilde{H_d^-})$	$(1,2,\frac{1}{2})$
Particle Names		Spin $\frac{1}{2}$	Spin 1	$SU(3)_C, SU(2)_L, U(1)_Y$
gluino, gluon		$\tilde{g}$	g	(8,1,0)
Winos, W bosons		$\tilde{W^\pm}$, $\tilde{W^0}$	$W^\pm$, W^0	(1,3,0)
Bino, B boson		$\tilde{B^0}$	B^0	(1,1,0)

TABLE 3.2: Particle content and supermultiplets in the Minimal Supersymmetric Standard Model.

FIGURE 3.1: Proton decay as a consequence of baryon and lepton number violating. The process shows a $p \to e^+\pi^0$ mediated by a squark (strange or bottom).

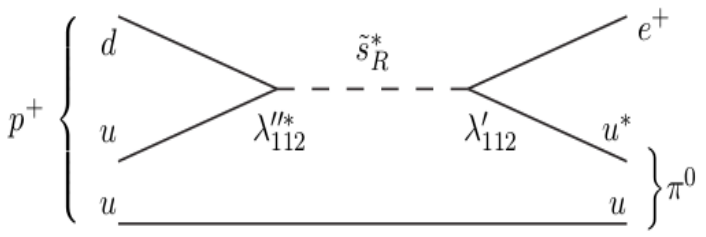

The idea of a most general gauge-invariant and renormalizable superpotential based on Eq. 3.4 would include more terms, but these would violate either baryon or lepton number, and it is clearly a step backward from the SM. Therefore in the MSSM it seems to be necessary to add a new symmetry, which has the effect of eliminating the possibility of B and L violating terms in the renormalizable potential and it will allow good terms. This symmetry is called "R-Parity" [2].

R-Parity is a multiplicative conserved quantum number and it is defined as

$$R_p = (-1)^{3B-L+2S} \tag{3.5}$$

where B, L and S are respectively the baryon number, the lepton number and the spin of particles. All the Standard Model particles and the Higgs bosons have even R-parity,

while their supersymmetric partners (the squarks, sleptons, gauginos and higgsinos) have odd R-parity.

If R-parity is exactly conserved, there cannot be mixing between the sparticles and the SM particles, and then some important phenomenological implications arise [2]:

- The lightest sparticle with R_p = -1 is called the *lightest supersymmetric particle* (LSP) and it must be absolutely stable.
- Each sparticle other than the LSP must eventually decay into a state that contains an odd number of LSPs.
- In collider experiments, sparticles can only be produced in even numbers.

R-parity is often assumed to be conserved, decision motivated phenomenologically by proton decay constraints and looking for the LSP to be a good dark matter candidate[2]; but, there is not compelling theoretical reason for this assumption while a violation of the R-parity seems to be more interesting.

3.1.2 R-Parity violation in a Supersymmetric model

The assumption of R-parity conservation (RPC) because of proton decay leads to expects if R-parity is violated, then in the renormalizable Lagrangian either B-violating or L-violating couplings are allowed, but not both at the same time. Then, an alternative discrete symmetry could forbid proton decay at the level of the renormalizable Lagrangian.

But, if R-parity is violated important consequences in the searches for supersymmetry are present; while R-parity violating (RPV) does not allow proton decay through alternative symmetries, it does allow the LSP to decay and any other heavier sparticle. Then, heavier sparticles will usually decay to final states containing the LSP, as in RPC, but the LSP will decay into Standard Model fermions. The signatures to be found will depend on the constraints of the R-parity violation.

In general representations of a gauge invariant and renormalizable superpotential, R-parity violation could be included as:

$$W_{R_p} = \frac{1}{2}\lambda^{ijk} L_i L_j \bar{e_k} + \lambda'^{ijk} L_i Q_j \bar{d_k} + \frac{1}{2}\lambda''^{ijk} \bar{u_i} \bar{d_j} \bar{d_k} + \mu'^{i} L_i H_u \tag{3.6}$$

[2]If the LSP is electrically neutral it will interact only weakly with ordinary matter, and this seems to be an attractive candidate for the non-baryonic dark matter.

where the additional terms added to the superpotential are the baryon and lepton number violating terms. L and Q are the lepton and quark SU(2) doublet superfields; e, d and u denote the singlet fields for charged leptons, down and up quarks (respectively) and μ, λ, λ' and λ'' are couplings (the last three are the dimensionless Yukawa coupling constants). All these terms violate either L- or B-symmetry, and the terms that may produce both number violation simultaneously are forbidden in the superpotential to ensure the stability of the proton.

Signals with L-violating LSP decays will include charged leptons or large missing energy, or both always. Another possibility will be a sparticle (slepton or sneutrino), that is not the LSP, could decay directly to Standard Model quarks and leptons if the RPV couplings are large enough.

Resonant Sneutrino in a RPV Model

The current work will study the decay of a sneutrino in a RPV Model; then accordingly with the R-parity violation consequences explained in 3.1.2, it is expected as a result a decaying into Standard Model particles.

The motivation is to find a signature related with a tau sneutrino decaying into an electron-muon pair. Then, the search focuses specifically on the tau sneutrino (and anti-sneutrino) because their RPV couplings are less constrained by experiments.

The ATLAS Collaboration in [10] explains that "strong limits on RPV couplings have been obtained from low-energy searches [1], [11], where superparticles appear in the intermedia state, often in loops". But due to "the presence of multiple interfering amplitudes" the extraction of limits is difficult and "it is usually assumed that a single product of couplings dominates".

FIGURE 3.2: Feynman diagram of sneutrino production and decay at LHC.

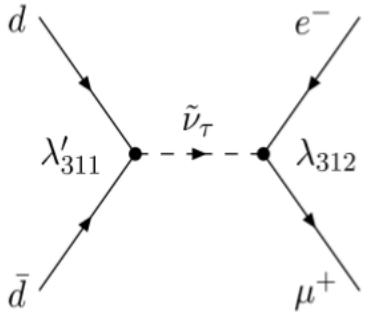

A more complete study about the sneutrino decay could be found in [1].

Chapter 4

The ATLAS Experiment

4.1 The Large Hadron Collider

The CERN Large Hadron Collider (LHC) is a two-ring, superconducting particle accelerator and collider located on the French-Swiss border near Geneva (Figure 4.1), which has been designed to collide 7 TeV protons together with a centre of mass energy of $\sqrt{s}$ = 14 TeV, and to reach a design luminosity[1] of 10^{34} cm^{-2} s^{-1}. It has been designed to have $\sim 10^{11}$ proton in each bunch crossing, colliding at a rate of 40 MHz.

FIGURE 4.1: LHC. From [12].

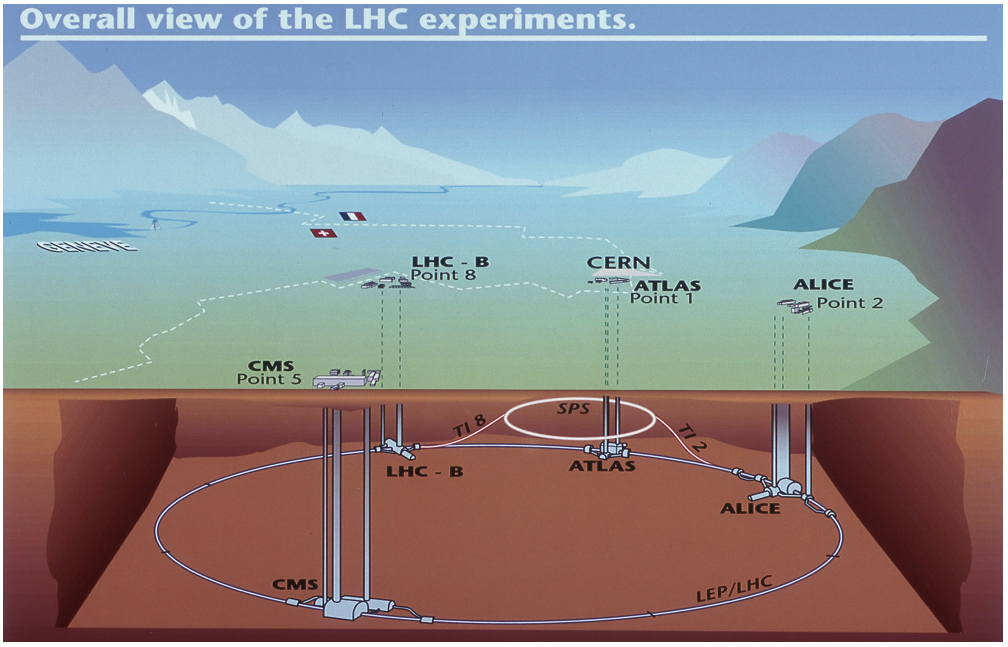

[1]Luminosity is a measure of beam intensity, proportional to the number of interactions of a given type.

The hadron colliders can achieve relatively easily high energy and high luminosity; and the LHC luminosity and the interaction rate are needed because of the small cross-sections expected for many potentially new processes in particle physics.

The protons are initially accelerated by the LINear ACcelerator 2 (LINAC2) to an energy of 50 MeV, and to a 31.4% of the speed of light. Then, the protons are injected into the Proton Synchrotron (PS) Booster. The PS Booster accelerates them to an energy of 1.4 GeV and a velocity that is 91.6% the speed of light. The PS Booster then feeds into the Proton Synchrotron (PS), which was CERN's first synchrotron. The PS accelerates the protons to an energy up to 20 GeV, and a velocity that is 99.93% the speed of light. The PS injects the protons into the Super Proton Synchrotron (SPS), which accelerates protons to an energy of 450 GeV with a velocity of 99.9998% the speed of light. The SPS then injects the proton beams directly into the LHC [13]. The CERN accelerator complex is shown in Figure 4.2. To keep the beam focused and to control the acceleration around the LHC ring, it is employed over 1300 dipole magnets (8.3 T), each cooled by a bath of superfluid helium (1.9 K), and 392 quadrupole magnets [8].

FIGURE 4.2: Cern Accelerator Complex [14].

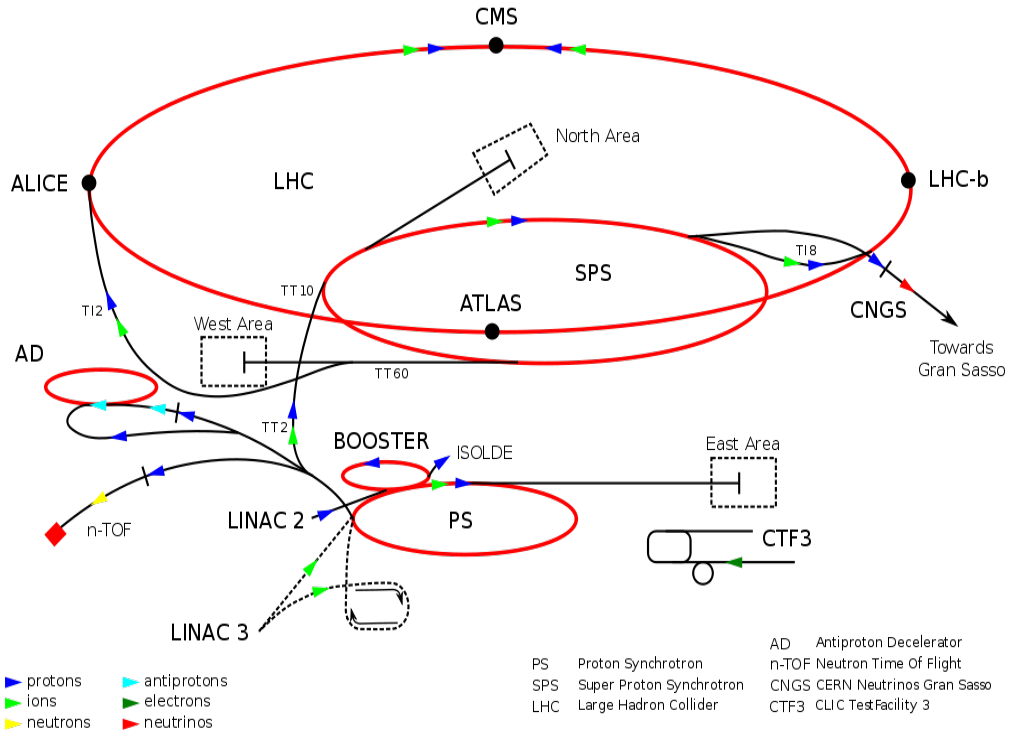

Then the beams are forced into collision at four points along the LHC experiment ring (Figure 4.1 and Figure 4.2), each point houses its own experiment. Two of them, ATLAS (A Toroidal LHC ApparatuS) and CMS (Compact Muon Solenoid), are experiments searching for new physics. A third one, LHCb (Large Hadron Collider beauty experiment) is searching for new physics in b-decays and making precision measurements of

CP violation; and the last experiment, ALICE (A Large Ion Collider), is a heavy-ion experiment investigating the quark-gluon plasma.

The LHC Experiments

- ALICE Experiment [15]: For the ALICE experiment the LHC collides ions to recreate the conditions just after the Big Bang under laboratory conditions. The data obtained allows physicists to study a state of matter known as quark-gluon plasma, which is believed to have existed soon after the Big Bang.
- ATLAS Experiment [16]: It is one of the two general-purpose detectors at the LHC. It investigates different physics phenomena, including the search for the Higgs boson, extra dimensions, and particles that could make up dark matter. ATLAS records sets of measurements on the particles created in collisions (their paths, energies, identities).
- CMS Experiment [17]: It uses a general-purpose detector to investigate a wide range of physics, and it has the same scientific goals as the ATLAS experiment, but it uses different technical solutions and design of its detector magnet system to achieve these. The CMS detector is built around a huge solenoid magnet that generates a magnetic field of 4 Teslas, which is about 100000 times that of the Earth.
- LHCb Experiment [18]: it investigates why the Universe appears to be composed almost entirely of matter, but not antimatter. It specialises in studying the slight differences between matter and antimatter by studying the "beauty quark" (b quark).

4.2 Detector Nomenclature

In order to understand the detectors and their behaviour in this chapter, it is important to explain the nomenclature related to the detector description and used in the current study.

The origin of the coordinate system in the detector is defined by the nominal interaction point, while the beam direction defines the z-axis and the x-y plane is transverse to the beam direction: the positive x-axis points from the interaction point to the centre of the LHC ring, and the positive y-axis points upwards. The azimuthal angle ϕ is measured around the beam axis where $\phi = 0$ corresponds to the positive x-axis and increase clock-wise, and the polar angle θ is the angle from the beam axis.

The pseudorapidity is defined as $\eta = -ln\tan(\theta/2)$, and it is a commonly used to describe the angle of a particle relative to the beam axis. The transverse momentum p_T, the transverse energy E_T, the missing transverse momentum E_T^{miss}, and any other transverse variable, are defined in the x-y plane (transverse plane) unless stated otherwise. The distance ΔR in the pseudorapidity-azimuthal angle space is defined as $\Delta R = \sqrt{\Delta\eta^2 + \Delta\phi^2}$.

4.3 The ATLAS Experiment

The ATLAS experiment is the largest volume particle detector constructed nowadays: its cylindrical shape is formed by different sub-detectors, one solenoidal and one toroidal magnet system, cabling and cooling infrastructure, in a total length of 42 m and a radius of 11 m, weighting approximately 7000 tons.

It consists of four major parts: the inner detector (ID), the calorimeters, the muon system and the magnet system.

FIGURE 4.3: ATLAS detector. From [12].

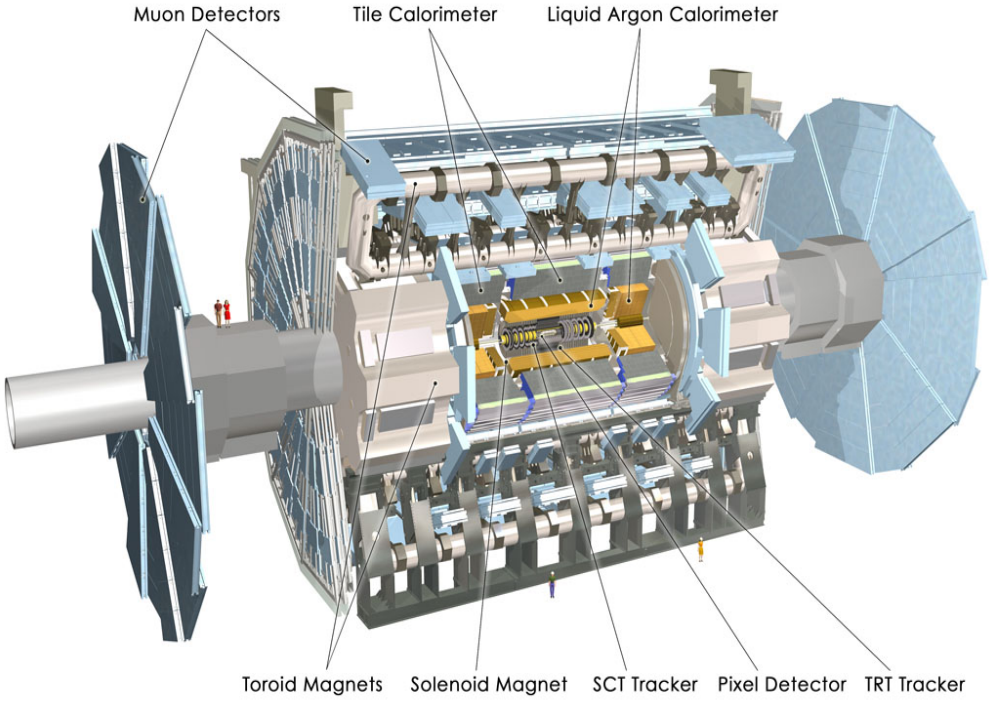

The magnet system creates the azimuthal magnetic field in the detector, and it comprises a thin superconducting solenoid surrounding the inner-detector cavity, and three large superconducting toroids (one barrel and two end-caps) arranged around the calorimeters. The inner detector is then immersed in a 2 T solenoidal field and it is designed to achieve

pattern recognition, momentum and vertex measurements, and electron identification. The calorimeters surround the inner detector: the liquid-argon (LAr) electromagnetic calorimeters cover the pseudorapidity range $|\eta| < 3.2$, while the hadronic calorimetry in the range $|\eta| < 1.7$ is provided by a scintillator-tile calorimeter and in the range $|\eta| > 1.5$, end caps, LAr technology is also used for the hadronic calorimeters. The LAr forward calorimeters provide both electromagnetic and hadronic energy measurements, and extend the pseudorapidity coverage to $|\eta| = 4.9$. The calorimeter is surrounded by the muon spectrometer (muon system).

As a general-purpose detector, requirements for the ATLAS detector system have been set to provide a wide range of physics studies, from precision measurements of Standard Model to uncovering of phenomenon due to new physics. The broad spectrum of processes expected to be studied (e.g. tests of QCD, electroweak interactions) have predetermined the design criteria of the detector as it follows:

- The detectors require fast, radiation-hard electronics and sensor elements. Also high detector granularity is needed to handle the particle fluxes and to reduce the influence of overlapping events [19].
- A large acceptance in pseudorapidity, η, and almost full azimuthal angle, ϕ, coverage everywhere.
- Efficient tracking and precise reconstruction capability of charged tracks in the inner detector, close to the interaction region. It is important for precise vertex determination and offline tagging of b-jets and τ-leptons.
- Precise measurements and identification of physics objects done by electromagnetic calorimetry and hadronic calorimetry are required. These measurements are the basis of many physics studies.
- High precision muon identification and momentum resolution over a wide range in momenta.
- Triggering and measurements of particles at low-p_T with accurate rejection of background.

4.4 The ATLAS detectors

4.4.1 The Inner Detector

The inner-detector (ID) is designed to reconstruct charged particle tracks and vertexes close to the interaction region, contributing to the measurement of the momenta and

charges of the particles it reconstructs. The inner detector combines high-resolution detectors at the inner radii with continuous tracking elements at the outer radii, and it is contained in the central solenoid which provides a nominal magnetic field of 2 T.

FIGURE 4.4: ATLAS Inner Detector. From [12].

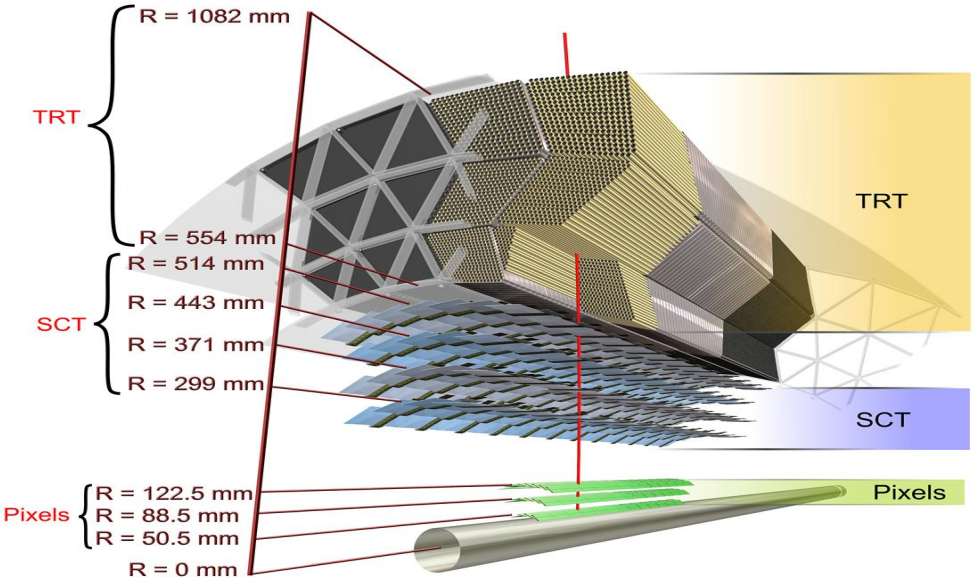

The ID is contained within a cylindrical envelope of length ±3512 mm and of radius 1150 mm. The ID consists of three independent but complementary sub-detectors: a *Pixel Detector*, a *Semiconductor Tracker* and a *Transition Radiation Tracker* (Figure 4.4).

The ATLAS ID has been designed to provide hermetic and robust pattern recognition, excellent momentum resolution and primary and secondary vertex measurements for charged tracks closest to the beam-pipe. The highest granularity detection is needed closest to the beam-pipe to cope with the very large particle track density, while further from the beam-pipe reduced granularity detection suffices, because the particle occupancy is lower.

- Pixel Detector

  This sensor is a wafer of silicon with 46.080 pixels in a area of 16.4 x 60.8 mm and with 50 x 400 microns each. It has been designed to provide a very high-granularity, high-precision set of measurements as close to the interaction point as possible. The system provides precision measurements, and mostly determines the impact parameter resolution [20].

- Semiconductor Tracker (SCT)

  The SCT system is designed to provide eight precision measurements per track in a intermediate radial range, contributing to the measurement of momentum, impact parameter and vertex position. It consists in eight layers of silicon micro-strip detectors; and it covers $|\eta| < 2.5$.

  The detector contains 61 m^2 of silicon detectors, and 6.2 million readout channels. The spatial resolution is 16 μm in $R - \phi$ and 580 μm in z. Tracks could be distinguished if separated by more than $\sim$200 μm.

- Transition Radiation Tracker (TRT)

  Polyimide drift tubes of 4 mm diameter are the basic TRT detector elements [19] . The straw tube wall, especially developed to have good electrical and mechanical properties with minimal wall thickness, is made of two 35 m thick multi-layer films bonded back-to-back.

  It is a combined straw tracker and transition radiation detector. The TRT provides on average 36 two-dimensional measurement points for charged particle tracks with $|\eta| < 2.5$ and $p_T > 0.5$ GeV.

4.4.2 The Calorimeters

The measured quantities in the detector are energies deposited inside calorimeter cells. The measured energies are used during the reconstruction step to calculate total energy and particle identification variables: once a particle enters the calorimeter, it produces a hadronic and/or electromagnetic shower that leads to energy depositions in several calorimeter cells (each shower will always follow an individual history). Since the energies of particles produced in proton-proton collisions at the LHC come in wide range it is necessary to construct calorimeters in a way that even the most energetic particles could be fully stopped.

The calorimeters could be classified in two groups: the electromagnetic calorimeters and the hadronic calorimeters.

- The Electromagnetic Calorimeter

  The electromagnetic (EM) calorimeter is a lead liquid-argon (LAr) detector and lead absorber plates over its full coverage. The electromagnetic LAr sampling calorimeter covers the range $|\eta| < 3.2$ and it has a great performance in terms of energy and position resolution.

FIGURE 4.5: ATLAS Calorimeters. From [12].

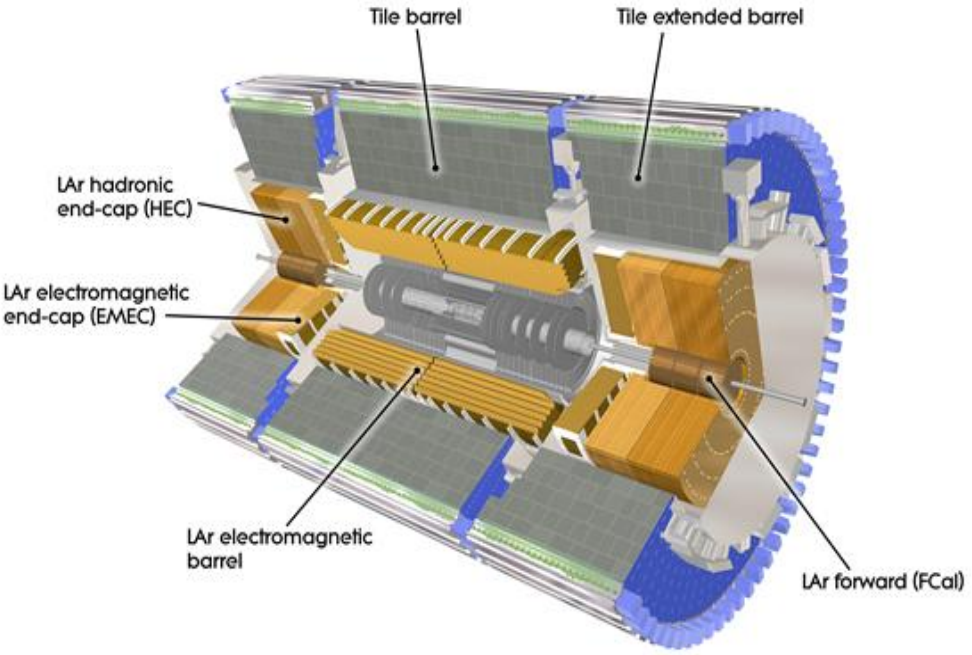

The EM calorimeter surrounds the inner detector, and it has been designed to identify and measure the energy of electrons and photons. The EM calorimeter is divided into a barrel part ($|\eta| < 1.475$) and two end-caps ($1.375 < |\eta| < 3.2$). It has an accordion geometry, which provides a complete ϕ symmetry without azimuthal cracks.

In the region closest to the inner detector, its granularity is especially fine, making possible to distinguish between partially overlapping showers.

- The Hadronic Calorimeter

  The hadronic calorimeter consists of three parts: the Tile Calorimeter (Tile-Cal), the liquid-argon Hadronic End-cap Calorimeter (HEC) and the liquid-argon Forward Calorimeter (FCal). One of its main parameters is its thickness, which should provide a good containment for hadronic showers and reduce punch-through into the muon system to a minimum.

  The Tile-Cal is a large hadronic sampling calorimeter which consists of a cylindrical structure with an inner radius of 2280 mm and an outer radius of 4230 mm. It covers the central range $|\eta| < 1.7$. It is placed directly outside the EM calorimeter where the level of radiation is relatively low.

  The HEC extends to $|\eta| < 3.2$, and the range $3.1 < |\eta| < 4.9$ is covered by the FCal. Both, the HEC and the FCAL, are integrated in the same cryostat.

4.4.3 The Muon System

Surrounding the calorimeter system, it is the muon spectrometer; and it is the largest tracking system at ATLAS with a radius of 4.25 m around the calorimeters, out to full radius of 11 m. The main goal is to detect muons exiting the calorimeters and to measure their momenta. It is based on the magnetic deflection of muon tracks in the large superconducting air-core toroid magnets, instrumented with separate trigger and high-precision tracking chambers.

The trigger system covers the pseudorapidity range $|\eta| \leq 2.4$.

FIGURE 4.6: Muon System. From [12].

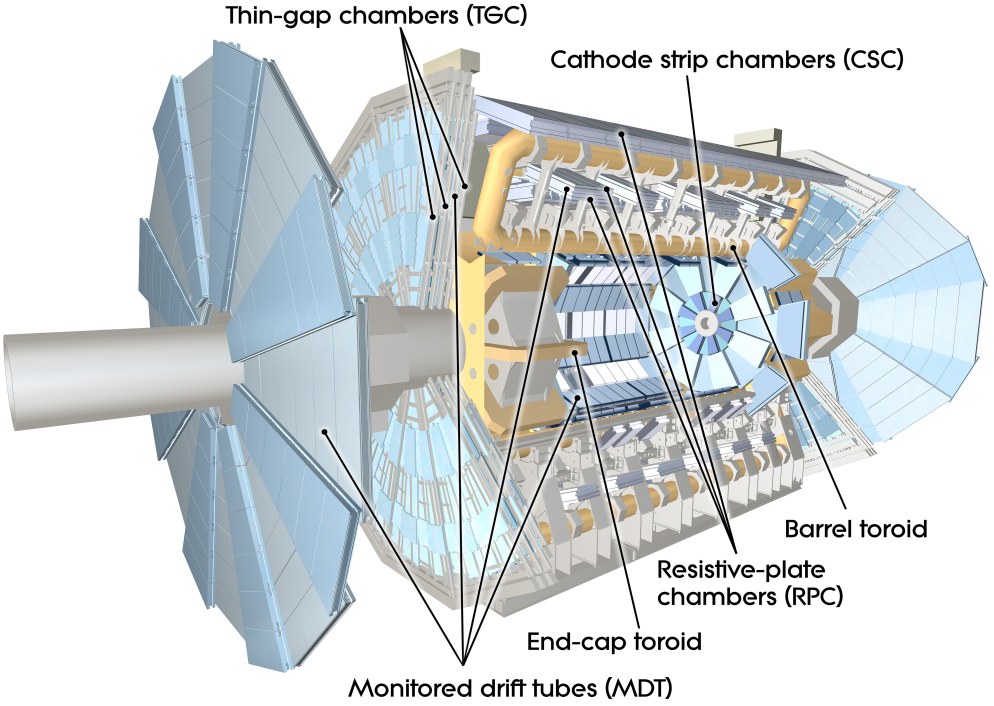

4.4.4 Magnet System

It provides the optimal conditions for particle identification and momentum measurement for each detector system separately. Consists in system of four independent magnet system called *Central Solenoid*, and three separate *Toroid* systems.

- Central Solenoid

  The central ATLAS solenoid consists of a flat superconducting cable located in the centre of an aluminium stabiliser with rectangular cross-section. This solenoid shares the cryostat with the LAr calorimeter.

It is situated around the inner detector and it is designed to provide a magnetic field of 2T in the inner tracker. This strength was chosen to maintain good tracking for the particles tracking, without them curling up before reaching the inner detector.

- Toroid Magnet

  This ATLAS magnet system consists of eight barrel coils housed in separate cryostat and two End-Cap cryostat housing eight coils each. The barrel part is installed outside the hadronic tile calorimeter, and the end-cap parts installed outside the liquid argon hadronic calorimeter. They are designed to produce and average toroidal magnetic field between 0.5T and 1 T.

4.4.5 Triggers and data-acquisition system

The ATLAS trigger and data-acquisition (DAQ) system is based on three levels of online event selection [21]. Each trigger level refines the decisions made at the previous level, and if it is necessary applies additional selection criteria.

Level-1 (LVL1) selects the bunch crossings which might contain interesting events. This trigger is based on a fast identification and processing essentially geographical coordinates in η and ϕ, called *Regions-of-Interest* (RoI's). The decision of whether or not to accept an event at LVL1 is made by a Central Trigger Processor (CTP). The CTP bases its decision on all the available information within the RoI's which is matched to a set of trigger menus which can be programmed with up to 256 distinct items.

After LVL1 a high level trigger (HLT), level-2 and event filter, take as starting point the RoI's provided by the LVL1 trigger. Then HLT uses the RoI's and the full detector information to provide a trigger decision in a series of steps. Every step must refine the information from the previous step by acquiring additional data from increasingly more detectors. Then, dedicated algorithms request detector data from within the RoI and attempt to identify features like tracks or calorimeter cluster. For all interesting signatures a second algorithm determines if the identified feature meets a criterion necessary to continue. The final stage in this level is carried by an event filter, which reduces the event rate and uses offline analysis procedures on fully-built events to further select events down to a rate which can be recorded for subsequent offline analysis.

Finally, the data acquisition system handles the distribution of data between the different levels of the trigger system and ultimately the mass storage for the events that passed the full trigger selection.

Chapter 5

ATLAS Simulation: ATLFast-II

5.1 Simulating Detectors

Particle physics uses simulations as a tool to understand the data obtained in a real detector produced by different physical phenomena. Under this consideration, a realistic description of the detector is needed, just as an accurate description of the elementary physics processes as well as the interactions of the particles with a detailed model of the detection apparatus. The Monte Carlo (MC) simulations provides an invaluable tool for comparisons between the expected results and the observed; even in absence of the real data measured by the detector, the MC simulation provides a way to design new physics analyses and quantify expected detector performance.

Furthermore, these analyses require a large number of MC simulated events for the estimation of systematic effects with increasing precision, the modelling of background processes and the sought signs of new physics with tiny cross sections.

In general, the MC production is usually a very Central Processor Unit (CPU) intensive task, and the simulation processes include:

- Event generation, which produces complete events starting from a collision (e.g. proton-proton, proton-nucleus) and it is achieved by general purpose generators;
- Physics and detector response, hits collection, digitisation of physics quantities and production of final output.

The simulation of particle interactions with the detector material, and the determination of the detector response, is a very time-consuming task and it spends a large fraction of the computing time, basically because it is simulated in the most accurate way possible.

Therefore, the simulations request a large amount of time to be completed, and this is not always feasible; consequently, it has been pursued faster and precise simulation strategies.

5.2 The ATLAS Detector Simulation

5.2.1 ATLAS Offline Software

The ATLAS software has two main components: the ATLAS online software, which is a software to configure, control and monitor the ATLAS Trigger and Data Acquisition System (Trigger-DAQ project); and the ATLAS offline software, which has as goals to process the events delivered by the Trigger-DAQ system, to deliver the processed results to physicists within the ATLAS Collaboration and to provide tools for them to analyse the processed information and obtain physics results.

The ATLAS offline software has simulations as a primary data processing activity; together with event generation, digitisation, detector reconstruction, physics analysis and so on.

ATLAS adopted an object-oriented development methodology, based primarily on `C++` programming language, and a component-based model by which applications are developed from collections of plug-compatible components based on a variety of configuration files. This is supported by a common framework (explained below), and it results in a great flexibility in meeting the basic processing needs of the experiment.

Due to the complexity and scale of ATLAS experiment, the software must be highly modular and robust, but particularly it must be flexible enough to meet the need throughout the detector lifetime: to adjust to the changes in the physics goals and detector hardware. To simulate a very complex detector such as ATLAS, the software has to take into account as large number of physics processes as possible, and covering from physics processes with energies around 10 eV (e.g. ionisation potential in the active gas of various detectors [22]) to process with high energies in the order of TeV (according with the requirements set for the ATLAS detector, Chapter 4.3) .

ATLAS Software Framework

The simulation of the detector is integrated into the ATLAS software framework: Athena.

Athena is a control framework; that means, it is a skeleton of an application into which developers plug in their code, and as it is component-based it has allowed flexibility in

providing common functionality and communication between different components. But, Athena is an implementation of an architecture called Gaudi: instead of developing an entirely new physics data processing infrastructure for particle physics, ATLAS adopted a project originally developed by the LHCb experiment: the Gaudi Framework, and it includes classes particularly designed for high-energy physics software. However, while the Gaudi project is a kernel of software common to both experiments, Athena has more ATLAS-specific enhancements.

Athena includes software for event simulation, event trigger, event reconstruction and physics analysis tools. But in order to control Athena, python[1] scripts[2] are used to set the algorithms configuration at run-time, as well as the properties established for each script.

The ATLAS software is organised into hierarchical structure of projects and packages. Each package has a label that distinguishes different versions, a tag number; and each project has a release number to identify it.

5.2.2 ATLAS Simulation Data Flow

The production of Monte Carlo (MC) events follows a chain of processing stages, which can be seen in the following simulation data flow, Figure 5.1.

FIGURE 5.1: ATLAS Simulation data flow.

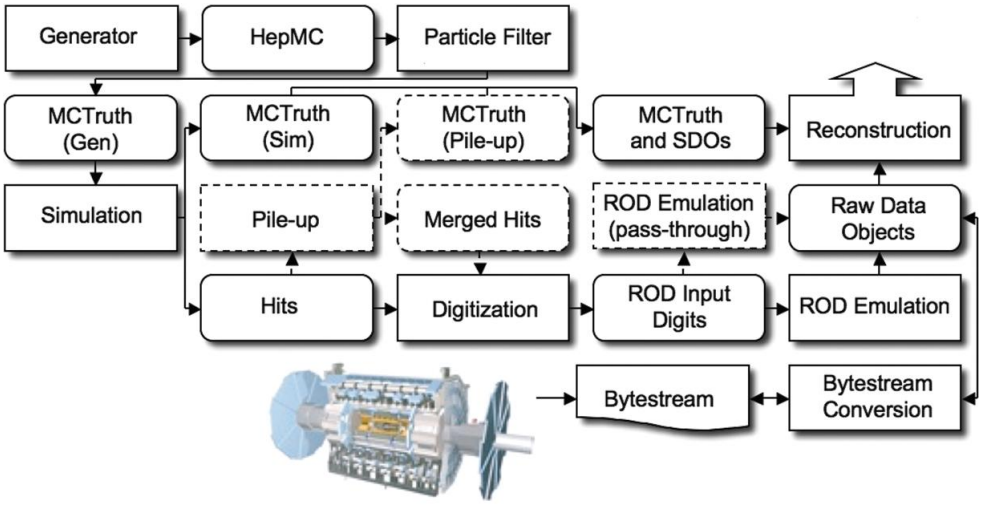

First, a generator produces events in a standard format, called HepMC[3]. These events could be filtered, and only those with a certain property would be kept (e.g. leptonic

[1]Python is an interpreted, object-oriented programming language; and it is used inside ATLAS as a scripting language.

[2]aka Job Options.

[3]HepMC is an Object Oriented event record written in C++ for High Energy Physics Monte Carlo event generators.

decay). The generator is responsible for any prompt decays, and because it only considers immediate decays there is no need to consider the detector geometry during the generation step[4]. In this step the run number for the simulated data set and event number for each event are established.

The generated events follow to a simulation step, where a record of all particles produced by the generator is retained in the simulation output file. A particle filter could be here applied, to select only certain particles to process in the simulation; and each particle is propagated through the full ATLAS detector by Geant4 simulation (5.2.2), or through the fast simulation of the detector (5.2.2). Then the energies deposited in the detector are recorded as "hits", containing the total energy deposition, position, and time. These hits are recorded in the simulation output file: the *hit file*.

The simulation is the slowest of all the steps, and can take several minutes per event with full Geant4 simulation of the detector. So, simulation jobs are divided into groups of 50 or fewer events in order to use resources and time more effectively.

In both prior steps, information called "truth" is recorded for each event. The truth information is a history of the interaction from the generator, including incoming and outgoing particles. In the event generation a record is kept for every particle, while in the simulation jobs truth track and decays for certain particles are stored.

The next step in the chain is the digitisation; it converts the hits produced by the simulation into "digits". A digit is a detector response, produced when the voltage, or current, on a particular readout channel rises above pre-configured threshold within a particular time window; the digits of each sub-detector are written out as Raw Data Objects (RDOs).

The final step is the reconstruction, where from the RDO files the particle parameters and information necessary for physics analysis are reached; the reconstruction applies for both, simulation and real data, but with the exception that truth information is only available in simulated data. The reconstruction also follows a chain of stages, as it is shown in Figure 5.3.

The first step in the reconstruction chain involves the reconstruction of the tracking and calorimetry detectors, allowing to identify photons, electrons, muons, tau-leptons, and to reconstruct jets, missing transverse momentum, primary vertex; where information from all sub-detectors are combined to reach an optimal reconstruction. The output is stored in an Event Summary Data file (ESD).

[4]This is valid except when the generator stores some "stable" particles expected to propagate through certain part of the detector, then it is necessary to control what particles are considered, and therefore the geometry.

FIGURE 5.2: The reconstruction of events chain of stages [23].

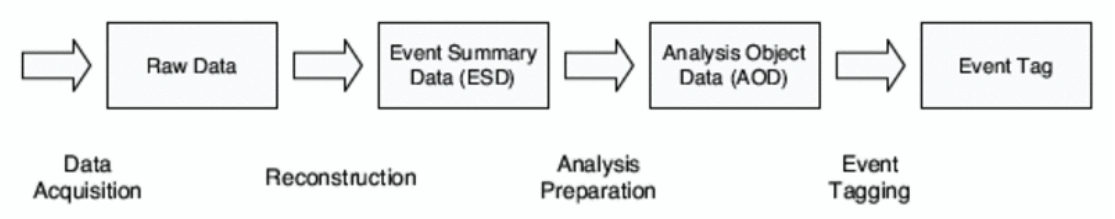

The next step is the Analyses preparation; and it includes the reconstruction of more complex objects (e.g. the b-tagged Jet); and it is basically a summary of the reconstructed events. The output is written on Analysis Object Data (AOD). An AOD is produced from the ESD, and it makes unnecessary to track back and process the raw data, because it contains enough information to do a physics analyses.

A n-tuple style representation of the event data for end-user analysis is used to defined a dataset with the AOD information. This n-tuple representation is called DPD, Derived Physics Data, and it is the final file before the physicist does the analysis of the data sample.

The Generators

The event generators are responsible for the modelling of the complex physics processes that lead to the production of hundreds of particles per event at LHC energies, from the physics of hard process to hadronization and decays [23]. They are used to set the detector requirements, to formulate analysis strategies, or to illustrate uncertainties in the physics modelling.

The list of supported generators includes Herwig, Pythia, Isajet, Hijing, CompHep, and many others; but it is of relevance for the current study the JIMMY generator, as it will be shown in Chapter 6.

JIMMY generator is a library of routines which is linked with the Herwig Monte Carlo event generator [24]. Herwig, meanwhile, is a Monte Carlo package for simulating hadron emission reactions with interfering gluons [25], which allow to plug the JIMMY package designed for multiple interactions and to generate multiple parton scattering events in hadron-hadron, photon-photon or photon-hadron events.

The GEANT4 Toolkit

The Geant4 simulation (G4) toolkit [26] has provided a set of software components, where all aspects of the simulation process have been included: the geometry of the system, the materials involved, the fundamental particles of interest, the generation

of primary particles of each event, the tracking of particles through the detector, the physics processes involved in the different particle interactions, the response of the detector components, the generation of event data, the storage of events and tracks, the visualisation of the detector and the particles trajectories, and the simulation data at different levels for subsequent analyses.

All in all, the G4 toolkit allows to create a geometrical model with a large number of components of different shapes and materials, and to define the elements that record information (*hits*) needed to simulate detector responses (*digitisation*); furthermore it also provides a set of physics processes to model the behaviour of particles.

The different aspects include in the toolkit are: the geometry of the system, the materials involved, the fundamental particles of interest, the generation of primary events, the tracking of particles through materials and electromagnetic fields, the physics processes governing particle interactions, the response of sensitive detector components, the generations of event data, the storage of events and tracks, the visualisation of the detector and particle trajectories and the capture and analysis of simulation data, as it is indicated in [26].

From the above list it is important to highlight one aspect, the physics processes. Geant4 toolkit offers different physics processes with different details of physics modelling depending on the needs of the user. These physics processes available are called *the physics lists* [27].

There are four families of lists: the LHEP list or parametrised modelling of hadronic interactions; the QGS or list based on a modelling using Quark Gluon String model for high energy hadronic interactions of protons, neutrons, pions and kaons; the FTF or list based on a modelling using the FRITIOF model for high energy hadronic interactions; and more specialised lists (which could be created or modified by the user).

The physics list used for the simulation of the data sets used for the analysis in Chapter 6 was the *QGSP_BERT* list, which uses Bertini cascade[5] for primary protons, neutrons, pions and kaons below ∼10 GeV, and produces more secondary neutrons and protons simulating a better agreement to experimental data [27].

The ATLAS detector geometry description

The geometrical description of the ATLAS detector depends on two databases: one of them stores basic constants, the ATLAS Geometry database, and the other one stores various conditions data for a specific run chosen, ATLAS Condition database.

[5]The Bertini cascade model generates the final state for hadron inelastic scattering by simulating the intra-nuclear cascade [28].

However, to describe the detector it is used a label (a version tag) to indicate into the databases certain configurations of the geometry and some other properties related to the detector. The version tag is specified at simulation time (or when the real data is recorded) and it remains along with the event data.

Simulation Strategies

FIGURE 5.3: The different ATLAS simulation strategies [23].

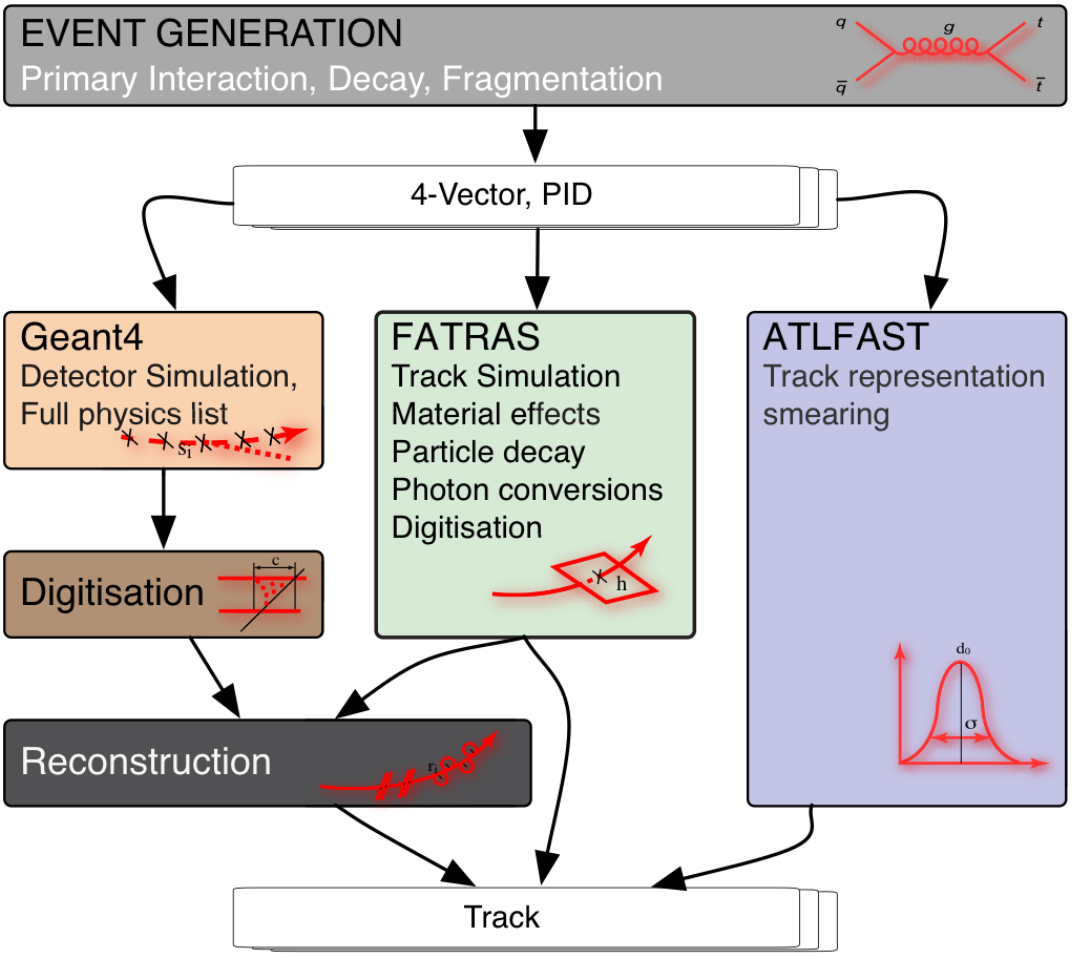

- ATLAS Full Simulation of detectors

  The most detailed description of the detector consists to simulate the propagation and interaction of all particles through a detailed computer model of the detector, and it includes simulation of the energy measurement process and the electronics used. The standard, and most realistic, simulation of the ATLAS detector is based on the Geant4 particle simulation toolkit.

  Geant4 simulation provides a detailed description of the physics processes and the particle transportation through a defined geometry, and its implementation gives

very good results; but it is CPU-time consuming and for many studies the required simulated statistics are hard to be achieved. Hence, extra techniques have been developed to complement and to improve the full Geant4 simulation (fullSim).

- ATLAS Fast Simulation of detectors

  As it was said before, to achieve the required simulated statistics using fullSim it is not viable many times, therefore a faster way to obtain an accurate simulation of the detector is needed. To complement the fullSim and to meet the need for faster simulations, a group of packages that increase the speed of the detector simulation (compared with fullSim) was created: ATLAS Fast Simulation (ATLFast).

  The major part of the CPU-time consumption of fullSim (nearly 80% of the full time [22]) is spent simulating particles when traversing the calorimeters whilst about 75% of the fullSim CPU-time consumption is spent simulating electromagnetic particles. The fast simulation intends to speed up the slowest parts of the fullSim, by removing electromagnetic particles from the calorimeters and replacing them with pre-simulated showers stored in a library.

  That is, if a particle is in the adequate energy range ($> 10\ GeV$) [22] is replaced by a shower rotated and scaled to match the primary particle. But, this has as a disadvantage that the possibilities are limited to the shower shapes stored.

  The fast simulation could be done by ATLFAST-I (AtlFast1) or ATLFAST-II (AtlFast2 or AF-II) package.

  ATLFAST-I

  It has been developed for physics studies that require very large statistics but do not require a high level of details, compared with fullSim. AtlFast-I executes a fast simulation by replacing detailed detector simulation with parametrisation of the desired detector and reconstruction effects, and smearing truth objects to provide physics objects similar to those of the reconstruction; but it is not a realistic detector description, and it is not possible to study detector-based quantities (e.g. track hit positions). This makes AtlFast-I the least detailed simulation method with lower accuracy.

  In spite of that behaviour, AtlFast-I provides an useful method of making quick estimates of systematic uncertainties in early data analyses due to the simple process of re-parametrise the detector; furthermore, without those large statistics it would not be possible to study the physics process of some signatures which requires large amount of events.

ATLFAST-II

ATLFast-II (AF-II) is a fast simulation package meant to provide large statistics and it was thought to complement (and to improve) studies done with full Geant4 Sim and AtlFast-I. It was intended to simulate events as fast as possible but being able to run the standard ATLAS reconstruction, and even more to be able to do analyses for ATLFast-II and full Geant4 simulation without modifying any code.

The advantage over AtlFast-I relies on the ability to combine fast simulation with full simulation of the sub-detectors (detailed explanation 5.3), allowing to simulate with G4 to provide higher level of accuracy in specific objects reconstruction but in a shorter CPU time consumption than the fullSim time. And, unlike AtlFast-I, reconstructed ATLFast-II output includes all the properties associated with a reconstructed object.

Digitisation and Reconstruction

The physical information in the hits produced during the simulation step need to be re-processed in order to simulate the detector output, and written out to be then used by the reconstruction programs. The digitisation operates locally at each sub-detector, and the output obtained is similar to that which might be expected from the readout electronics in the experiment.

The output of the digitisation are called RDO (previously explained), and they are going to be used by the reconstruction programs. The reconstruction proceeds in two stages: first, the data from the detector is reconstructed in a stand-alone mode; and then, the information from all the detectors is combined so that the reconstruction is optimal for the full momentum range, full rapidity range and any luminosity to get the most accurate measurement and identification of the final physics objects with the least background.

5.3 ATLFast-II Simulation

According to the prior description of ATLFast-II package (AF-II), AF-II simulation is closer to fullSim than AtlFast-I and it was designed to improve the fast simulation of the detector, but with the output containers having the same names and contents as in fullSim (standard ATLAS reconstruction can be run and same AOD information as for fullSim events). AF-II has arisen as the solution to the CPU-time consumed by G4 to make a detailed description of the detector and the particle interactions, and it has been validated since 2011 for large-scale MC production together with fullSim [22]. But, it is

still being verified as to accuracy (according with the needs to meet for different areas of research) and to identify possible weaknesses in the physics objects description of AF-II.

The primary benefit of AF-II, it is the possibility of simulated each sub-detector of ATLAS in both ways: fast simulated and/or full simulated. However, the possible combinations of fullSim and fast simulation for AF-II are:

- a full simulation of the Inner Detector, but with the opportunity to change to a fast simulation (Fatras);
- a fast simulation of the Calorimeters (FastCaloSim);
- a full simulation for the Muon system, but with the chance to use also a fast tracking simulation (same as Inner Detector, Fatras);
- a normal trigger simulation for the Trigger system, if the Fatras simulations were not used before.

The current combination of AF-II simulations[6], called **ATLFast2-D**, has a G4 simulation for the inner detector; it has a calorimeter simulation done by FastCaloSim, with the output of this simulation converted into a G4 hits and then processed by the G4 calorimeter digitisation; it has a G4 simulation (together with the inner detector) of the muon system, which means that muons are fully simulated and reconstructed; and a normal trigger simulation.

The other possible combination, called **ATLFast2-F**, was thought as pure fast simulation and therefore no trigger information is managed: the inner detector and the muon system are simulated with the fast track simulation package, Fatras; and the calorimeters are still simulated by FastCaloSim. This combination is intended to show a high level of agreement with fullSim and to significantly reduce the average amount of CPU-time spent.

5.3.1 FastCaloSim

Earlier it was explained that most of the CPU-time consumed by the ATLAS detector G4 simulation is spent in the calorimeter section. For this reason, the aim of ATLFast-II was to make a simulation as fast as possible in that section, to decrease the large amount of time used by full Geant4 Simulation, but doing a realistic description of the detector.

[6] And the combination used to develop this study.

FastCaloSim (simulation of Calorimeter for AF-II) provides a parametrised simulation of the particle energy response and energy distribution in the calorimeter; but this simulation should work with the ATLAS reconstruction and identification code used on full Geant4 Simulation, and that will be used for real data.

The simplifications used for FastCaloSim are [29]:

1. In the calorimeter, the measured quantities in the detector are energies deposited inside the calorimeter cells. These measured energies are used during the reconstruction step to calculate the total energy and particle identification variables from the relative distribution of energies in the cells. Once a particle enters the calorimeter, it produces a hadronic and/or electromagnetic shower that leads to energy depositions in several calorimeter cells; even for identical particles these showers will always follow an individual history, then two showers are not identical, they have fluctuations that make them different.

   The simulation method in FastCaloSim is to try to simulate only the average shower properties and uncorrelated fluctuations, but to ignore fluctuations from the individual shower development. Then, a particle is deposited into the calorimeter without tracking the particle propagation, interaction and shower development as in the full Geant4 simulation.

2. Full Geant4 simulation uses the reconstruction geometry of the calorimeter that describes calorimeter cells as cuboids in the r/z, η, ϕ space. For the purpose of the fast simulation a simplified geometry is absolutely sufficient, although some particle shape distortions due to the simplified geometry close to the calorimeter cracks can be expected. The parametrisation is done within the continuous calorimeter regions away from the calorimeter boundaries, then close to the boundaries differences from the full Geant4 simulation could be expected.

3. Only three types of particles are used in order to parametrise the simulation: photons, electrons and charged pions. The charged pion parametrisation is used for all hadrons (neutral and charged), due to most of the hadronic activity in QCD events are dominated by charged pions. Muons are currently ignored by FastCaloSim and no energy deposition for muons in the calorimeter is simulated, then no simulation of the muon energy loss in the calorimeter or the punch-through is applied.

5.3.2 Muons Performance in AF-IID

Muons in AF-II [7] are fully simulated by G4 simulation. They are tracked through the calorimeter system, and it is taken into the simulation the energy loss due to ionisation and bremsstrahlung; therefore, despite muon being ignored by FastCaloSim and no energy deposition because of them is simulated in the calorimeters, it is expected a good agreement.

That means secondary muons produced in the development of hadronic showers in the calorimeter region are not included in AF-II, having as a consequence no punch-through particles included in the simulation; and therefore it is understandable an underestimation of the occupancy in the muon chambers and of the rate of reconstructed true and fake muons.

[7] Hereafter, to simplify the terminology used, AF-II will refer to AtlFast2-D since it was the combination used to simulate the samples studied for this analysis.

Chapter 6

Electron-Muon Resonance Analysis

6.1 Setup of the Study

As it was said in Chapter 3, it is of interest to investigate the performance of ATLFast-II in a particular RPV SUSY model predicting the existence of a heavy neutral short-lived resonance (the tau sneutrino) that decays to an electron-muon pair with opposite charges.

The current study used three mass points: a high sneutrino mass point, 2000 GeV; a low sneutrino mass point, 100 GeV, and a sneutrino mass point of 650 GeV used in previous studies [5]. Data used in this analysis are proton-proton collision Monte Carlo simulated data at center-of-mass energy $\sqrt{s} = 7$ TeV normalised to an integrated luminosity of 4,7 fb^{-1}. The data sets used are listed in the Appendix A.

Initially all the samples (A) were made from the same JIMMY/HERWIG Monte Carlo event generator[1] (tag *e1170*). Thereafter, they had different detector simulation (full simulation, tag *s1372*, vs fast simulation, tag *a131*), in which either full Geant4 simulation or ATLFast-II simulation were used in order to produce HITS files. Then, the HITS files were digitised, reconstructed and "ntuple-ized" identically in both cases. Each of the samples simulated with full Geant4 simulation (each one with 99899 events) were normalised such that the number of events was the same as in the corresponding sample simulated with ATLFast-II (100000 events). Originally, the number of events requested for each sample was 100000 events; however, full Geant4 simulation failed 1 out of 1000

[1] JIMMY is a plug-in for HERWIG (see Chapter 5) generators which allows to generate a realistic underlying event: multiple parton scattering events in hadron-hadron, photon-photon or photon-hadron events.

Production Tag	AF-II/fullSim	Production Step	Comment
e1170	AF-II/fullSim	evgen	JIMMY/HERWIG Generator
a131	AFII	simul	HITS simulation (EVNT→HITS)
s1372	fullSim	simul	HITS simulation (EVNT→HITS)
s1353	AFII	merge	Merging of HITS files
s1370	fullSim	merge	Merging of HITS files
a145	AFII	recon	AOD Reconstruction Digitisation + Reconstruction (HITS→RDO→ESD→AOD)
r3043	fullSim	recon	AOD Reconstruction Digitisation + Reconstruction (HITS→RDO→ESD→AOD)
r2993	AF-II/fullSim	merge	Merging of AOD files
p832	AF-II/fullSim	merge	SUSYD3PD (AOD→NTUP_SUSY)

TABLE 6.1: Production tag comparison per event.

event simulation, due to segmentation faulting over and over. As the lost was only 0.1% of the statistics, no measures are taken by the production team in such case. In general, only if the loss is 5% or more there will be a debugging and re-submission effort.

Table 6.1 shows the samples production steps, and their respective production tag, for full Geant4 simulation and ATLFast-II simulation. The following example will illustrate the content of Table 6.1:

Consider one of the samples for each detector simulation (A), that is:

ATLFast-II Sample:
mc11_7TeV.106486.RPV_emu100_jimmy_susy.merge.NTUP_SUSY.e1170_a131_s1353_a145_r2993_p832

full Geant4 Simulated Sample:
mc11_7TeV.106486.RPV_emu100_jimmy_susy.merge.NTUP_SUSY.e1170_s1372_s1370_r3043_r2993_p832

The TAG split means:

e1170: full Geant4 and ATLFast-II Event Generation: the events were generated from JIMMY/HERWIG Monte Carlo event generator with Athena release 16.6.9.5.

a131/s1372: ATLFast-II Simulation tag / full Geant4 simulation tag. Both simulations were made with G4 toolkit and the physics list QGSP_BERT (Chapter 5), though the description is pretty specific for each one (e.g. fast simulation ATLFast-II has FastID-Killer, which modifies full simulation to kill all particles except muons at the exit of the ID).

s1353 / **s1370**: HITS Merging tags. Both are hits merging tags, though the difference is not based on fast simulation or full simulation of the detector, but in different Athena and database (DB) release numbers; beyond that they have the same tag definition.

a145 / **r3043**: ATLFast-II digitisation+reconstruction tag / Digitisation and reconstruction tag. Tag definition shows differences between the digitisation+reconstruction tag related to ATLFast-II and the tag linked to full Geant4 simulation; e.g., the a145 definition specifies ATLFast-IID (Chapter 5) configuration for digitisation and reconstruction of the events.

r2993: AOD Merging tag. The reconstruction configuration is the same for both simulations.

p832: Performance DPD tag, generates SUSYD3PDs for both simulations.

As described above, the relevant tags are **a131**/**s1372** and **a145**/**r3043**; which confirms that differences are only in the detector simulation and reconstruction steps.

6.2 Time Performance

The greatest advantage of using ATLFast-II instead of full Geant4 simulation to simulate the detector behaviour and to generate the MC signal samples, it is the least amount of time used by ATLFast-II throughout the production steps until the generation of the Ntuple files (Chapter 5). This is a key aspect for SUSY analysis where a high demand for a large number of GRID resource consuming samples is usual. Therefore, it is desirable to know how much time ATLFast-II spends and to compare it with the full Geant4 simulation time.

In order to know this difference, one must take into consideration two different time analysis: the CPU-time consumption and the end-user waiting time. What distinguishes one from another is the process where the time is being measured; the CPU-time consumption only measures how long it takes to each script (each production step here), as it is shown in table 6.2, while the end-user waiting time is related to the time elapsed since the request of the analysis until the samples are available to the user. The end-user waiting time includes the waiting time for each job to be done (which is directly related with the priority given to the production on the GRID), this idea is shown in table 6.4.

To observe the gain in terms of CPU time and end-user waiting time, the samples used were sneutrino 100 GeV sample (emu100) and sneutrino 2000 GeV (emu2000) sample, both generated by ATLFast-II and full Geant4 simulation. The analysis was made for each production step.

6.2.1 CPU-Time Consumption

Each production step has certain number of jobs done to generate the total number of events; these number of jobs and events per job are the same for each full Geant4 simulated file and ATLFast-II file.

To calculate the time spent for every event simulated, it was done an average for each job completed by the scripts. Those times and the number of jobs (and events) were founded on PanDA[2].

Table 6.2 shows how much time (in minutes) was spent per event. It is interesting to notice here that the major difference between all the production steps falls over, as expected, the detector simulation; where the time difference per event generated by full Geant4 simulation of the detector is around 10 (emu100) to 25 (emu2000) times larger than the ATLFast-II simulation time.

Production Step	**emu100**		**emu2000**	
	fullSim (min/event)	AF-II (min/event)	fullSim (min/event)	AF-II (min/event)
evgen	0.0021	0.0021	0.0027	0.0027
Detector simulation (HITS)	3.8822	0.3840	8.9280	0.3475
HITS merging	0.0288	0.0107	0.0342	0.0120
AOD reconstruction	0.5442	0.6132	0.5728	0.5532
AOD merging	0.0051	0.0043	0.0100	0.0046
NTUP_SUSY	0.0226	0.0247	0.0233	0.2788
Total time	4.4850	1.0390	9.5709	1.1989
fullSim/AF-II Simulation Ratio	10.1099		25.6921	
fullSim/AF-II Digitisation Ratio	0.8875		1.0354	
fullSim/AF-II Total Ratio	4.3166		7.9831	

TABLE 6.2: CPU time consumption for each production step.

The ratio between fullSim and AF-II per production step and the total ratio time[3] should be approximately the same for all samples used here. Nevertheless, differences between the sneutrino 100 GeV mass point full simulation time and the sneutrino 2000 GeV mass point full simulation are observed, which has as a consequence different simulation ratio and total ratio between both data samples. Various hypotheses explaining the differences are handled; first, broadly the number of attempts to finish a job was larger

[2]PanDA is the Production ANd Distributed Analysis system which has been developed by ATLAS since 2005 to meet ATLAS requirements for a data-driven workload management system for production and distributed analysis processing capable of operating at LHC data processing scale. PanDA has processed more than 25 million jobs as of January 2009, at a typical rate of about 50k jobs/day and 14k CPU wall-time hours/day for production at 100 sites around the world, and 3-5k jobs/day for analysis. More information about it could be found in [30].

[3]The ratio between fullSim and AF-II time, and not the time per step.

for the electron-muon 2000 GeV full simulated data sample than for the electron-muon 100 GeV full simulated data sample. While the last one had all the jobs finished in the first attempt, the electron-muon 2000 full simulated data sample expended between one to three of five attempts to manage to finish correctly each job. Second, the differences also could be justified by assuming they were subject to different machines, for instance while for the electron-muon 100 GeV data samples some of the CPU models were Intel(R) Xeon(R) CPU X5650 at 2.67GHz with cache size[4] of 12288 KB, for the electron-muon 2000 GeV data samples some of the CPU models were Intel(R) Xeon(R) CPU E5430 at 2.66GHz with cache size of 6144 KB; then differences between a simple detail as cache size were twice the size for 100 GeV fast simulated sample, which implied different CPU performance. The electron-muon 100 GeV and the electron-muon 2000 GeV fast simulated data samples instead had CPU models were the CPU differences were not so large (e.g. while electron-muon 100 GeV fast simulated had a cache size around 6000 KB, electron-muon 2000 GeV fast simulated had a cache size around 8000 KB).

6.2.2 End-User Waiting Time

As previously mentioned, end-user waiting time refers to the total running time (or total wall-clock time), and it is calculated since the sample was requested until it is available as a Ntuple.

Table 6.4 shows the requested time for the samples which are being compared (and it is the same for each of them), and it also shows the total wall-clock time for emu100 and emu2000 samples generated by ATLFast-II and full Geant4 simulation. Accordingly, the end-user waiting time for ATLFast-II is shorter than the end-user waiting time for full Geant4 simulation. This result was expected in accordance with the CPU-Time consumption results showed before (Table 6.2), however in previous studies about the end-user waiting time performance [4] the priority given to the ATLFast-II samples was an influential factor on the time performance and ATLFast-II had been giving lower priorities in the past, as a result the gain in the end-user time was completely negligible. But, these current results are showing that (almost) the same priority was given for both detector simulations and then the differences about the time performance and the gain in end-user waiting time are significant: for the electron-muon 100 GeV data sample ATLFast-II simulation is around 1.4 times faster than full Geant4 simulation, and for the electron-muon 2000 GeV data sample ATLFast-II is around 2.3 times faster than full simulation (e.g. the electron-muon 2000 GeV data sample spent more than 24 days to be available for the user, the one generated by ATLFast-II spent roughly 10 days).

[4]The cache size is related with a better performance and consumption of the CPU.

emu100				
AF-II				
Requested Time Total wall-clock time	2012-04-04 21:20 From 2012-04-04 21:51 to 2012-04-13 22:23			
Step Production	Pending Time	Running Time (average)	Maximum Run. Time	Minimum Run. Time
HITS simul	till 88 hours	03:12:00 hours	4:57:44 hours	02:31:51 hours
HITS merge	till 14 hours	00:10:40 hours	0:29:46 hours	0:04:29 hours
AOD recon	till 22 hours	10:13:12 hours	22:11:32 hours	05:13:20 hours
AOD merge	till 2 hours	00:21:31 hours	00:23:42 hours	00:18:46 hours

fullSim				
Requested Time Total wall-clock time	2012-04-04 21:20 From 2012-04-04 21:51 to 2012-04-17 13:44			
Step Production	Pending Time	Running Time (average)	Maximum Run. Time	Minimum Run. Time
HITS simul	till 54 hours	06:28:13 hours	25:06:06 hours	04:21:52 hours
HITS merge	till 6 hours	00:28:50 hours	00:31:58 hours	00:10:16 hours
AOD recon	till 39 hours	09:14:02 hours	14:24:21 hours	04:48:46 hours
AOD merge	till 4 hours	00:25:16 hours	04:14:19 hours	00:08:49 hours

emu2000				
AF-II				
Requested Time Total wall-clock time	2012-04-04 21:20 From 2012-04-06 11:25 to 2012-04-16 22:53			
Step Production	Pending Time	Running Time (average)	Maximum Run. Time	Minimum Run. Time
HITS simul	till 107 hours (4 days) (average between 6-22 hours)	02:53:46 hours	04:18:36 hours	02:30:22 hours
HITS merge	till 26 hours	00:11:58 hours	00:32:06 hours	00:05:31 hours
AOD recon	till 29 hours	09:13:12 hours	17:00:58 hours	05:06:19 hours
AOD merge	till 11 hours	00:23:14 hours	00:30:00 hours	00:16:43 hours

fullSim				
Requested Time Total wall-clock time	2012-04-04 21:20 From 2012-04-06 11:25 to 2012-04-30 19:18			
Step Production	Pending Time	Running Time (average)	Maximum Run. Time	Minimum Run. Time
HITS simul	till 23 hours	14:52:48 hours	31:21:34 hours	12:03:38 hours
HITS merge	till 2 hours	00:34:09 hours	01:07:32 hours	00:31:10 hours
AOD recon	till 51 hours (average 2 hours)	09:32:46 hours	17:46:19 hours	04:52:52 hours
AOD merge	till 2 hours	00:49:47 hours (*)	02:15:46 hours	00:16:43 hours

TABLE 6.3: End-user waiting time for ATLFast-II and full Geant4 simulation of an sneutrino with 100 GeV mass point and a sneutrino with 2000 GeV mass point. It also shows the average performance time during each production step for each sample and simulation with the maximum waiting time before it started, and the maximum and minimum time observed in the jobs.

Table 6.4 also shows a comparison between the maximum pending time[5]: the waiting time for each sample before the production steps started; and it is possible to observe that the pending time for ATLFast-II was larger than for full Geant4 simulation in general terms. Though, the total end-user waiting time referred to the production of the samples spent less time for ATLFast-II as it was stated before.

[5]Please note that it refers to a maximum value and not an implicit average value.

6.3 Physics Objects Analyses

Chapter 5 explained ATLFast-II as a tool which provides a reasonably realistic but fast simulation of the detection and reconstruction of particles in the ATLAS detector.

In fact, it was demonstrated in Section 6.2 that ATLFast-II simulation indeed guarantees a faster production of samples, but its use is only justifiable if no accuracy in the physics description is lost.

ATLFast-II simulation requires that all the particles are tracked through the inner detector using the full Geant4 simulation, but at the end of the ID volume all the particles, except for muons, are killed; then the energy depositions in the calorimeter are simulated using parametrised shower models for all the particles but muons, which are simulated through the detector with full Geant4 simulation.

This section is intended to test if ATLFast-II could describe kinematic objects without losing precision, and generating physics objects distributions similar to those produced by a full Geant4 simulation of the detector. This section includes: first, the definition of the physics objects used in the analysis, according with the definition given by the prior study searching a heavy neutral particle decaying into an electron-muon pair: these object definitions follow mostly the E-Mu Analysis Team[6] and the SUSY Working Group[7] recommendations, used by SUSY analyses. Second, the comparison between the kinematic objects for each sneutrino mass point for both detector simulations.

The physics objects to be presented below were obtained after applying the same cut-flow for each sneutrino mass point: one electron and one muon, in accordance with the object definitions given, with opposite charge. The ratio showed in the distributions is the result of the division between the statistical population for certain full Geant4 simulation result and the statistical population for the same ATLFast-II result minus one [(fullSim / AF-II) - 1].

Some of the results were shown in two presentations for ATLAS groups (RPVLL SUSY Group[8] and ISF Developers[9] meetings). The main difference between those previous results and the ones showed here are a few changes in the object definitions.

[6] The E-Mu (Electron-Muon) Analysis Team is part of the Exotics Working Group at ATLAS Experiment, and it is responsible of the heavy neutral particle search.

[7] All the SUSY Object Definition recommendations are given for Athena release 17 (r17), which is the Athena release number used for the analysis.

[8] ATLAS R-Parity Violating and Long-Lived group.

[9] ATLAS Integrated Simulation Framework Developers.

6.3.1 Object Definitions

In order to identify physics processes, particles such as leptons, jets, and missing transverse momentum are dened starting from the reconstructed objects. This is a so-called object denition. This subsection gives an introduction to the identication of objects used in this thesis (Appendix C gives a summary).

Electron :

Electron tracks with transverse momentum $p_T > 0.5$ GeV and $|\eta| < 2.5$ are reconstructed and measured in the inner detector; values of $p_T > 25$ GeV and $|\eta| < 2.47$ are going to be considered. Then, the standard identification of electrons is based on cuts on the shower shapes and information from the reconstructed tracks. The first cuts on the shower shapes to be applied are the *loose cuts* for a simple electron identification, these cuts consists of simple shower-shape cuts, where a simple and excellent identification of electrons is provided based only on limited information from the calorimeters, but with low background rejection [31]; the electrons identified after these cuts are the baseline electrons. Another set of cuts is applied, the *medium cuts* and they add shower-shape cuts using important information contained in the first layer of the electromagnetic calorimeter, these cuts require reconstructed tracks to have at least seven precision hits in the pixel and SCT sub-detectors; these electrons will be the signal electrons of the analysis [32]. For the electron identification a standard cluster-based algorithm called *author* is used, and it is set to 1 or 3; when author is set to 1, the electron has been found only by the standard (cluster based) algorithm. While if the author is set to 3 the object has been found by the standard (cluster based) and the track-based algorithms[10] [33].

Many analyses in ATLAS are based on final states with isolated leptons, processes that have the advantage of a small background expectation but they also suffer from jet background processes: semi-leptonic heavy-quark decays mimic the isolated leptons signal [31]. Then, a likelihood estimator for the separation of isolated electrons from non-isolated electron background is described for the current study as the transverse energy deposited in the calorimeter within a cone of radius $\Delta R = \sqrt{\Delta\eta^2 + \Delta\phi^2} = 0.4$ around the electron cluster, excluding the electron E_T.

Muons :

[10] It is possible to set the author to 2, and it means that the object has been found by only the soft (track based) algorithm. But it is not of interest for this study.

The muon reconstruction strategy considered is the *muon staco combined*; the combined strategy is a combination of a muon-spectrometer track with an inner-detector track over the range $|\eta < 2.5$ produce by the staco algorithm. A segment tag reconstruction strategy was used, and it means that a combination of an inner detector track with a muon spectrometer segment. The muon p_T is > 25 GeV, with $|\eta| < 2.4$.

Also, and isolated likelihood estimator is used; but for muons it is described as the scalar sum of the p_T of tracks with $p_T > 1$ GeV within a cone of $\Delta R = 0.4$ around the muon track, excluding the muon p_T.

Jet :

The jet reconstruction is made using an anti-K_T algorithm[11], with R = 0.4 from topo clusters calibrated using EM+JES calibration scheme (an AntiKt4TopoNewEM jet). The jets are requested to have $p_T > 30$ GeV, and over the range $|\eta|$ <2.5.

Missing Transverse Momentum :

The missing transverse momentum, E_T^{miss} is calculated from the energy deposed in all calorimeter cells and from muons. But certain correction is applied for the energy lost in the cryostat and different calibrations to the calorimeter cells.

The E_T^{miss} calibrated used for this analysis is called MET_Simplified20_RefFinal. The RefFinal refers to the refined calibration done as final step of the E_T^{miss} calibration, and it applies different weights to cells that belong to different reconstructed objects.

Trigger :

The trigger system achieves the required rejection power while retaining excellent sensitivity to the various physics signatures 6.3.1. In Chapter 4 it was explained that the architecture of the trigger is a three-level system: the first level is called L1, then the other two levels are L2 and EF (Event Filter). Each of the three trigger levels has a *trigger menu* which specifies thresholds and selection criteria according to the physics analysis requirements. Then the trigger menu could be read as follows: first it is indicated the trigger level (L1, L2 or EF), then the selected physics object identified using a notation where the symbol represents a particle type (e.g. e for electrons, mu for muons), followed by a E_T threshold value; and then any other requirement made. E.g., 2e5 = 2 or more electrons, with E_T value above 5 GeV.

Then, the triggers used for the current analysis are in Table 6.4.

[11]It is a jet clustering algorithm which behaves like an idealised cone algorithm [34].

Run Period	*Electron - Muon Trigger Requirement*
B-J	EF_e20_medium or EF_mu18
K	EF_e22_medium or EF_mu18_medium
L-M	EF_e22vh_medium1 or EF_e45_medium1 or EF_mu18_medium

TABLE 6.4: Triggers used for electron-muon analysis in data.

The triggers EF_e20_medium (single electron with E_T above 20 GeV using the medium variable), EF_e22_medium, EF_e22vh_medium1 (single electron prescaled by 10 with offline medium variable lepton trigger), EF_e45_medium1 are trigger scale factor for the electron with $p_T > 25$ GeV.

The triggers EF_mu18 and EF_mu18_medium are single muon triggers with E_T above 18. Medium implies a different weighting than only EF_mu18.

Other requirements are asked for the object definition: at least 3 associated vertex in the primary vertex; a removal of mis-identified jets as electrons or muons in a cone with $\Delta R = 0.4$.

6.3.2 Performance for Electrons

A summary of the signal electron definition used for the analysis: medium ID electron with p_T >25 GeV, $|\eta|$ <2.47 and Etcone40 < 10 GeV.

- Electron Transverse Momentum

  First of all it is important to do an analysis of how accurate has been the reconstruction of events, therefore for each detector simulation it was made a comparison between the truth variable (electron p_T) and the reconstructed one to inquire inefficiencies or programming errors during the reconstruction of the kinematic distribution.

FIGURE 6.1: Comparison of the electron p_T truth distribution and the reconstructed distribution for fullSim, sneutrino 100 GeV mass point.

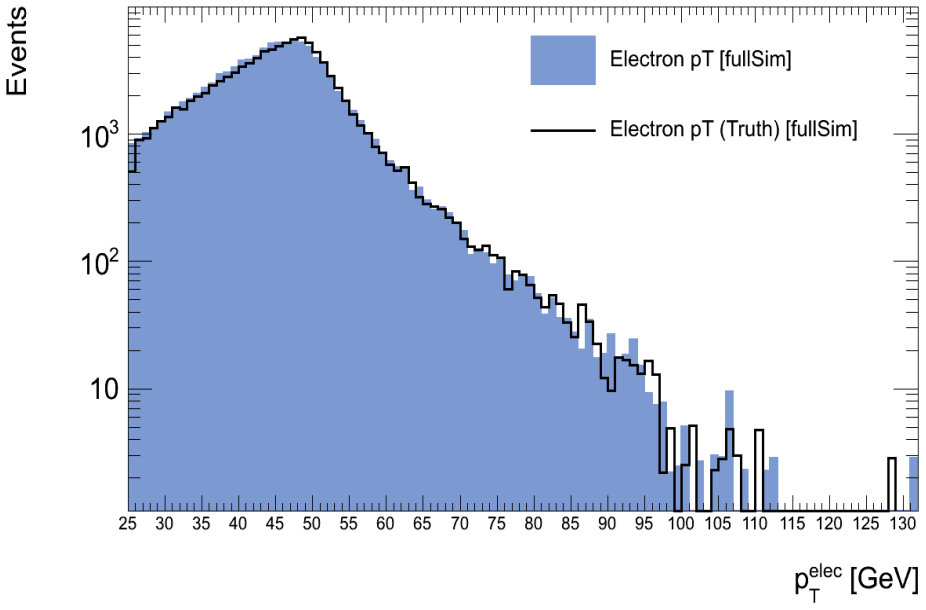

For the sneutrino 100 GeV mass point decaying into an electron-muon pair, the reconstruction of the electrons transverse momentum for full Geant4 simulation (Figure 6.1) shows agreement with the true distribution, which implies a good reconstruction of the electron p_T distribution for full Geant4 simulation. Also, the ATLFast-II distribution of the electrons p_T shows agreement between the true values and the reconstructed, and it also indicates a good reconstruction for ATLFast-II simulation (Figure 6.2).

Figure 6.3 shows the comparison between the ATLFast-II electron p_T distribution and the full Geant4 simulation distribution, and good agreement is found over the full range, despite the tail of the distribution after 100 GeV but those small differences could be neglected under the consideration that it represents around

FIGURE 6.2: Comparison of the electron p_T truth distribution and the reconstructed distribution for AF-II, emu100 mass point.

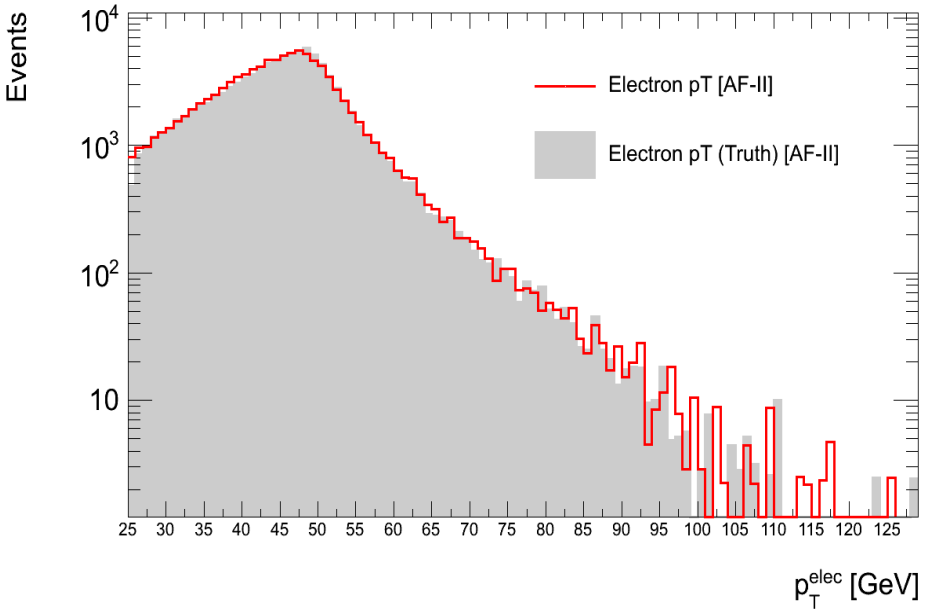

FIGURE 6.3: Comparison of electron p_T distribution for AF-II and fullSim for emu100 mass point.

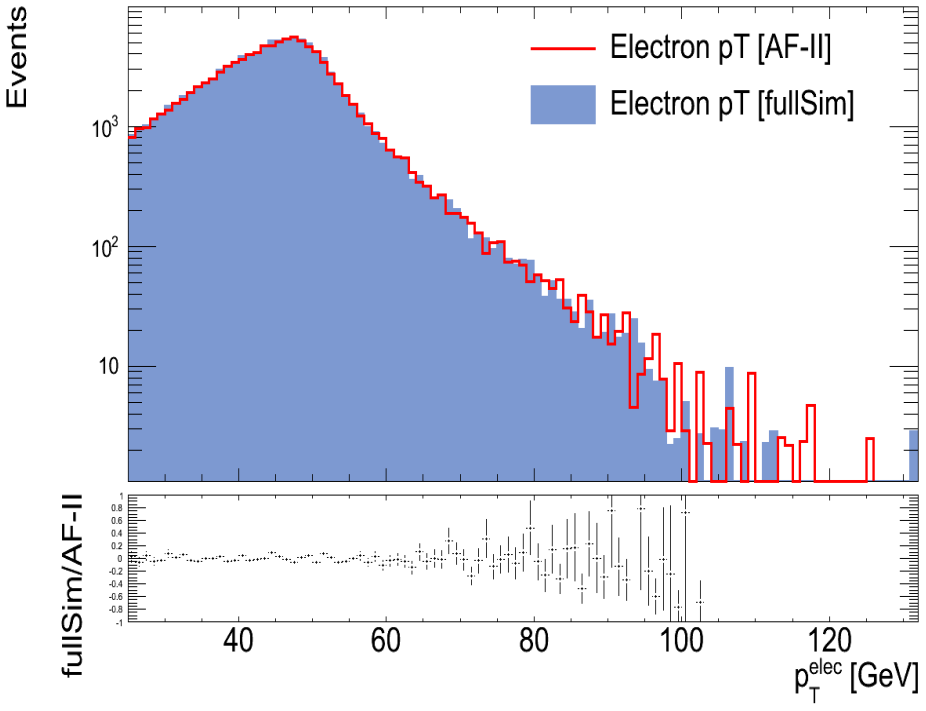

0.05% of the total statistical population and it is due to the simplifications in the simulation model. The aim of the ATLFast-II simulation is to provide a simulation where the key features of reconstructed object properties are well reproduced, and the differences in details due to the simplification in the model need to be accepted

as long as they do not lead to large and unpredictable differences at the physics analysis.

FIGURE 6.4: Comparison of the p_T truth distribution and the reconstructed distribution for fullSim, emu650 mass point.

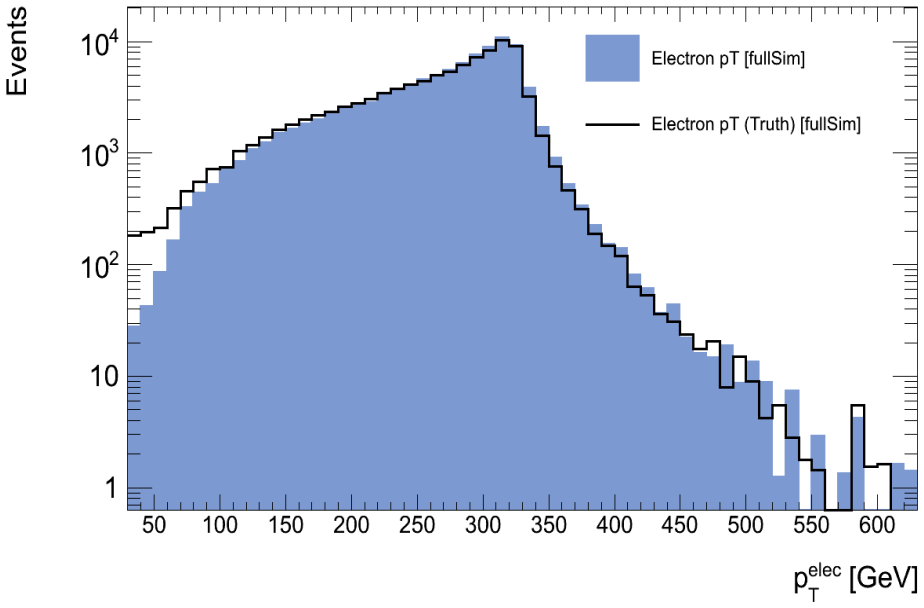

FIGURE 6.5: Comparison of the electron p_T truth distribution and the reconstructed distribution for AF-II, emu650 mass point.

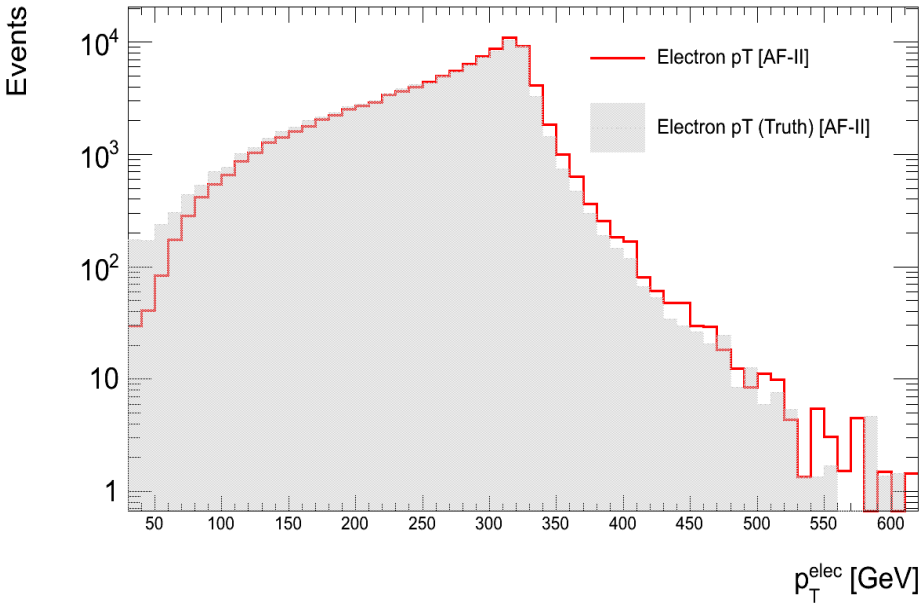

The comparison of the electrons transverse momentum, due to a sneutrino 650 GeV mass point, between the reconstructed values and the true values for both simulations show a good reconstruction of the electron p_T; except for 25 GeV $< p_T <$ 100 GeV, where the reconstructed distribution underestimates the number

of electrons with lower p_T (Figure 6.4 and Figure 6.5). But, the distributions show good agreement when ATLFast-II and full Geant4 simulation are superimposed (Figure 6.6) in spite of the behaviour of statistical population for lower electron p_T.

FIGURE 6.6: Comparison of electron p_T distribution for AF-II and fullSim for emu650 mass point.

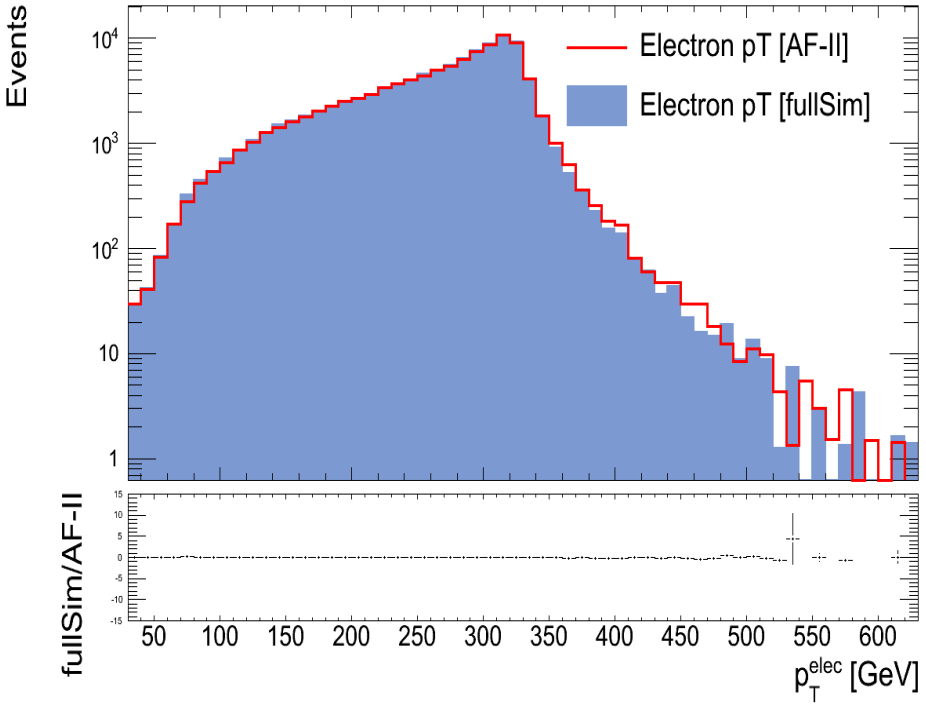

This underestimation could be generated by some failing in the electrons recognition during the reconstruction of events, where the electrons could be mis-identified as jets or photons. The same issue is found for electron p_T for the emu2000 samples simulated by ATLFast-II and full Geant4 simulation (Figure 6.7 and Figure 6.8), and it is almost in the same range for these samples.

In spite of the statistics population for lower p_T for the emu2000 samples, the full Geant4 simulation shows a good reconstruction of the physics object (Figure 6.7), but this is not entirely true for ATLFast-II reconstruction; in addition an overestimation of the distribution values beyond 1000 GeV is shown (Figure 6.8).

This overestimation is present also for ATLFast-II in the comparison with full Geant4 simulation, showing the main difficulty for ATLFast-II simulation: the reconstruction of the events in the tails. However, under the consideration that these events in the tail are not in the true distribution for ATLFast-II simulation, one might ask how many of those events are real electrons or fake electrons mis-identified. Then, it is needed a further study with better strategies to identify the fake and true electrons in the reconstruction.

FIGURE 6.7: Comparison of electron p_T truth distribution and the reconstructed distribution for fullSim, emu2000 mass point.

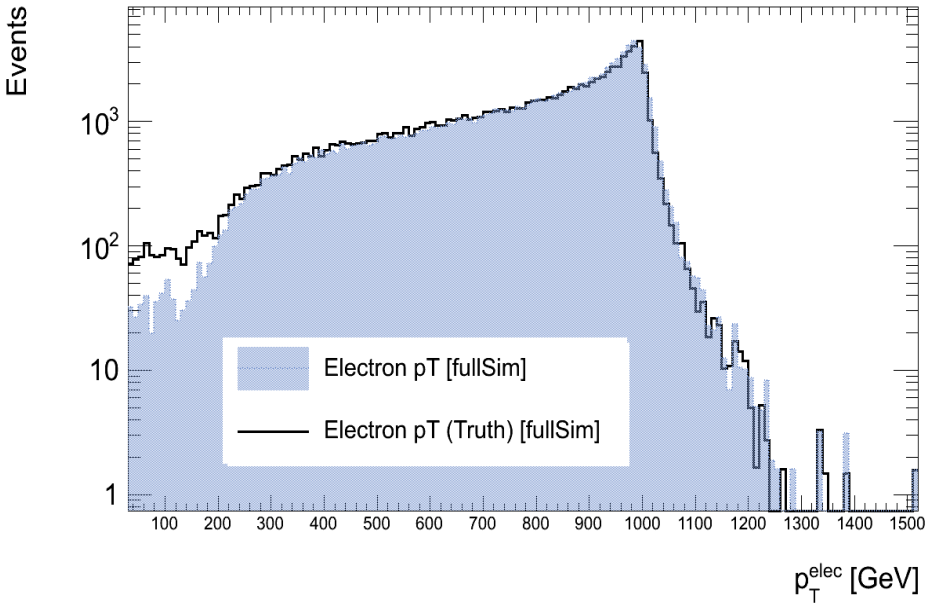

FIGURE 6.8: Comparison of the electron p_T truth distribution and the reconstructed distribution for AF-II, emu2000 mass point.

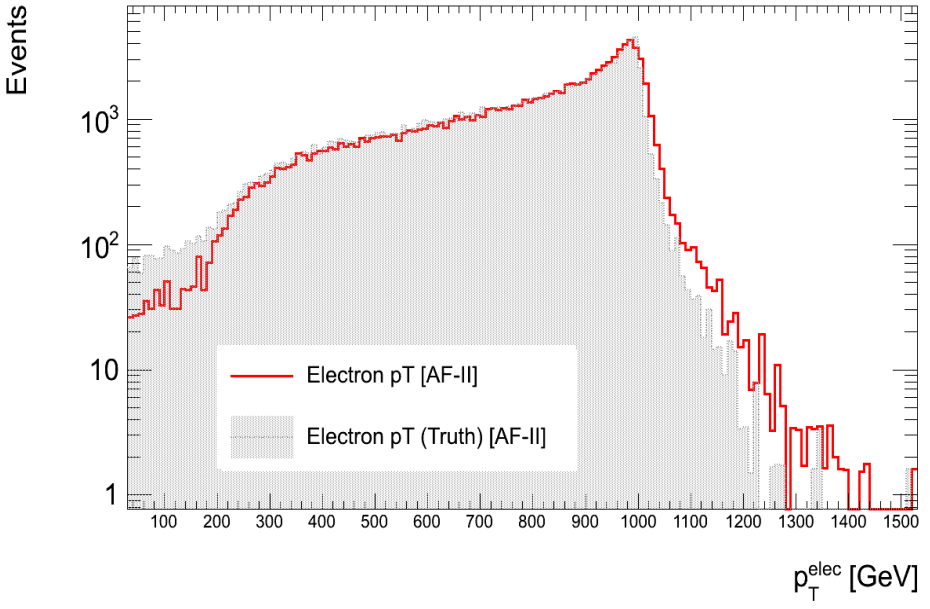

It is interesting to look at the electron p_T distribution for the emu650 samples (6.6), and to compare it with previous results for the electron p_T for a sneutrino 650 GeV mass point decaying into an electron-muon pair in Figure B.13. The mean value seems to go around 300 GeV for both distributions, indicating a first agreement for ATLFast-II with previous RPV SUSY results.

.

FIGURE 6.9: Comparison of electron p_T distribution for AF-II and fullSim for emu2000 mass point.

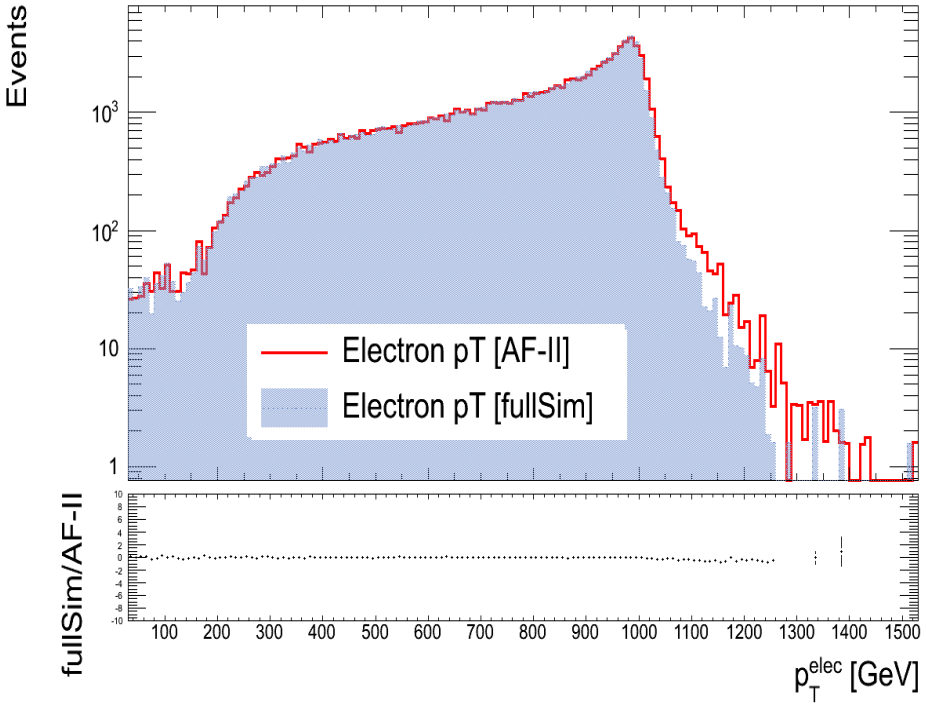

- Electron Pseudorapidity

  The pseudorapidity (η) (Chapter 4.2), which is used here to describe a kinematic condition of the electrons, presents a good agreement between ATLFast-II and full Geant4 simulation for all the electron-muon mass points as it is shown in Figure 6.10 (auxiliary plots showing the agreement for the lower sneutrino mass and the higher sneutrino mass are Figure B.1 and Figure B.2).

  The description of η given by ATLFast-II, and compared with full Geant4 simulation, shows a proper simulation done by fast simulation in less time and same accuracy.

- Electron Azimuthal Angle

  The electron azimuthal angle, ϕ (Chapter 4.2), distribution for ATLFast-II also shows a good agreement with full Geant4 simulation for all mass points; it is possible to see in Figure 6.11 that the ratio between the events of ATLFast-II and full Geant4 simulation approaches zero indicating that the efficiency difference is < 5 % (Auxiliary plots showing the agreement for the lower sneutrino mass and the higher sneutrino mass are Figure B.3 and Figure B.4).

  Therefore, the electron ϕ distribution (just as the electron η distribution) is accurately simulated by ATLFast-II. Both objects, ϕ and η, are simulated mainly by

FIGURE 6.10: Comparison of the electron pseudorapidity distribution for emu650 mass point.

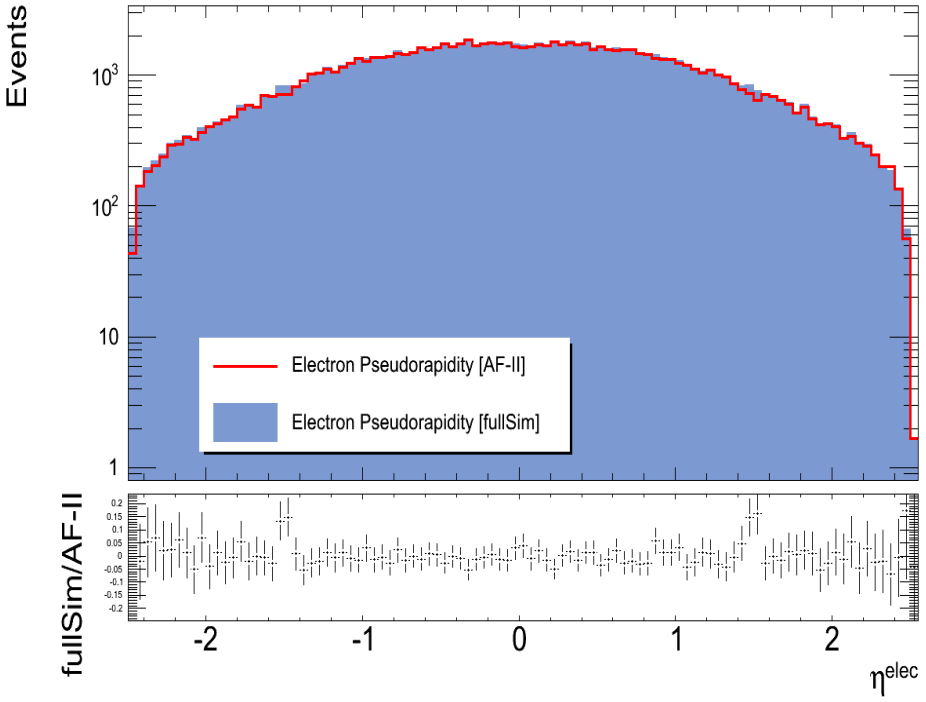

the inner detector, then their good accuracy should be expected, under the fact that the inner detector simulation is the same for ATLFast-II and full simulation.

FIGURE 6.11: Electron azimuthal angle distribution for emu650 mass point.

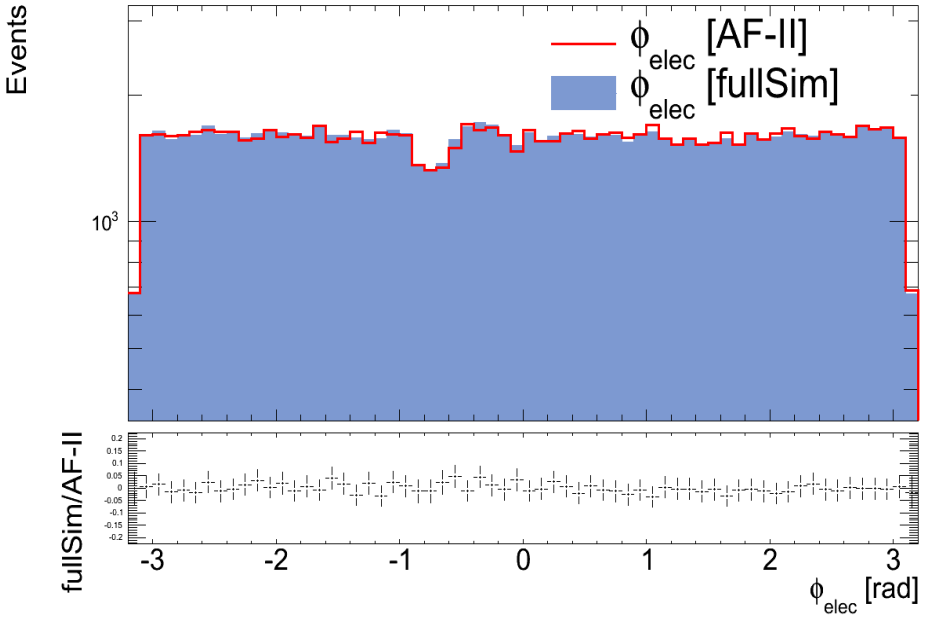

6.3.3 Performance for Muons

As explained in Chapter 5, ATLFast-II muons are simulated using full Geant4 simulation. In general, a good agreement between the kinematic distributions for muon is expected: differences could only arise from energy depositions in the calorimeter, affecting the isolation condition and punch-through muons (a hadron which enters the calorimeter and produces hits in the muon system).

A summary about the muons object definition: Staco combined muons (see object definition 6.3.1), with p_T >25 GeV, $|\eta|$ <2.4 and isolation ptcone40 <10 GeV.

- Muon Transverse Momentum

  It is also important to study how accurate has been the muon reconstruction of events and to quantify the success of the reconstruction, so a comparison between the muon p_T truth values and the reconstructed was made for each sample and for both detector simulations.

FIGURE 6.12: Comparison of the muon p_T truth distribution and the reconstructed distribution for fullSim, emu100 mass point.

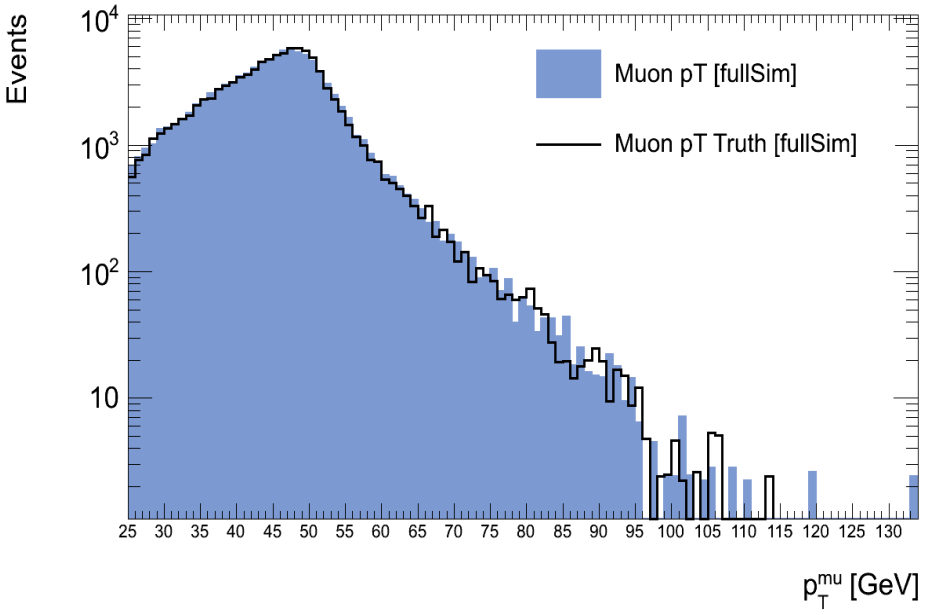

For the sneutrino 100 GeV mass point samples, it is found a good agreement over the full range when the true muon p_T distribution is compared with the muon p_T reconstructed distribution, pointing then an accurately reconstruction by full Geant4 simulation (Figure 6.12) and ATLFast-II (Figure 6.13).

For these samples, sneutrino 100 GeV mass point samples, the muon p_T description done by AF-II is consistent with the expectations by having a good agreement with

FIGURE 6.13: Comparison of the muon p_T truth distribution and the reconstructed distribution for AF-II, emu100 mass point.

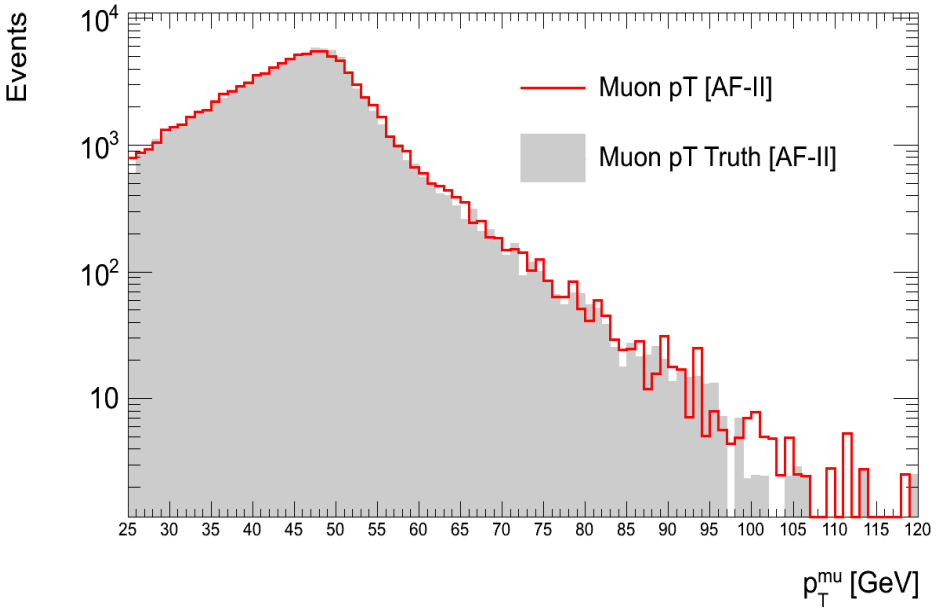

FIGURE 6.14: Comparison of the AF-II muon p_T distribution and fullSim muon p_T distribution for emu100 mass point.

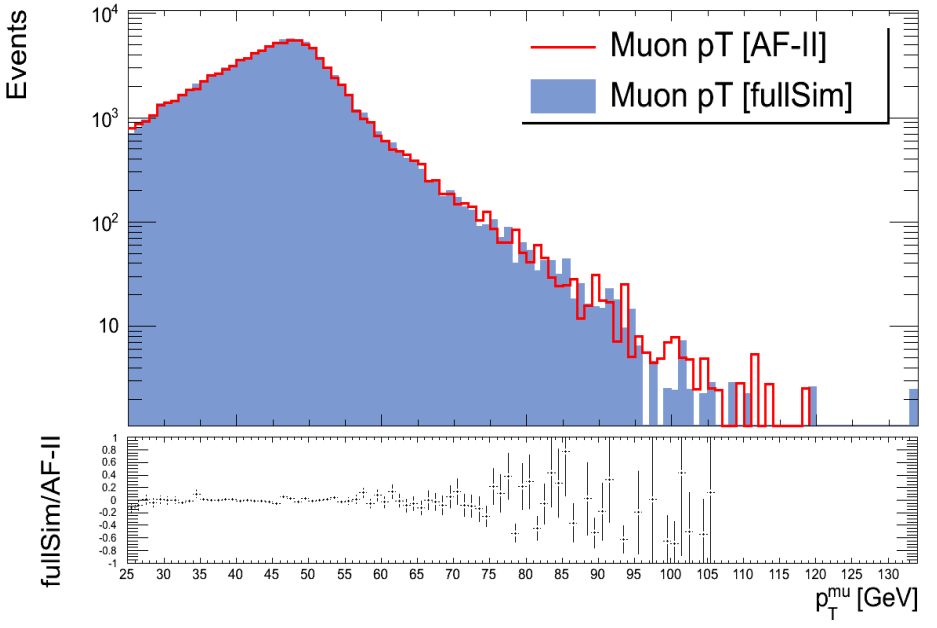

the fullSim distribution (6.14). The differences between the distributions is less than 10% nearly over the full range, as the ratio shows.

Similar, for the sneutrino 650 GeV mass point samples, the muon p_T distributions comparing the true values and the reconstructed shows in a general way a good reconstruction of the object done by full Geant4 simulation (Figure 6.15) and ATLFast-II (Figure 6.16); but, after 300 GeV an overestimation of the muons is

FIGURE 6.15: Comparison of the Muon p_T truth distribution and the reconstructed distribution for fullSim, emu650 mass point.

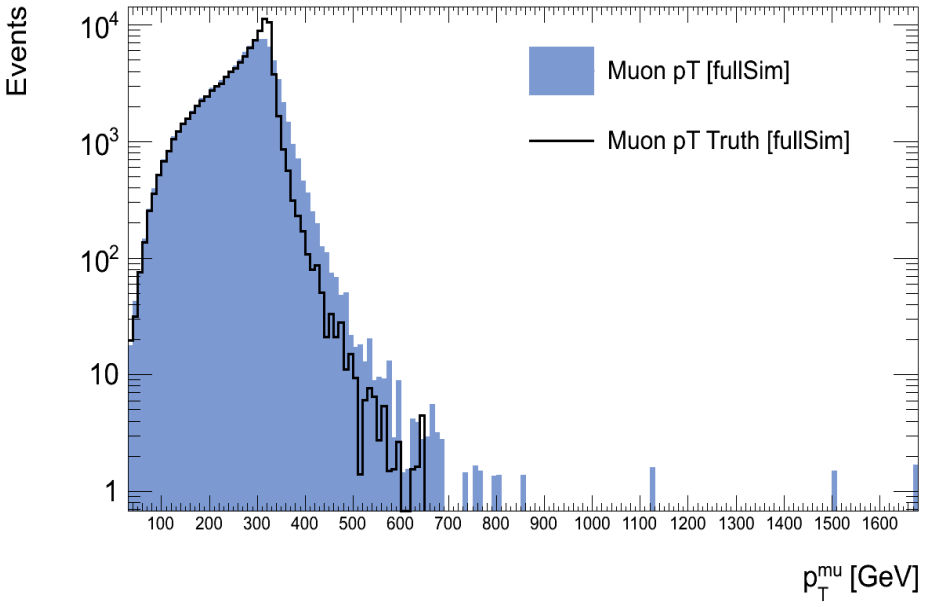

FIGURE 6.16: Comparison of the Muon p_T truth distribution and the reconstructed distribution for AF-II, emu650 mass point.

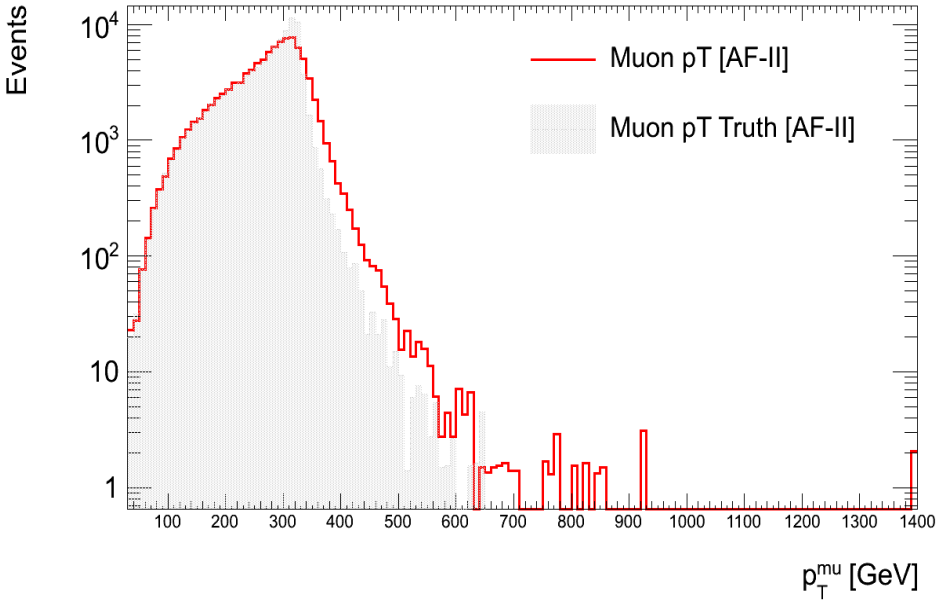

shown when the reconstructed values are compared with the true. The same issue is observed for the emu2000 samples comparison between the true and the reconstructed muon p_T distribution: an overestimation after the peak of the distribution (around 1000 GeV) for full Geant4 simulation (Figure 6.18) and for ATLFast-II (Figure 6.19).

But this overestimation of the muon values is observed only when comparing the

reconstructed objects and the true information stored. For instance for emu650 samples the muon p_T distribution is accurately simulated by ATLFast-II, showing a good agreement nearly over the range for both simulations (Figure 6.17).

FIGURE 6.17: Comparison of the AF-II muon p_T distribution and fullSim muon p_T distribution for emu650 mass point.

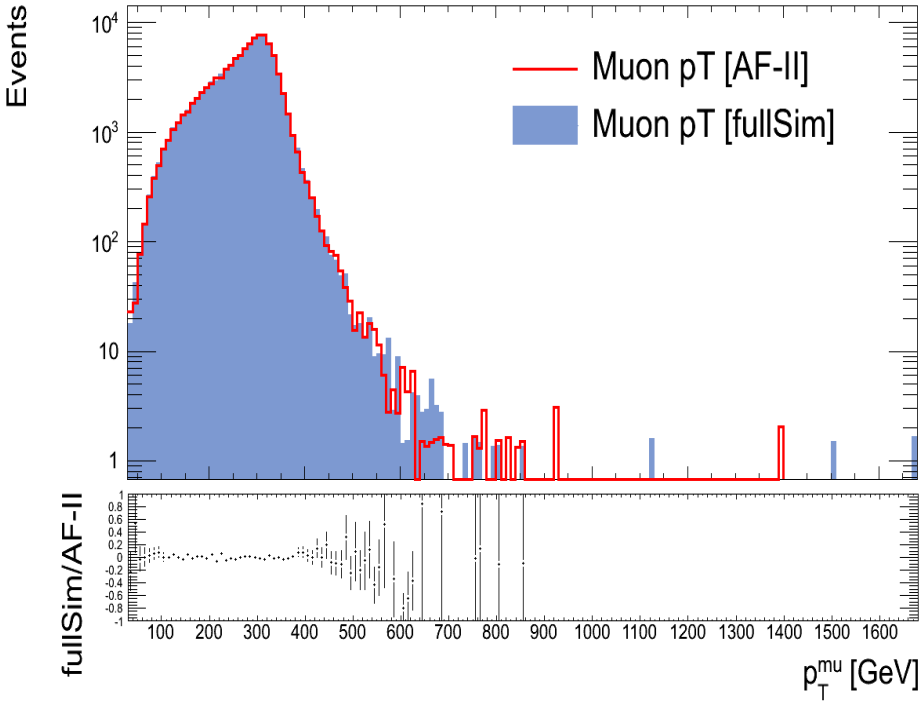

FIGURE 6.18: Comparison of the Muon p_T truth distribution and the reconstructed distribution for fullSim, emu2000 mass point.

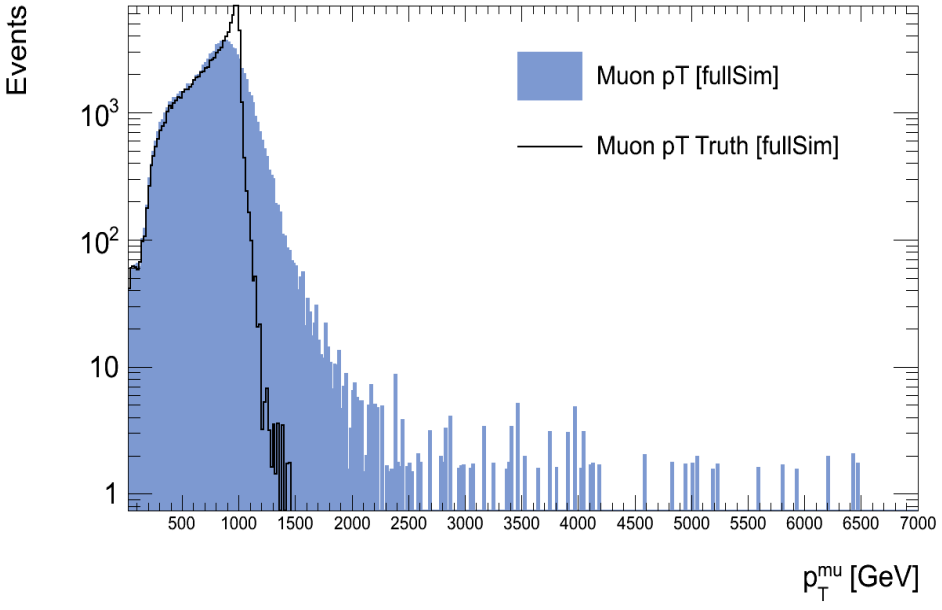

FIGURE 6.19: Comparison of the muon p_T truth distribution and the reconstructed distribution for AF-II, emu2000 mass point.

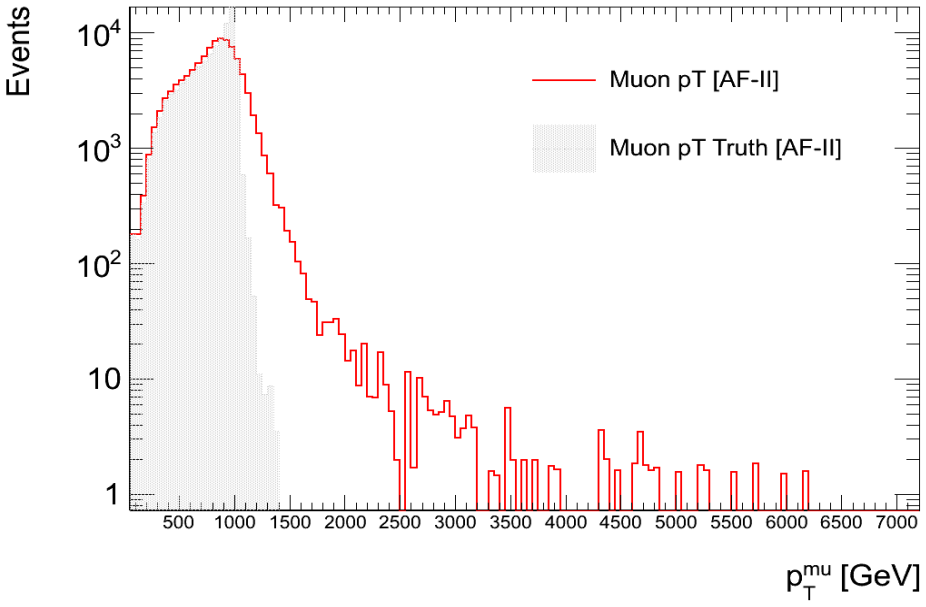

The same happens for the emu2000 samples, where the distribution has a good agreement between ATLFast-II and full Geant4 simulation (Figure 6.20) despite of the behaviour of the reconstructed and true comparison. Furthermore, the peaks for the reconstructed muon p_T distributions are in the positions expected for a sneutrino of 650 GeV mass and 2000 GeV mass.

FIGURE 6.20: Comparison of the AF-II muon p_T distribution and fullSim muon p_T distribution for emu2000 mass point.

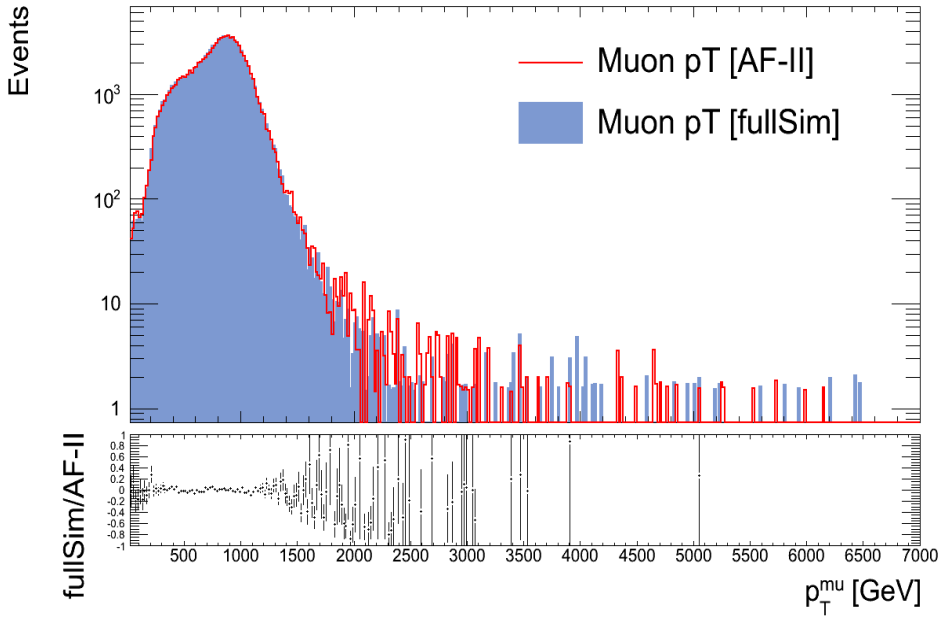

Those differences between the true and the reconstructed information for the muon p_T distribution could be due to resolution for muons p_T; an ATLAS study about the relationship between the muon p_T and its resolution indicates that the expected muon resolution will increase as the muon p_T increases when muon p_T is larger than ~30 GeV, and it is shown in the Figure 6.21. This may justify why the differences between true and reconstructed are larger when the expected p_T increases.

FIGURE 6.21: The muon resolution (ATLAS result); where it is possible to observe the "contributions to the momentum resolution for muons reconstructed in the Muon Spectrometer as a function of transverse momentum for $|\eta| < 1.5$". Then, "the alignment curve is for an uncertainty of 30~ μm in the chamber positions" [35]. ATLAS Experiment ©2012 CERN.

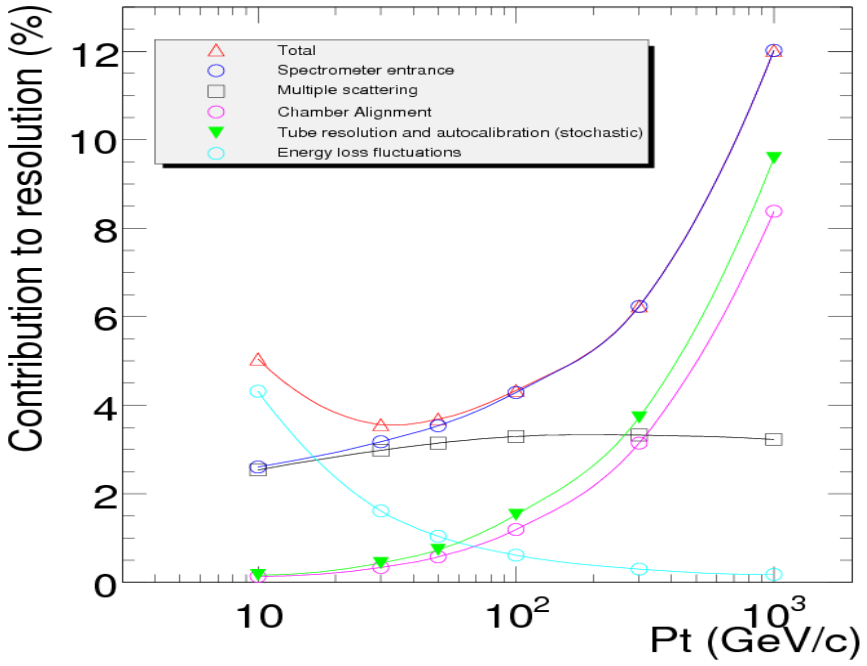

Besides all these results, it is possible to do another comparison for emu650 samples between the muon p_T distribution showed in Figure 6.17 with the muon p_T distribution from [5] (Figure B.14). The distribution generated here by ATLFast-II (and full Geant4 simulation) seems to be consistent with the result expected for the RPV SUSY model described earlier, where the mean value is around 350 GeV. This result demonstrates an accurate object simulation performed by ATLFast-II.

- Muon Isolation Variable

  The muon isolation variable used in this analysis was *etcone40*, which gives the distribution of the isolation energy (E_T) in a cone of radius (ΔR) 0.4.

  Even when muons are full Geant4 simulated, and a good agreement is expected (as it was showed for the muon p_T distributions), the differences could arise from the energy depositions in the calorimeter affecting the isolation condition and punch-through muons. In the configuration of the ATLFast-II simulation used with these samples, muons are ignored and no energy deposition for muons in the calorimeter is applied.

FIGURE 6.22: Comparison of AF-II muon etCone isolation distribution and fullSim distribution for emu100 mass point.

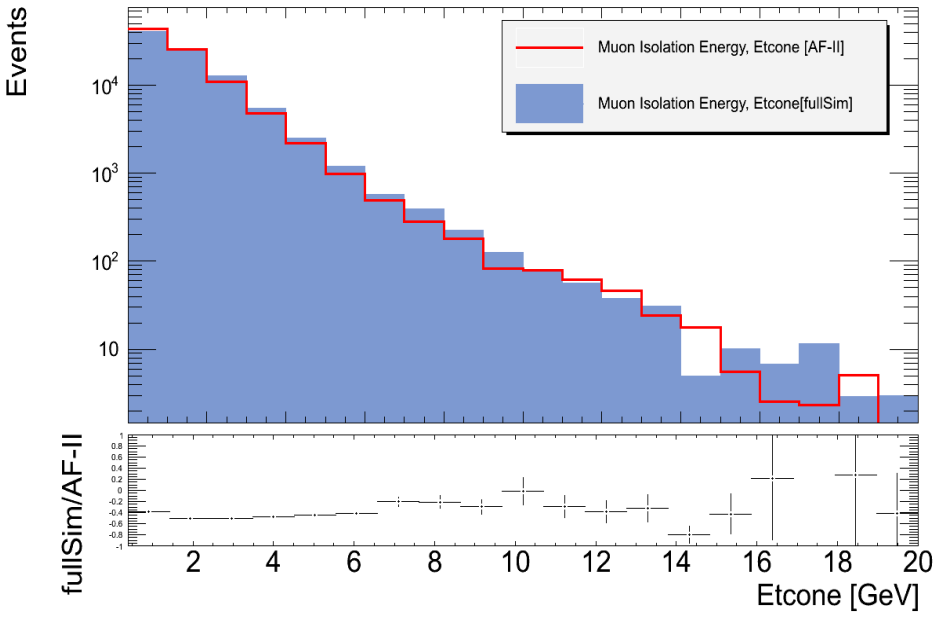

The etcone distribution for emu100 samples shows good agreement for ATLFast-II simulation with full Geant4 simulation nearly all the range (6.22), but as expected and underestimation of the number of events is shown, around 16 GeV, due to the absence of energy depositions on the calorimetry.

Also, for emu650 samples (Figure 6.23) and emu2000 samples (Figure 6.24) a good agreement would be expected between AF-II isolation distribution and fullSim, but AF-II simulation is generating some events where fullSim does not show any. These extra events are due to the deficiency of energy deposited by the muon in the calorimeter. Then, as it is not applied any simulation of the muon energy loss in the calorimeter or a simulation of the punch-through muons, it is possible to say that the isolation cuts for ATLFast-II are too soft, and fake events are generated.

FIGURE 6.23: Comparison of AF-II muon etCone isolation distribution and fullSim distribution for emu650 mass point.

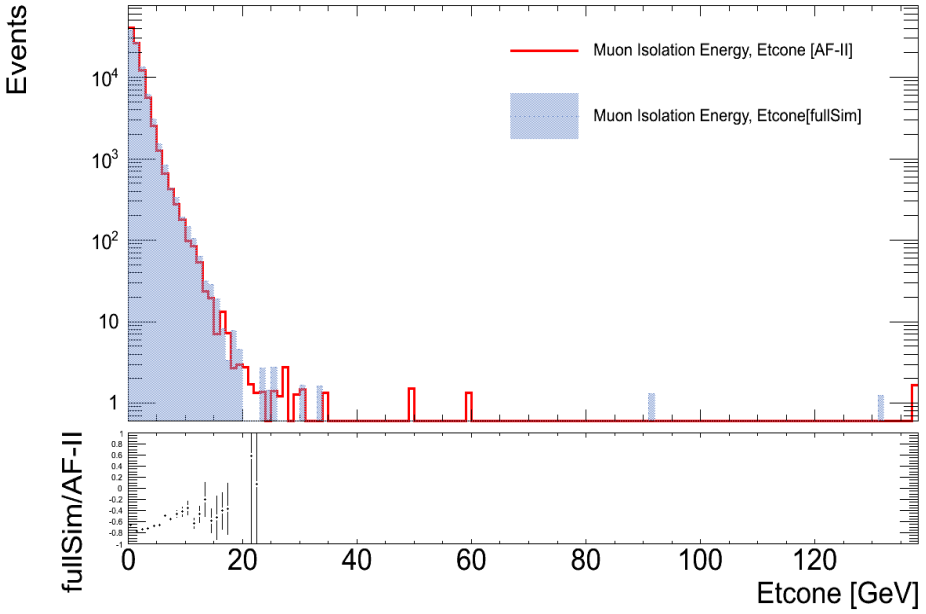

FIGURE 6.24: Comparison of AF-II muon etCone isolation distribution and fullSim distribution for emu2000 mass point.

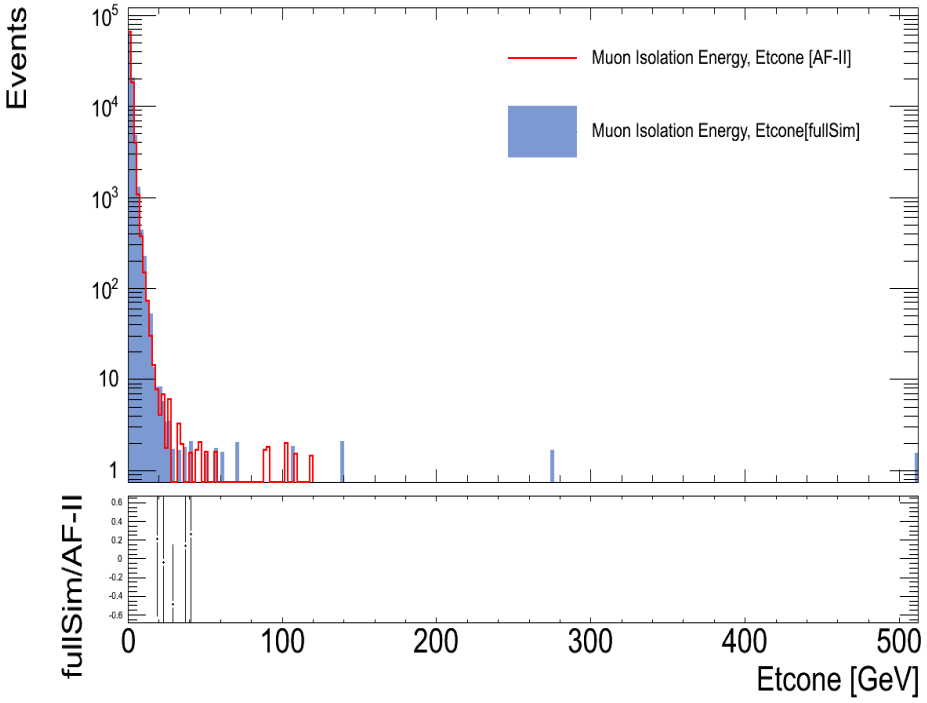

- Muon pseudorapidity

  The muon pseudorapidity, η, as expected has a good agreement between the description given by ATLFast-II distribution and full Geant4 simulation, in fact the ratio goes to zero for all sneutrino mass points as it goes in Figure 6.25 (Auxiliary plots showing the muon pseudorapidity distribution for lower sneutrino B.5 and higher sneutrino B.6). As a result, together with the electron η, the pseudorapidity can be regarded as evidence of the good description done by AF-II.

FIGURE 6.25: Comparison of the muon pseudorapidity AF-II and fullSim distribution for emu650 mass point.

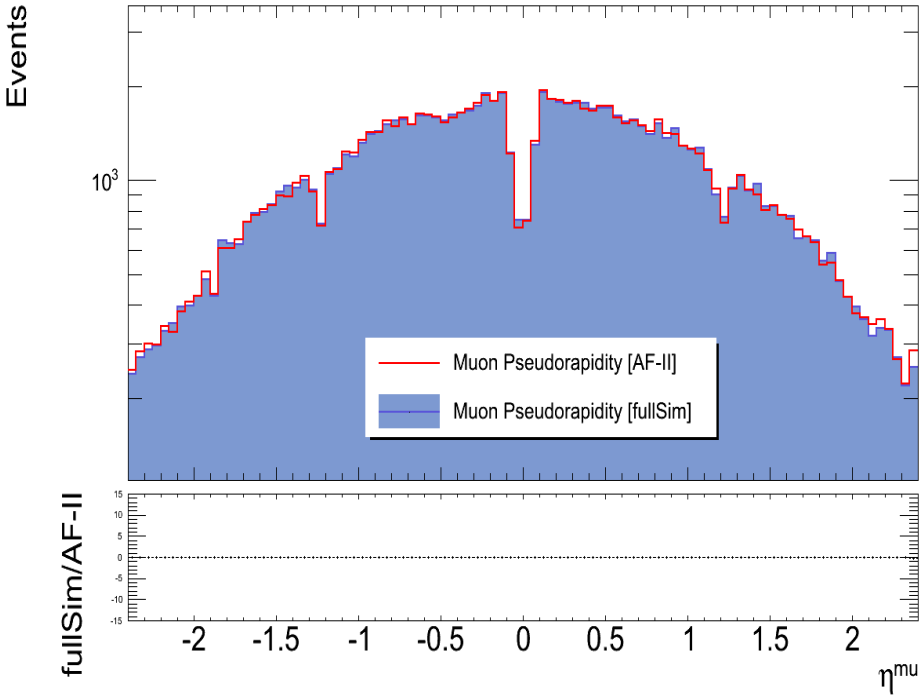

- Muon Azimuthal Angle

  The muon azimuthal angle distribution, ϕ, for all mass points meets expectations of a good agreement between AF-II physics objects description and fullSim as it is shown in Figure 6.26 (see auxiliary plots for sneutrino 650 GeV B.7 and sneutrino 2000 GeV B.8 azimuthal angle distribution). Furthermore the ratio approaches zero for almost all the comparison points.

- Difference between the Azimuthal Angles of the Electrons and the Muons

  The difference between azimuthal angles of the electron and the muon is called $\Delta\phi$. A good agreement is expected for all mass points for this variable.

  Yet for the sneutrino 100 GeV mass point, see the auxiliary plot Figure B.9. There is a good agreement in almost all the distribution. Some events around zero were

FIGURE 6.26: Comparison of the muon ϕ AF-II and fullSim distribution for emu100 mass point.

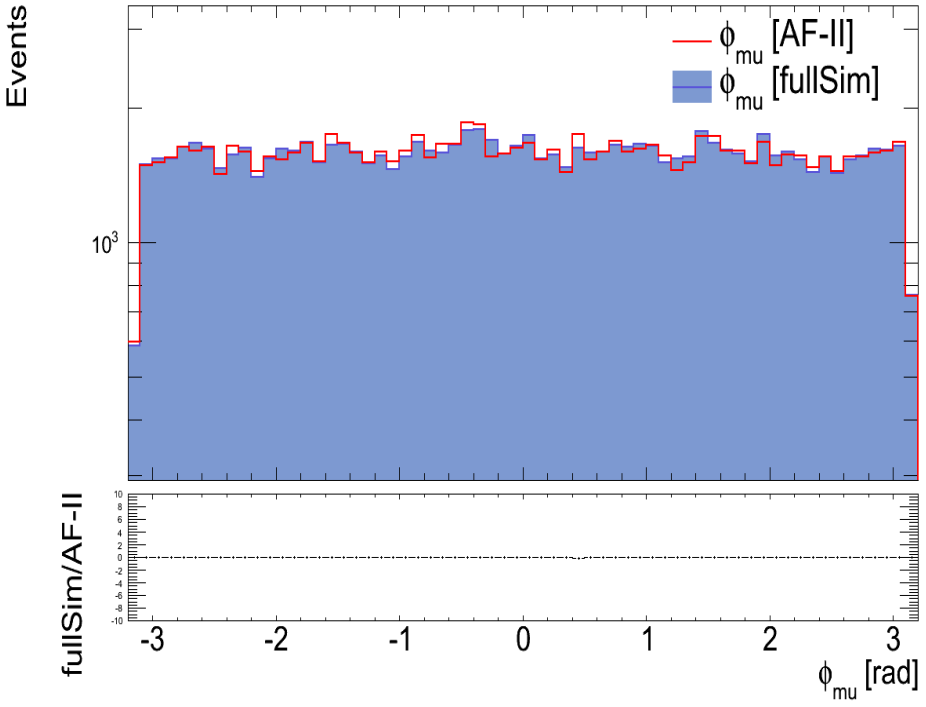

reconstructed for ATLFast-II but not for full Geant4 simulation. The agreement, however does not show any considerable gap.

FIGURE 6.27: Comparison of $\Delta\phi$ AF-II distribution and fullSim distribution for emu650 mass point.

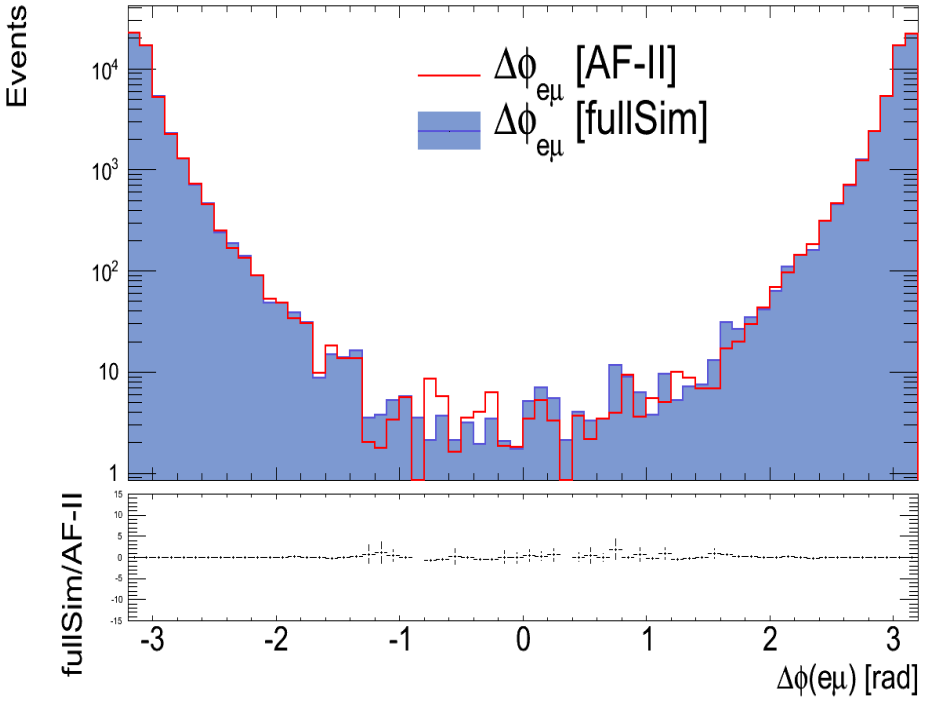

The $\Delta\phi$ distribution for the sneutrino 650 GeV mass point (6.27) did not show a poor agreement between ATLFast-II distribution and full Geant4 simulation distribution, but the agreement is not as good as it was observed for ϕ_{elec} or ϕ_{mu} before (Figure 6.11 and Figure B.7). But just as the sneutrino 100 GeV mass point, there are not large discrepancies in the comparison AF-II/fullSim.

Around zero for the sneutrino 2000 GeV mass point, the ATLFast-II and full Geant4 simulation $\Delta\phi$ distributions (Figure B.10) do not have great similarities. But, at each side of the plot the agreement between them is good.

In general terms, around zero it is applied an overlap removal, where electrons and muons very close each other are rejected to decrease the chance of mis-measuring them. However, it seems to be more complicated to distinguish fake and real electrons when they are too energetic, as it was stated before, for ATLFast-II so the differences could be focused in this small disagreement.

6.3.4 Performance for Jets

The calorimeter system is the principal detector for jet reconstruction, so a good agreement between the ATLFast-II jets reconstruction and full Geant4 is important. This implies that as the performance of the jets are more sensitive to the calorimeter reconstruction a good agreement will mean that the FastCaloSim, and therefore the ATLFast-II, parametrisation was good enough to model the full simulated calorimeters behaviour.

Moreover, jet performance is an important part of the SUSY analysis and therefore a good reconstruction will imply that the fast simulation done with ATLFast-II is acceptable for jets in RPV SUSY.

A summary of the jets requirements: $p_T > 30$ GeV, $|\eta| < 2.5$ and the jet algorithm information AntiKt4TopoNewEM (6.3.1).

- Jet Transverse Momentum

  The jet transverse momentum, p_T, and its systematic uncertainty of the jet energy scale (JES) were determined for each mass points. The jet energy scale calibrates the measured calorimeter level jet energy to the particle level [36]; jet measurements are affected by a multitude of effects of different origin and this calibration accounts for non-compensation, dead material and other detector effects, as well as systematical bias of the response of different parts of the detector as a function of the jet transverse momentum and rapidity. The calibration of the JES should ensure the correct measurement of the average energy across the whole detector.

FIGURE 6.28: Comparison of the jets p_T distribution for AF-II and fullSim with its corresponding JES uncertainty variation for emu100 mass point.

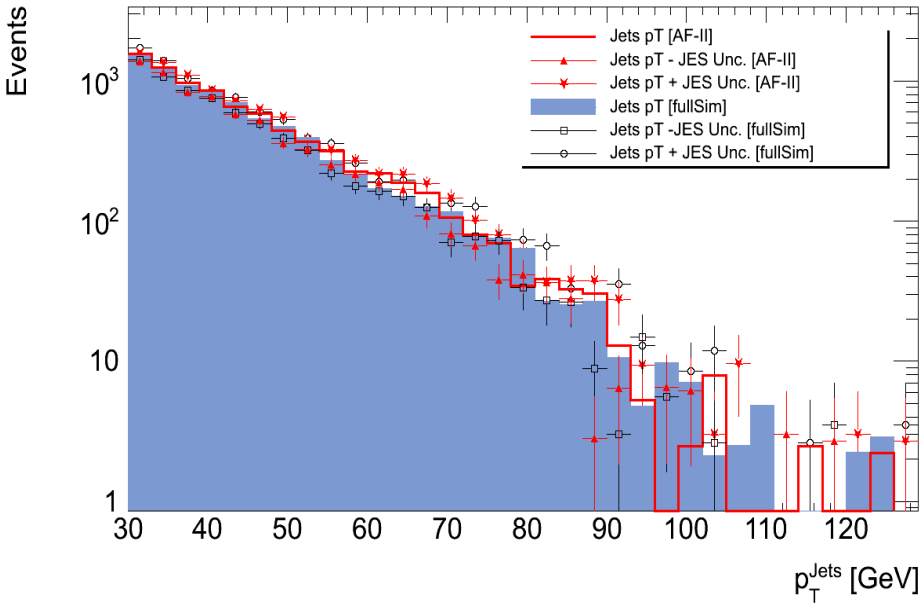

The interception belonging to the jets p_T ATLFast-II distribution (red line) and the jets p_T full Geant4 simulation distribution (blue area) for the sneutrino 100 GeV mass point is shown in Figure 6.28. Broadly ATLFast-II has a behaviour consistent with full Geant4 simulation, and any other part of the distribution where full Geant4 simulation and ATLFast-II seems to disagree are within the JES uncertainty.

FIGURE 6.29: Comparison of the jets p_T distribution for AF-II and fullSim with its corresponding JES uncertainty variation for emu650 mass point.

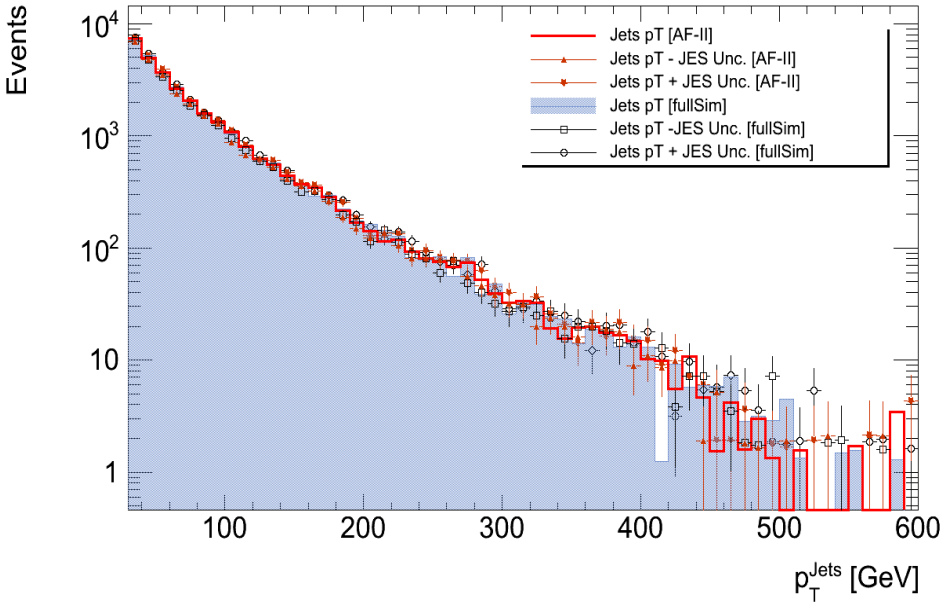

For the sneutrino 650 GeV mass point, the interception of the ATLFast-II and full Geant4 simulation areas belonging to the jet p_T distribution (area under the red line and blue surface respectively) shows more similarities between the simulations (Figure 6.29), even in the tail where the agreement for the sneutrino 100 GeV mass point was worse. Although emu100 and emu650 mass points have less jets generated by AF-II, both distributions show resemblance.

FIGURE 6.30: Comparison of the jets p_T distribution for AF-II and fullSim with its corresponding JES uncertainty variation for emu2000 mass point.

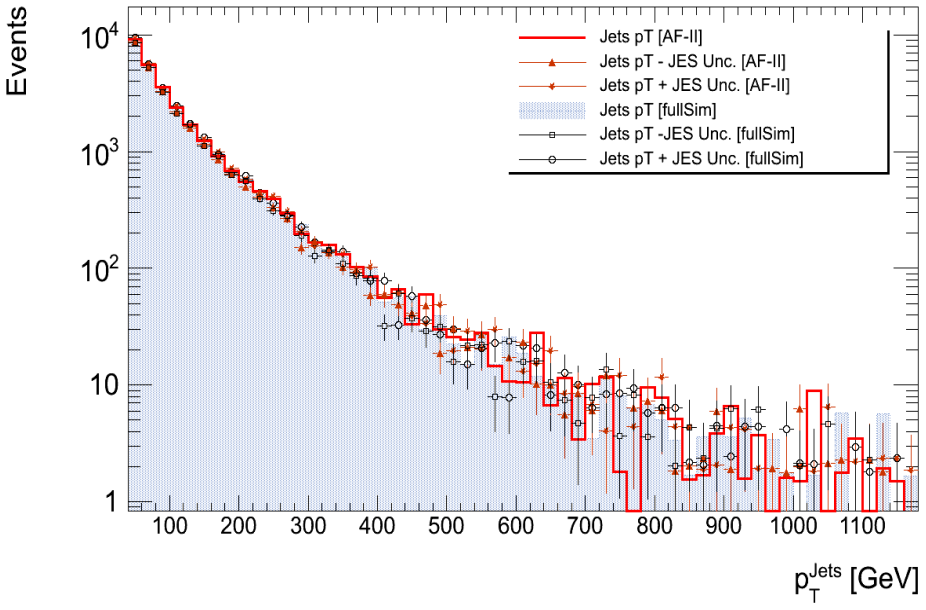

The interception area for the sneutrino 2000 GeV mass point, and agreement, is shown in Figure 6.30, where the ATLFast-II p_T distribution is the area under the red line while the full Geant4 simulation p_T distribution is the blue area. This figure points that almost every data of the distributions are similar; but, once again, where the main distributions seems to fail in the agreement, the values are within the JES uncertainty and as a result the agreement between AF-II and fullSim is good.

- b-tagged Jet Transverse Momentum

  Loosely defined, jets are colour singlets produced from quarks and gluons emerged from the proton-proton collision: for instance, b-jets are jets originated from bottom quarks and they are also known as b-tagged jets.

  The b-jet transverse momentum, p_T, was determined for each event together with the JES systematic uncertainty for each mass point in the same way it was done for non b-tagged jets. Since b-tagging performance depends on the performance

of the inner tracker, ATLFast-II simulation is expected to show good agreement with the results obtained in full Geant4 simulation.

The b-jets p_T distribution for the sneutrino 100 GeV mass point generated by ATLFast-II (area under the red line) and its intersection with the distribution generated by full Geant4 simulation (blue area) is shown in Figure 6.31; both distributions shows good agreement within the JES uncertainty and despite the events in the tail of the distributions (> 80 GeV).

FIGURE 6.31: Comparison of the bjets p_T distribution for AF-II and fullSim with its corresponding JES uncertainty variation for emu100 mass point.

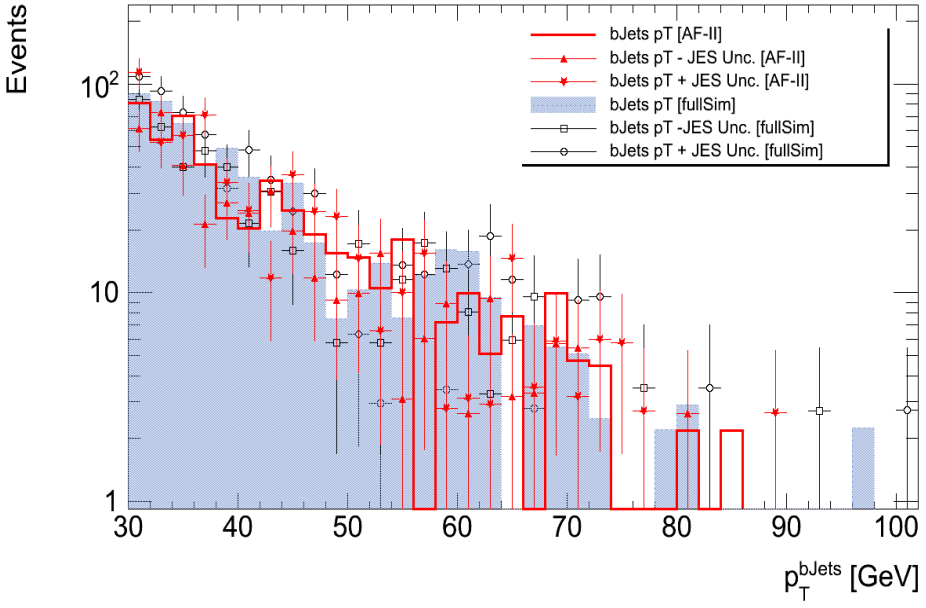

For the sneutrino 650 GeV mass point the Figure 6.32 shows a good agreement between ATLFast-II and full Geant4 simulation distributions until 200 GeV, where the description done by each simulation differs and there is a small deficit in the events generated by AF-II. Nevertheless, some of those points generated by AF-II that do not match with fullSim are within the JES uncertainty, enabling the difference to be neglected there.

The agreement shown for the sneutrino 2000 GeV mass point in Figure 6.33, states two important aspects: a good correlation (≥ 300 GeV) between ATLFast-II and full Geant4 simulation for lower bjet p_T distribution and agreement within JES uncertainty consideration (between 300 GeV and 600 GeV) and a deficit of events generated by AF-II in the tail of the distribution (> 600 GeV) which goes against the expected results. It is possible that some backsplashes from the calorimeter distort the tracking and b-tagging capabilities, giving as a result the events shown.

FIGURE 6.32: Comparison of the bjets p_T distribution for AF-II and fullSim with its corresponding JES uncertainty variation for emu650 mass point.

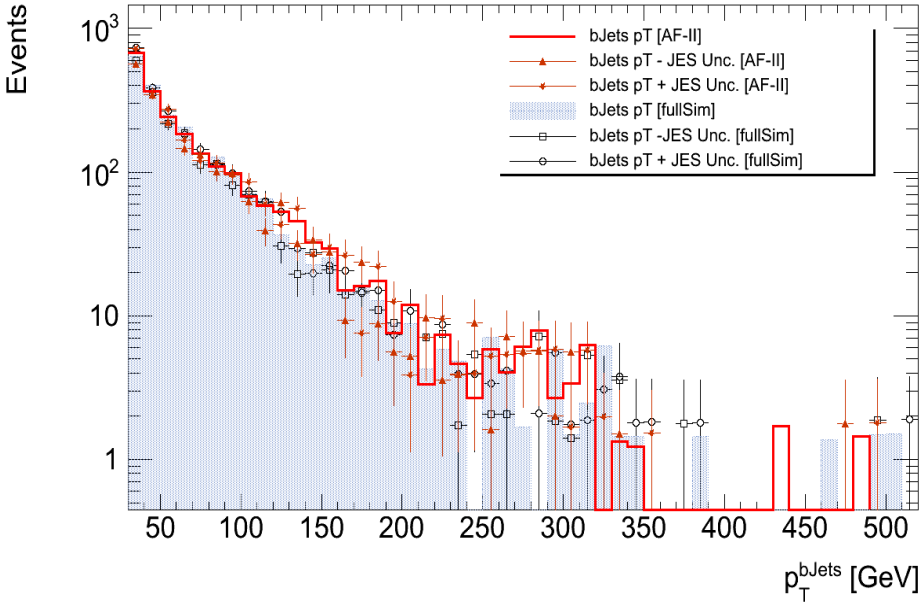

FIGURE 6.33: Comparison of the bjets p_T distribution for AF-II and fullSim with its corresponding JES uncertainty variation for emu2000 mass point.

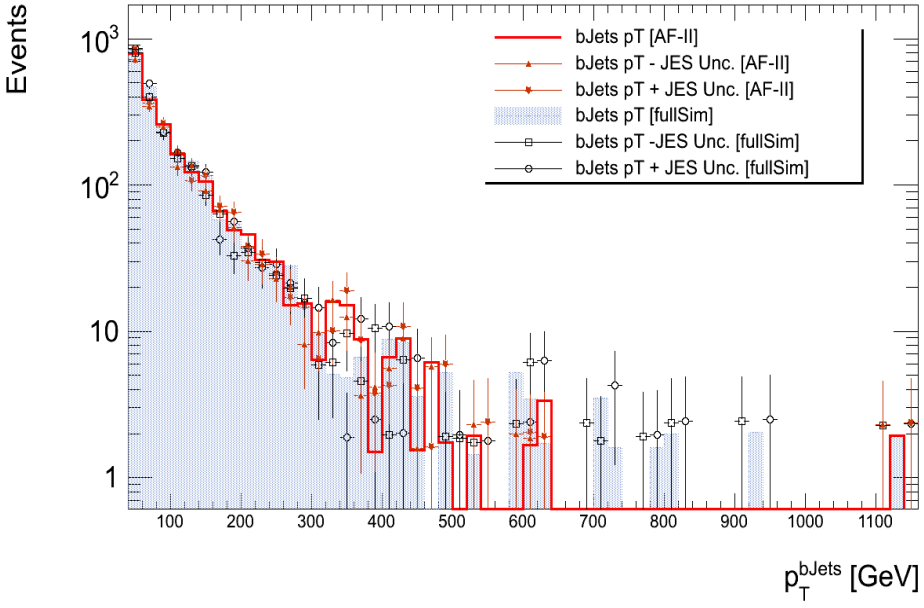

- Jet Timing

  The jet timing, t_{jet}, is the deviation of the event time from the time of energy deposition for the detector cells related to the jet, weighted by their energy squared. In other words it is the energy squared cells mean time. Real jets are expected to be *in-time* and therefore the mean of the distribution for real jets is around zero. *Out-of-time* jets (typically with $t_{jet} > 25$ ns) indicate (fake) jets originated by non-collision sources such as machine-induced (beam gas or beam halo muons) or cosmic ray background.

FIGURE 6.34: Comparison of AF-II and fullSim t_{jet} distribution for emu100 mass point.

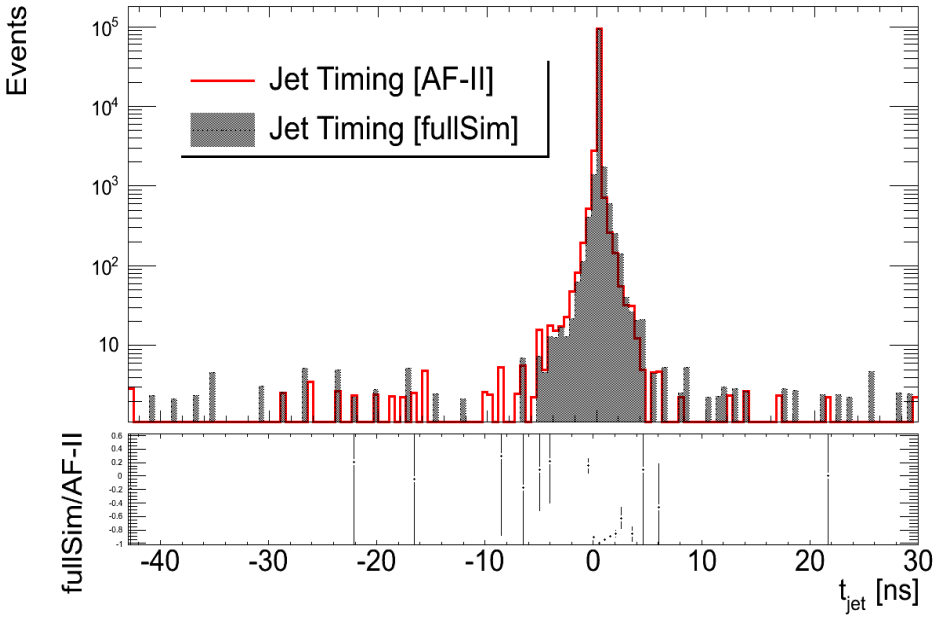

Jet timing distribution for the sneutrino 100 GeV mass point (Figure 6.34) has its mean value at zero for both simulations. The agreement is so good for *in-time* jets that the it is hard to distinguish them in Figure 6.34. But the ATLFast-II distribution shows less *out-of-time* jets (tail of the distribution) in contrast with full Geant4 simulation distribution.

For the sneutrino 650 GeV mass point, the ATLFast-II t_{jet} distribution has a good agreement with full Geant4 simulation t_{jet} distribution for *in-time* jets. Furthermore, even the number of jets *out-of-time* for ATLFast-II shows a good agreement at the distribution, which results in a better agreement than for the emu100 sample as Figure 6.35 shows.

The mean value of the ATLFast-II sneutrino 2000 GeV mass point t_{jet} distribution agrees with the distribution generated by full Geant4 simulation (6.36); although ATLFast-II shows more *out-of-time* jets than before, and more than full Geant4

FIGURE 6.35: Comparison of AF-II and fullSim t_{jet} distribution for emu650 mass point.

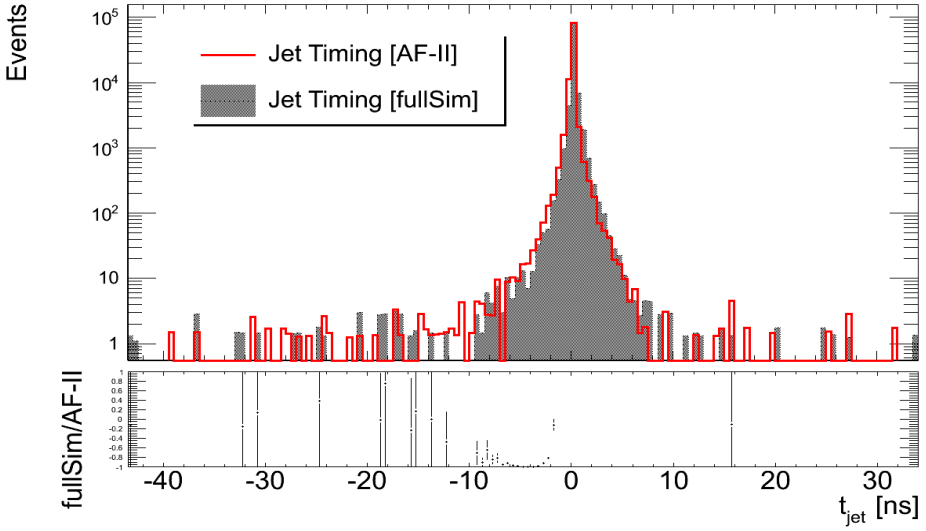

FIGURE 6.36: Comparison of AF-II and fullSim t_{jet} distribution for emu2000 mass point.

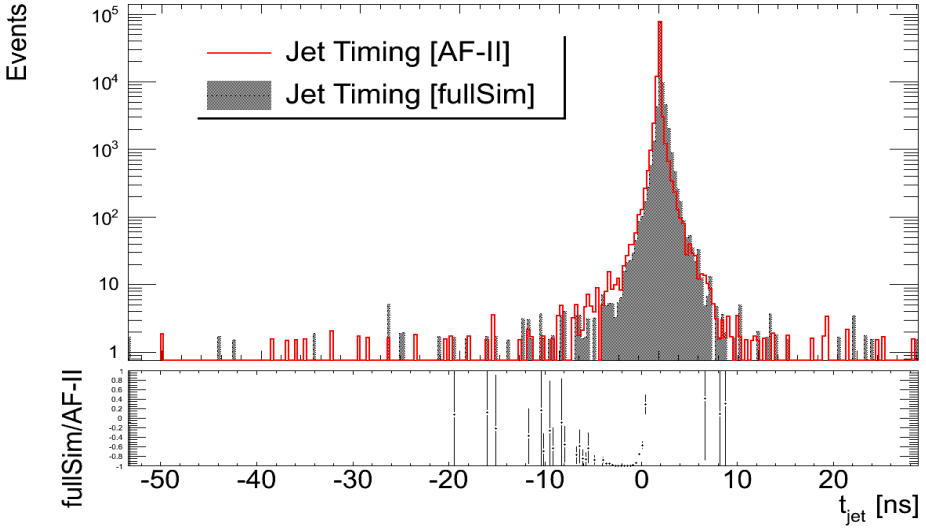

simulation shows for the same sample. However the t_{jet} the distributions do not have large differences between them to be considered.

- Electromagnetic fraction

  The Electromagnetic (EM) Fraction refers to the energy deposited in the electromagnetic calorimeter divided by the total jet energy ([37]). Keeping in mind that the calorimeter simulation is a part where the fast simulation differs from the full simulation of the detector (Chapter 5), it happens to be an interesting variable to compare the agreement between AF-II and fullSim. The EM Fraction is used to suppress fake jets, especially those from cosmic rays, then a good agreement between ATLFast-II and full Geant4 simulation results important.

FIGURE 6.37: Comparison of EM fraction AF-II distribution and fullSim distribution for emu100 mass point.

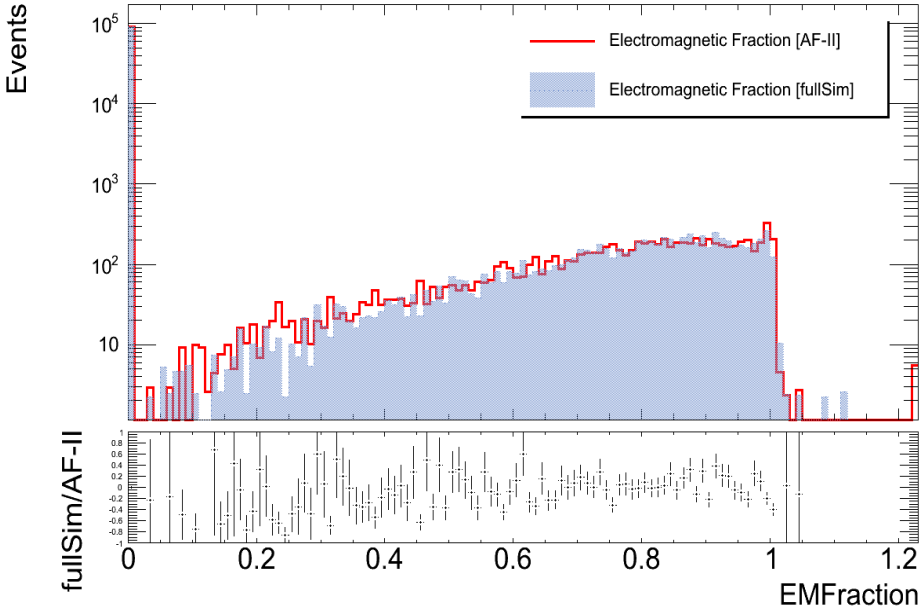

For the sneutrino 100 GeV mass point the ATLFast-II distribution shows a good agreement (6.37); jets in ATLFast-II are reconstructed using the same algorithms and software implementation as for full Geant4 simulation, so jets obtained from ATLFast-II are expected to have an energy response very similar to that of the full Geant4 simulation.

For the sneutrino 650 GeV mass point (6.38), the ATLFast-II distribution also shows similarities with full Geant4 simulation. Small discrepancies exist in the number of events around EMFraction = 0.2 (just as for emu100 sample, larger number of statistical population). However the ratio remains constant tending to zero, pointing to a similar behaviour for these distributions.

The distribution obtained for the sneutrino 2000 GeV of the EM fraction (6.39) shows agreement between ATLFast-II and full Geant4 simulation, where it is easily observed the good description done by ATLFast-II of this physics object.

FIGURE 6.38: Comparison of EM fraction AF-II distribution and fullSim distribution for emu650 mass point.

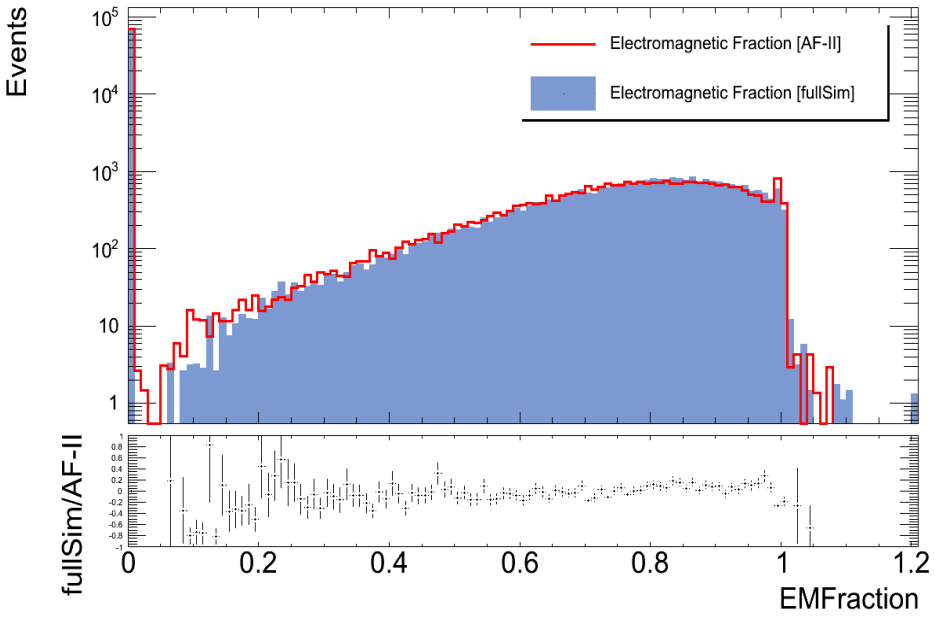

FIGURE 6.39: Comparison of EM fraction AF-II distribution and fullSim distribution for emu2000 mass point.

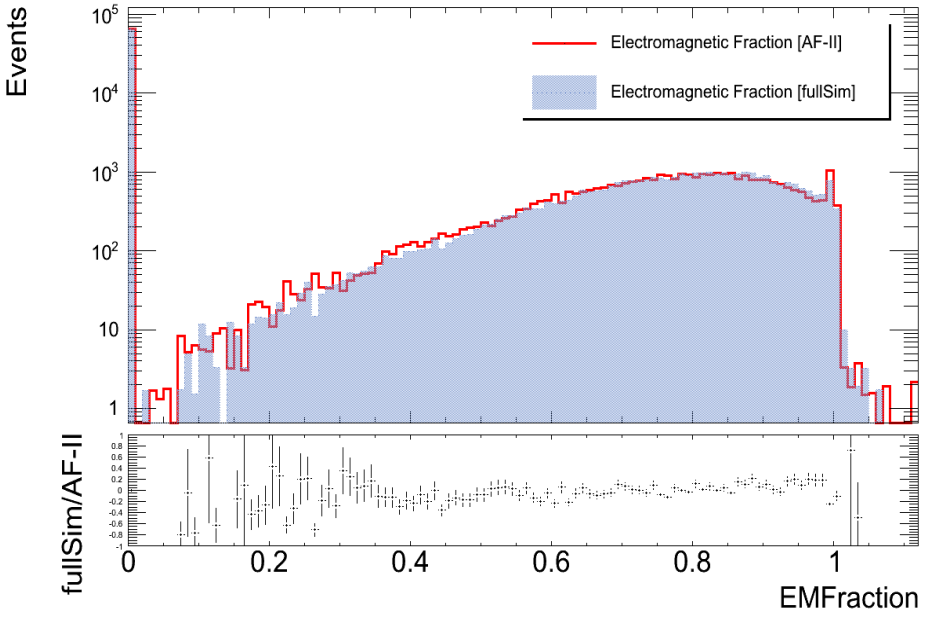

6.3.5 Performance for Missing Transverse Momentum

In a hadron collider the missing transverse momentum is defined as the momentum imbalance in the plane transverse to the beam axis (Chapter 4), where momentum conservation is expected [38]. Such an imbalance may signal the presence of undetectable particles, such as neutrinos or new stable, weakly-interacting particles.

The missing transverse momentum[12] is used to describe the magnitude of the vector momentum imbalance, E_T^{Miss}, and it is calculated from the energy deposit in all calorimeters cells and also from muons. However, in simulated events the ideal description of this quantity is given only by non-interacting particles involved and it is referred as the true E_T^{miss} ($E_T^{miss,true}$). A good description done by ATLFast-II is vital for its applicability to many studies of searches for new physics.

The further analysis will study the reconstructed E_T^{miss} distribution for each mass point.

- True Missing Transverse Momentum, $E_T^{miss,true}$

  The process studied was a sneutrino decaying into an electron-muon pair (according with the setup of the study given in Section 6.1), and there is no momentum imbalance in the hard process. It is expected then to have a small $E_T^{miss,true}$ distribution. A comparison between the E_T^{miss} reconstructed for each detector simulation and the true expected value E_T^{miss} was done for each mass point.

FIGURE 6.40: Validation of the reconstructed E_T^{Miss} with truth variables done for fullSim distribution with non-interacting particles for emu100 mass point.

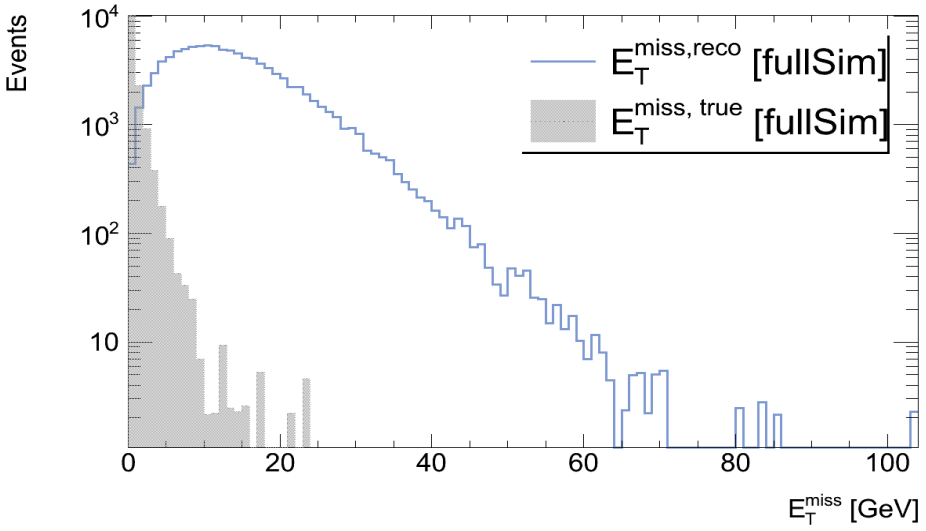

[12] Some times will be refered as "missing transverse energy" due to the laws of conservation of energy and momentum.

FIGURE 6.41: Validation of the reconstructed $E_T Miss$ with truth variables done for AF-II distribution with non-interacting particles for emu100 mass point.

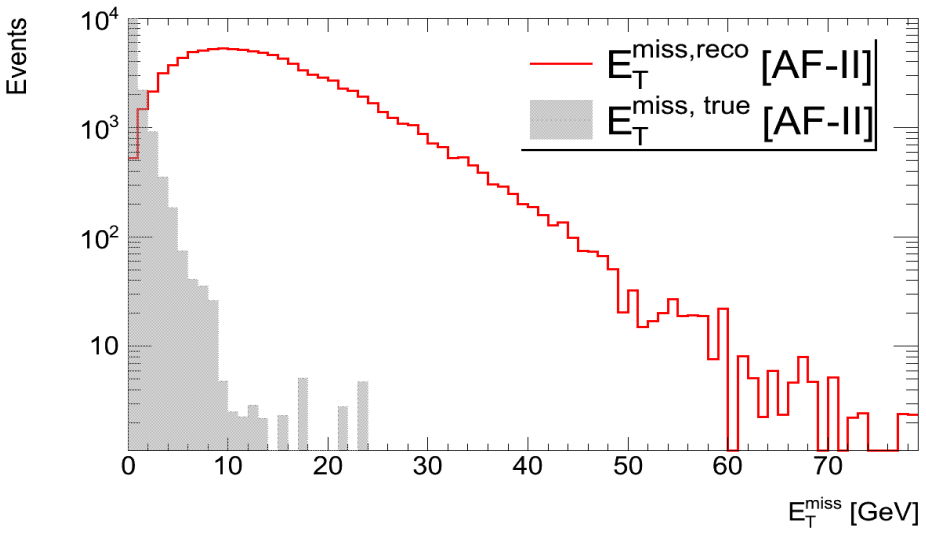

The missing transverse momentum reconstruction is based first on the calibrated calorimeter cell energies and on the reconstructed muons. The transverse energy reconstruction follows three steps: first the E_T^{miss} muon term is calculated from the momenta of the muons measured using the muon spectrometer reconstruction. Second, the E_T^{miss} reconstruction accounts for the cryostat term, which corrects for the energy lost between the LAr electromagnetic and tile calorimeter. And finally, a refined calibration is performed through the association of each high p_T object in the events to its calibrated cells [32].

Then, the missing transverse momentum reconstructed relies on a proper reconstruction of all other physics objects; for instance, if the muon has a large p_T the resolution will have effects on the missing transverse momentum. Therefore the differences observed between the true distribution and the reconstructed, and the broader distribution are understandable after the study of the muon p_T performance done previously, where for a 300 GeV muon p_T the resolution is around 7% (Figure 6.21 shows the equivalence between muon p_T and the resolution). As it was explained in the muon p_T performance and its resolution before, it is expected that the muon resolution will increase with the muon p_T (for values larger than $\sim$ 30 GeV).

A deeper study will be necessary to understand the behaviour of the missing transverse momentum reconstructed and truth distribution, to verify if the reconstructed missing transverse momentum comes from lepton resolution. And also, it would be interesting to do a comparison between the missing transverse momentum muon term, the reconstructed total transverse energy and the truth distribution.

- Missing Transverse Momentum ATLFast-II/Full Geant4 Simulation

  The missing transverse momentum distribution for the electron-muon 100 GeV sample (6.42) shows a good agreement between the ATLFast-II and full Geant4 simulation, even the events in the tail show similarities although some disagreement after 80 GeV.

FIGURE 6.42: Comparison between the AF-II E_T^{Miss} distribution and fullSim E_T^{Miss} reconstructed distribution for emu100 mass point.

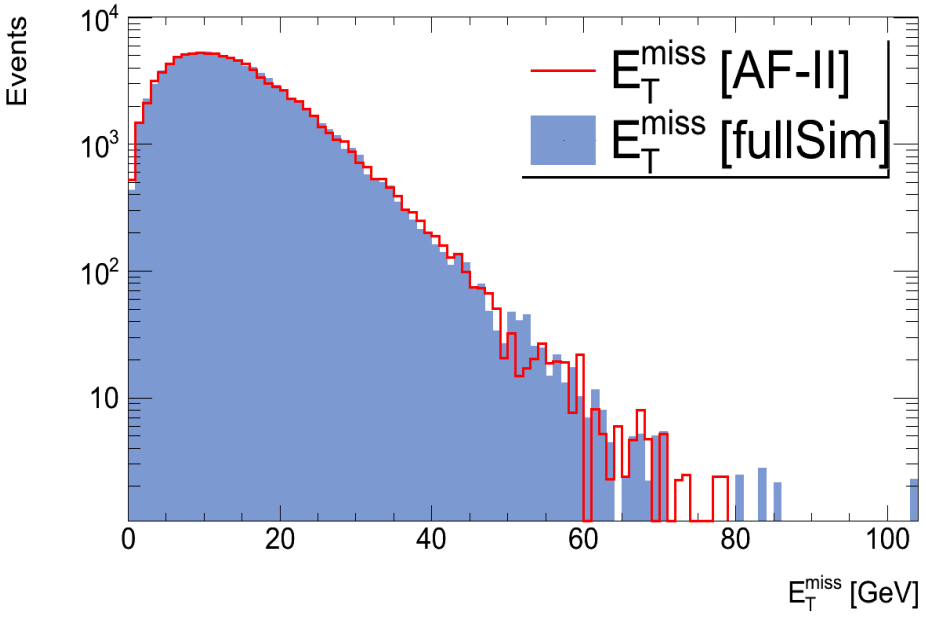

  The agreement for the electron-muon 650 GeV sample between the object distribution for ATLFast-II and full Geant4 simulation (6.43) is good and it includes most of the events in the tail; but some extra points in the missing transverse momentum were generated by ATLFast-II around (and after) 300 GeV, which are missing for full Geant4 simulation.

  On the other hand, a comparison of these results with the $E_T Miss$ obtained in the previous study done about the RPV SUSY model for a electron-muon resonance (Figure B.15 from [5]), shows certain agreement in the mean value of the distribution for electron-muon 650 GeV sample. But the distribution 6.43 seems to be broader than B.15.

  Again, a deeper study will be necessary for the missing transverse momentum distributions, due to the noise in the tails showing events with certain values of GeV far from the central tendency.

- Components of the Missing Transverse Momentum

  The missing transverse momentum, E_T^{Miss}, has two components: the X component, $E_T x^{Miss}$, and the Y component, $E_T y^{Miss}$, because the definition of the transverse

FIGURE 6.43: Comparison between the AF-II E_T^{Miss} distribution and fullSim E_T^{Miss} reconstructed distribution for emu650 mass point.

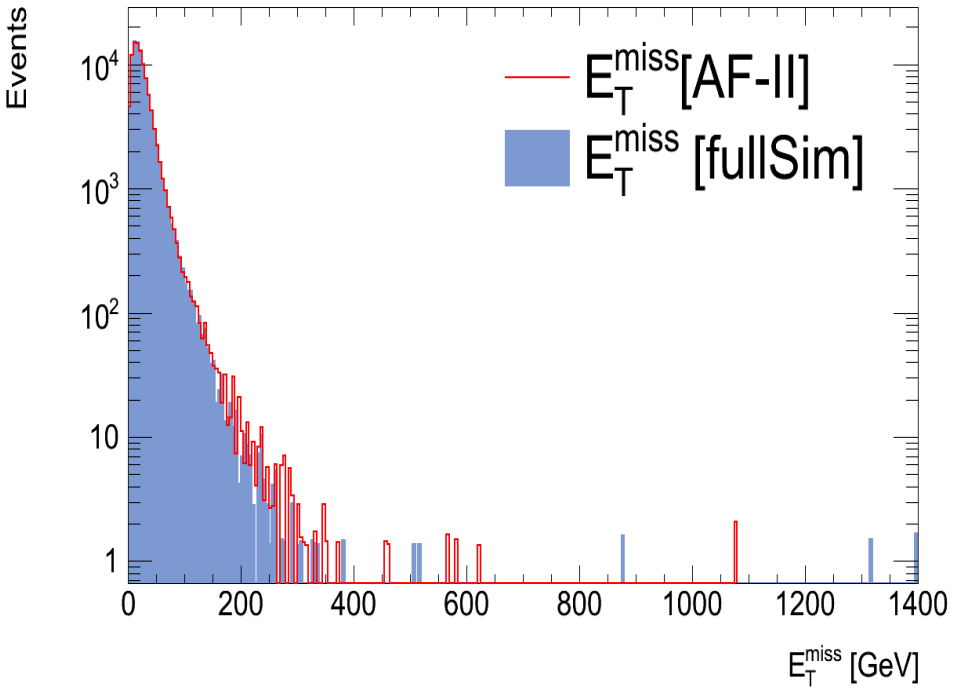

direction in the detector (Chapter 5). So, for each component it was done a comparison between ATLFast-II and full Geant4 simulation.

FIGURE 6.44: Comparison between the AF-II $E_T x^{Miss}$ distribution and fullSim $E_T x^{Miss}$ reconstructed distribution for emu100 mass point.

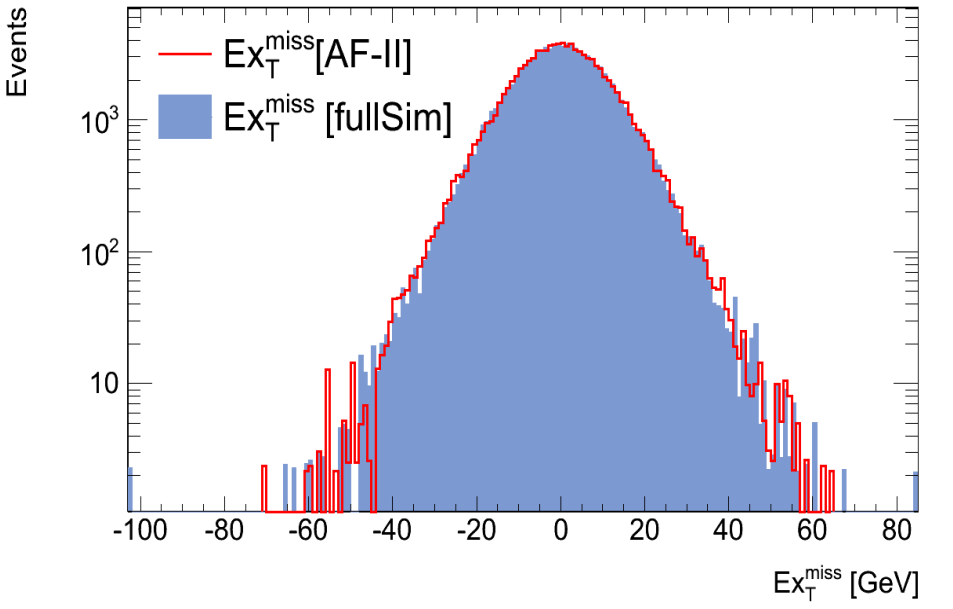

A good agreement is observed for electron-muon 100 GeV sample for the $E_T x^{miss}$

FIGURE 6.45: Comparison between the AF-II $E_T y^{Miss}$ distribution and fullSim $E_T y^{Miss}$ reconstructed distribution for emu100 mass point.

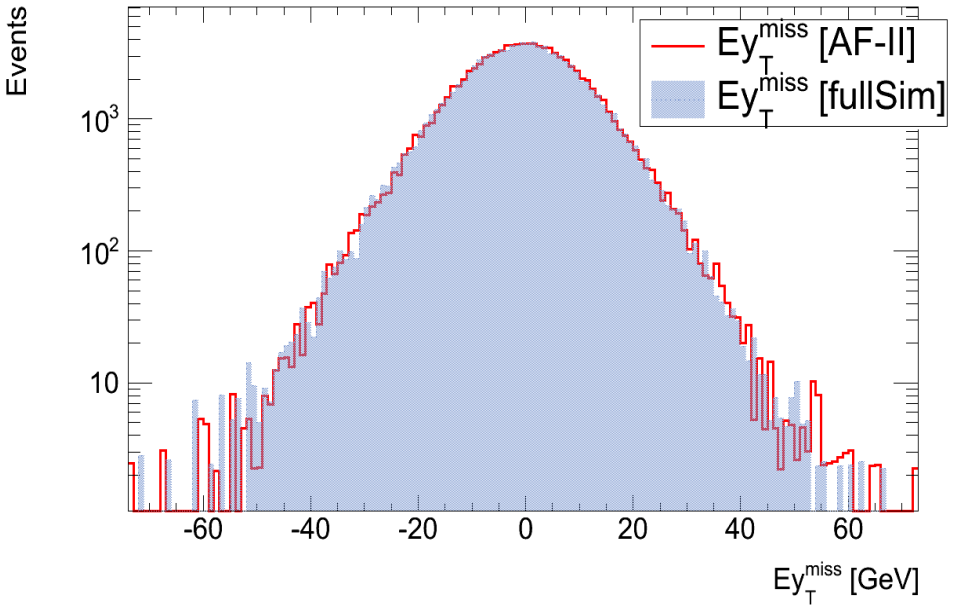

distribution (6.44), even though a few extra events were generated by ATLFast-II in the tails of the distribution, but in general the ATLFast-II $E_t x^{miss}$ distribution shows concordance in the central tendency described by full Geant4 simulation.

The similarities between the ATLFast-II $E_T y^{miss}$ distribution and the full Geant4 simulation $E_T y^{miss}$ distribution are large when comparing the description of the object (6.45); moreover, despite the behaviour one would expect in the tails of the distributions, they show a great resemblance.

For electron-muon 650 GeV sample the reconstruction of the E_T^{miss} in the X component generated by ATLFast-II simulation shows great similarities with the one generated by full Geant4 simulation (6.46), and yet only a few extra statistics reconstructed by ATLFast-II differ from the full Geant4 simulation. As usual, those small discrepancies are located in the tail of the distribution, but it do not represent a significant noise.

The $E_T y^{miss}$ distribution described by ATLFast-II for electron-muon 650 GeV sample shows once more a good agreement with full Geant4 simulation distribution (6.47), despite the few extra points generated out of the central tendency of the distribution.

FIGURE 6.46: Comparison between the AF-II $E_T xMiss$ distribution and fullSim $E_T xMiss$ reconstructed distribution for emu650 mass point.

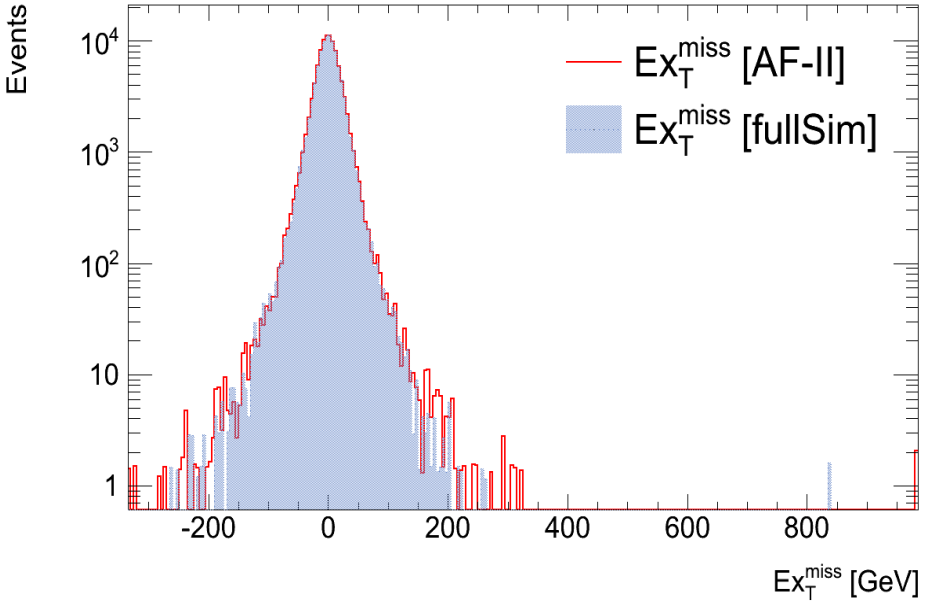

FIGURE 6.47: Comparison between the AF-II $E_T yMiss$ distribution and fullSim $E_T yMiss$ reconstructed distribution for emu650 mass point.

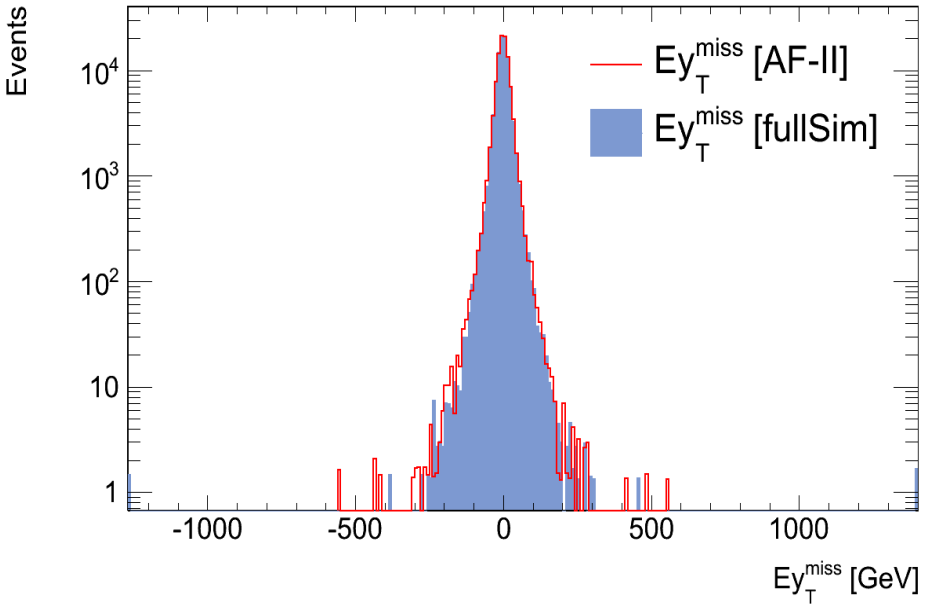

6.4 Tau Sneutrino: Study of the Invariant Mass

Throughout this study, it has been explained different physics objects linked with certain RPV SUSY process: an electron-muon resonance. For the physics analysis of this resonance one of the most important objects to study, and to have a good description either by data taken at the detector or simulated by any of the strategies explained before, is the invariant mass. The invariant mass is often used as a discriminator on SUSY analysis, and more specifically for SUSY dilepton analysis.

The main idea behind this process is to look for some heavy particle signal through a final signature of an electron-muon pair with opposite charge, which could suggest new physics signals.

The electron-muon final state is characterised by a clean detector signature, and low backgrounds which includes Standard Model processes that are mainly due to the production of $Z/\gamma* \rightarrow \tau\tau$, WW, WZ, ZZ, $t\bar{t}$ and single top quarks (Wt). These background processes are often small and characterised by invariant mass spectra that lie well bellow the range of new physics.

Among the possible new physics signals, RPV SUSY model predicts an electron-muon signature in the final state as a consequence of a tau sneutrino decaying. Then for the invariant mass, $m_{(e,\mu)}$, a comparison between the Standard Model data and prediction with center-of-mass energy $\sqrt{S} = 7$ TeV and luminosity of 1.07 fb^{-1} of proton-proton collision data taken by the ATLAS detector, sneutrino simulation and a heavy neutral gauge boson Z' was done by ATLAS Experiment [5], and it is shown in Figure 6.48.

The current study only simulated the sneutrino masses, using ∼4 times more data but with the same $\sqrt{S}$.

6.4.1 ATLFast-II Performance

The previous studies of the heavy particle signal decaying into an electron-muon pair, did the simulation and reconstruction of the signal samples with the full Geant4 simulation. But, in order to produce larger statistics in least time it is important to have a good agreement for ATLFast-II. Then, before doing any analysis of physics beyond the sneutrino signals it is important to do a comparison between both simulations for the invariant mass.

The comparison done for sneutrino 100 GeV, 6.49, has a good agreement between the ATLFast-II and full Geant4 simulation where the distribution ratio goes to zero nearly all range.

FIGURE 6.48: Previous study about the electron-muon decay, "observed and predicted electron-muon invariant mass distributions. Signal simulations are shown for m_{snutau} = 650 GeV and $m_{Z'}$ = 700 GeV. The couplings $\lambda'_{311} = 0.10$ and $\lambda_{312} = 0.05$ are used for the RPV snutau model. The production cross section is assumed to be the current published limit of 0.178 pb for the LFV Z' model. The ratio plot at the bottom includes only statistical uncertainties", [39]. ATLAS Experiment © 2012 CERN.

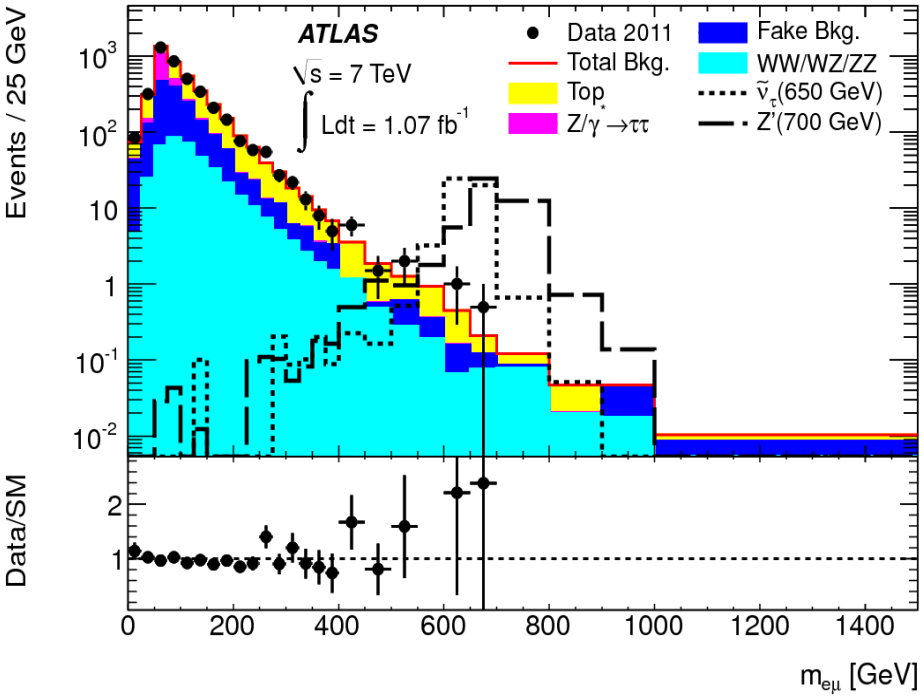

FIGURE 6.49: Comparison of AF-II $m_{e,mu}$ distribution and fullSim $m_{e,mu}$ distribution for emu100 mass point.

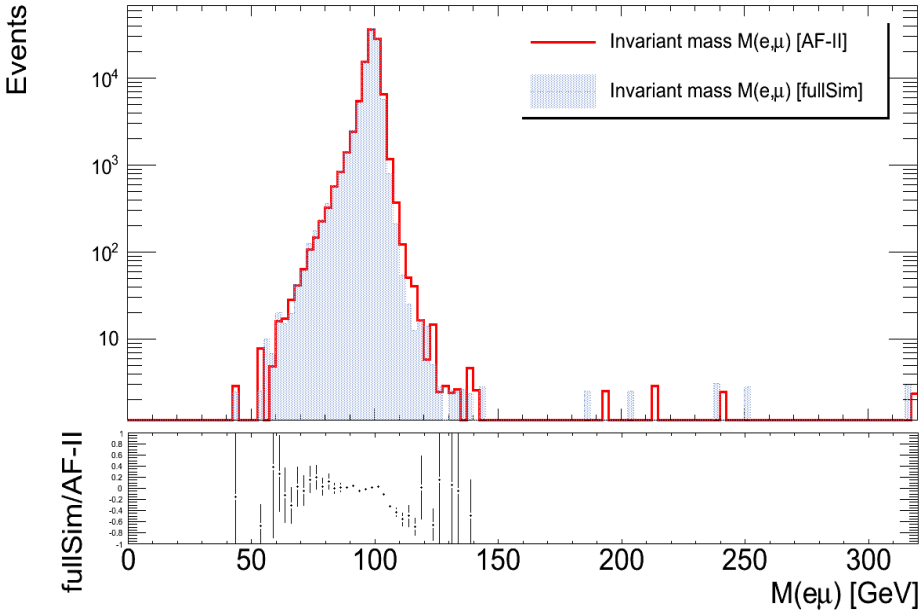

FIGURE 6.50: Comparison of AF-II $m_{e,mu}$ and fullSim $m_{e,mu}$ distribution for emu650 mass point.

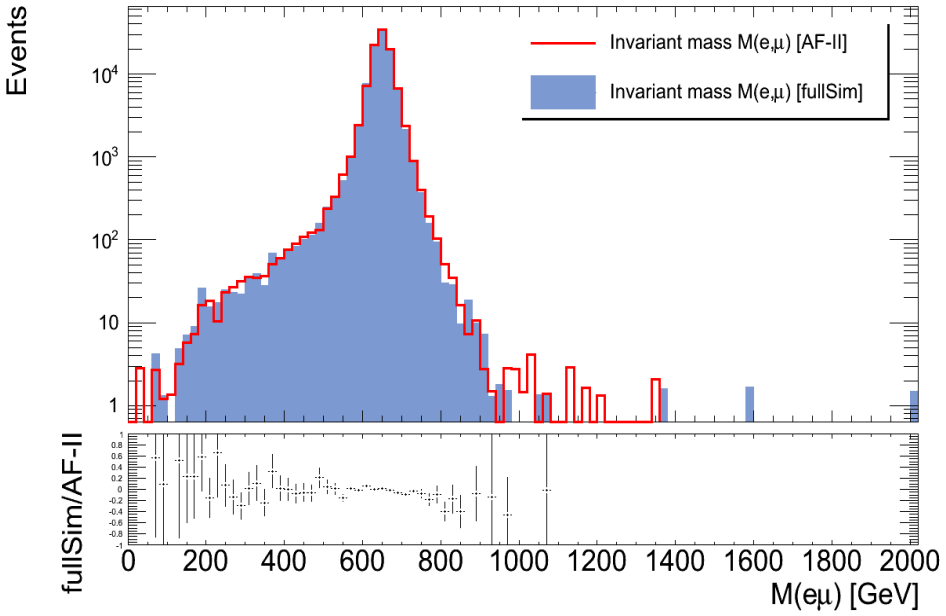

The invariant mass distribution for sneutrino 650 GeV mass point shows agreement between ATLFast-II and full Geant4 simulation. Some discrepancies between the points at the tail are clear (around 1 TeV), where extra events were generated by AF-II. In spite of those differences, the central tendency has ratio approaching to zero.

FIGURE 6.51: Comparison of AF-II $m_{e,mu}$ distribution and fullSim $m_{e,mu}$ distribution for emu2000 mass point.

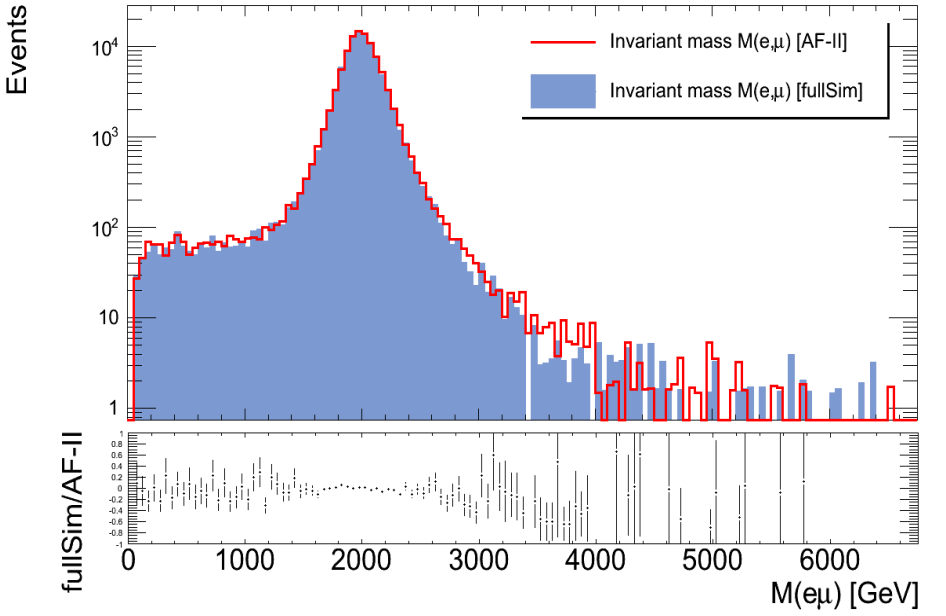

The same behaviour is observed for the sneutrino 2000 GeV mass point, where the

ATLFast-II and full Geant4 distributions show a good agreement nearly all over the range.

Therefore, ATLFast-II simulation does a good reconstruction of the invariant mass and it could be used to simulate the data for SUSY dilepton analysis.

6.5 Event Selection Efficiency

The Monte Carlo signal samples were made to simulate a sneutrino decaying process, but in order to match the signature of the process a set of cuts have been designed and applied to the samples. This goes from the total number of events to the number of events with a final signature with one signal electron, one signal muon with opposite sign, the number of vertex required and so on.

The preselected cuts are:

1. **GRL**, good run list: from all the events simulated, only those which are considered valid under certain criteria (trigger selection, run range) determine the good run list.
2. **Jet LAr Hole**: a "hole" in the LAr calorimeter[13] affects the jet and missing transverse momentum reconstruction, then it is necessary to clean the events which have a jet in the LAr hole area.
3. **Bad jets**: bad jets are jets not associated to real energy deposits in the calorimeters. They could be generated by different sources: from hardware problems to cosmic-ray showers.
4. **Primary vertex**: only those events with the number of vertex required in the object definition (> 3 vertex).
5. **Bad muons**: veto any event where a "baseline" muon before overlap removal is found.
6. **Cosmic muons**: cosmic muons rejected.
7. **Trigger**: the trigger match.
8. **2 leptons**: two leptons are required, one electron and one muon.

[13]The LAr hole is the commonly used term within the ATLAS collaboration for a detector problem which has occurred in the first half of 2011 data taking and which affects part of the electromagnetic liquid-argon calorimeter in the barrel.

9. **Signal leptons**: those leptons which passed the previous cut must fulfil the object definition given for the signal leptons.

10. **Opposite sign**: those leptons which passed the previous cut, and they have opposite signs.

emu100						
	Event number AF-II		**Event number fullSim**		ε % **AF-II**	ε % **fullSim**
	Total	Normalised to Luminosity	Total	Normalised to Luminosity		
Nominal	100000	54192.9 ± 171.4	100000	54148.2 ± 171.5	-	-
GRL	100000	54192.9 ± 171.4	100000	54148.2 ± 171.5	-	-
JetLArHole	99966	54171.4 ± 171.4	99965	54126.5 ± 171.5	0.9997	0.9996
BadJets	99918	54144.7 ± 171.3	99916	54099.9 ± 171.4	0.9992	0.9992
Primary Vertex	95845	51931.1 ± 167.8	95929	51939.9 ± 168.0	0.9585	0.9593
Bad Muons	95844	51930.4 ± 167.8	95929	51939.9 ± 168.0	0.9584	0.9593
Cosmic Muons	95284	51626.4 ± 167.3	95330	51616.6 ± 167.4	0.9528	0.9533
Trigger	74406	40554.7 ± 148.3	74569	40626.4 ± 148.5	0.7441	0.7457
2 Leptons	43703	23851.3 ± 113.7	43619	23786.9 ± 113.7	0.4370	0.4362
Signal Leptons	40139	21926.8 ± 109.0	41000	22374.1 ± 110.2	0.4014	0.4100
Opposite Sign	39571	21617.0 ± 108.2	40382	22035.2 ± 109.4	0.3957	0.4038

TABLE 6.5: Event cutflows sneutrino 100 GeV mass point.

emu650						
	Event number AF-II		**Event number fullSim**		ε % **AF-II**	ε % **fullSim**
	Total	Normalised to Luminosity	Total	Normalised to Luminosity		
Nominal	100000	49480.6 ± 156.5	100000	49440.2 ± 156.6	-	-
GRL	100000	49480.6 ± 156.5	100000	49440.2 ± 156.6	-	-
JetLArHole	99508	49215.1 ± 156.1	99486	49161.5 ± 156.1	0.99508	0.99486
BadJets	99125	49026.4 ± 155.8	99126	48981.8 ± 155.9	0.99125	0.99126
Primary Vertex	97078	48016.0 ± 154.2	96976	47924.5 ± 154.2	0.97078	0.96977
Bad Muons	96988	47971.4 ± 154.1	96882	47878.2 ± 154.1	0.96988	0.96883
Cosmic Muons	96765	47862.1 ± 153.9	96686	47780.7 ± 153.9	0.96765	0.96687
Trigger	92792	46142.6 ± 151.1	92739	46084.6 ± 151.2	0.92792	0.92740
2 Leptons	72381	35991.3 ± 133.5	72256	35898.3 ± 133.4	0.72381	0.72257
Signal Leptons	69439	34540.2 ± 130.7	69766	34672.2 ± 131.1	0.69439	0.69766
Opposite Sign	68269	33954.2 ± 129.6	68572	34073.9 ± 130.0	0.68269	0.68573

TABLE 6.6: Event cutflows sneutrino 650 GeV mass point.

In order to estimate the effect of ATLFast-II simulation in this analysis, tables 6.5, 6.6 and 6.7 show the efficiency of the cut applied on the samples for each simulation. Initially, the total number of events for each simulation are the same (full Geant4 simulation samples were normalised to their respective ATLFast-II samples as it was stated previously); but in order to have a meaningful number of events, it is necessary to normalise to the luminosity and to apply all the event weights to compensate the simulation values and match the conditions with real data and therefore have an approximation of what would be expected to get in real data. Then the efficiency was done with respect the initial number of events for ATLFast-II and full Geant4 simulation.

emu2000						
	Event number AF-II		**Event number fullSim**		ε % **AF-II**	ε % **fullSim**
	Total	Normalised to Luminosity	Total	Normalised to Luminosity		
Nominal	100000	49480.6 ± 156.5	100000	49440.8 ± 156.6	-	-
GRL	100000	49480.6 ± 156.5	100000	49440.8 ± 156.6	-	-
JetLArHole	99134	49035.5 ± 155.8	99126	48990.9 ± 155.9	0.99134	0.99126
BadJets	98225	48583.6 ± 155.1	98220	48540.1 *pm* 155.1	0.98225	0.98220
Primary Vertex	96386	47671.3 ± 153.6	96372	47624.9 ± 153.7	0.96386	0.96372
Bad Muons	92733	45865.7 ± 150.7	92683	45800.0 ± 150.7	0.92733	0.92683
Cosmic Muons	92638	45819.7 ± 150.6	92586	45751.9 ± 150.6	0.92638	0.92586
Trigger	89177	44289.5 ± 148.0	89288	44302.8 ± 148.2	0.89177	0.89288
2 Leptons	62257	30889.4 ± 123.6	62604	31042.0 ± 124.1	0.62257	0.62604
Signal Leptons	60039	29796.3 ± 121.4	60693	30099.6 ± 122.2	0.60039	0.60693
Opposite Sign	57580	28572.9 ± 118.9	58216	28868.4 ± 119.7	0.57580	0.58216

TABLE 6.7: Event cutflows sneutrino 2000 mass point.

For the sneutrino 100 GeV mass point, the difference between the number of events for the desired signature (an electron - a muon with opposite sign) is only of 2%; while for the sneutrino 650 GeV mass point the difference is 0.44 % between ATLFast-II and full Geant4 simulation and the sneutrino 2000 GeV mass point shows a difference of 1.1% between both simulations. Therefore, not even 5% of difference was found for the ATLFast-II simulation of the samples when compared with full Geant4 simulation. Therefore, a good agreement between ATLFast-II and full Geant4 simulation was observed.

Chapter 7

Conclusions

The aim of this work was to verify the performance of ATLFast-II simulation as a tool to describe different physics objects with same accuracy as a full Geant4 simulation of the detector but with less time consumption. To investigate this performance it was used a particular RPV SUSY model predicting the existence of a heavy neutral short-lived resonance.

There are many reasons why a RPV SUSY model was chosen to do this validation: firstly, the clean signature of the process predicted by the model. Secondly, the difference using ATLFast-II for this RPV SUSY model, compared to RPC SUSY models, is the absence of large missing transverse momentum which might increase effects from the tails of the distributions, and this is important because ATLFast-II encounters difficulties describing properly the tails of the distributions; and thirdly the strong constraints put on RPC scenarios by ATLAS and CMS experiments and therefore the increasing interest over RPV SUSY models.

In a direct comparison of ATLFast-II simulation with a full Geant4 simulation of the detector, the performance of ATLFast-II for describing physical distributions showed good agreement over nearly all the objects distributions for all the samples used. But a "good agreement" should be understood as a description of the physics objects where the key features of their properties are well reproduced, and differences in details due to the simplification in the model need to be accepted, as long as the differences do not lead to large and unpredictable results at the physics analysis; therefore, over all the results showed in this work it is possible to say that ATLFast-II reproduces with high accuracy all the kinematic distributions studied, and its simulation is justified for this study. Based on these results, recommendations to identify possible weaknesses and to correct any potential failures in ATLFast-II simulation tool are made later in this chapter.

A numerical evidence of ATLFast-II accuracy is given by the event selection, where the full Geant4 simulation and ATLFast-II simulation showed less than 5% of difference for the number of events; for instance, the electron-muon 2000 GeV sample differed in 1.1% for the event selection of the process signature studied throughout this work, a gain of 2.3 times for the end-user waiting time when ATLFast-II was used to simulate the sample, while the CPU-time gain was around 8 times for ATLFast-II.

The current study demonstrates an accurate description of the physics objects and a non-negligible time performance gain by ATLFast-II. Compared to previous ATLFast-II validations (for different SUSY models) the study shows an improvement in the fast simulation tool and it implies that some technical issues described by those prior validations (e.g. low priority given to ATLFast-II request) were solved.

Future work

Despite the results obtained in the current work, where ATLFast-II simulation turned out to be justied for this model, it is necessary to do a deeper study for some of the objects distributions because it is vital to have a good description of their performance for physics analysis; before a possible complete transition from full Geant4 simulation to ATLFast-II simulation it is necessary to eliminate possible sources of significant discrepancies that could affect the outcome of the physics analysis.

First, it is necessary to do a comparison of performances for energetic electrons ($> 500GeV$) to understand how is the performance of ATLFast-II for larger energies. Until the moment studies about the electron in the GeV range have been made, but it does not exist a performance validation for very-high p_T. Figure 6.6 and Figure 6.9 showed larger differences between ATLFast-II and full Geant4 simulation than in Figure 6.3 corresponding to electrons in the 100 GeV range. Therefore, it is necessary to understand how the accuracy is in this range and to confirm if they are reasonably described.

Second, for the muons performance it is necessary to do a deeper study about all the isolation cuts applied explicitly in the cuts or implicitly in the standard object selection, in order to understand the behaviour of the isolation and its relation with the muon kinematic objects performance.

Third, a study is needed about the trigger efficiency between ATLFast-II and full Geant4 simulation and if there is any significant difference or not.

Fourth, a better study should be performed of the missing transverse momentum and the origin of the anomalous events, with a deeper analysis about the differences between the true missing transverse momentum and the reconstructed. To do the last one it could be interesting to do a comparison between the performance of the missing transverse

momentum muon component with the total missing transverse momentum and to verify if the reconstructed missing transverse momentum comes from lepton resolution.

And last, a study of the background signal samples is necessary to validate completely the performance of ATLFast-II for RPV SUSY models.

Appendix A

Dataset list

The data sets used for the comparison between full Geant4 simulation and ATLFast-II simulation are listed below:

FAST Sim

mc11_7TeV.106486.RPV_emu100_jimmy_susy.merge.NTUP_SUSY.e1170_a131_s1353_a145_r2993_p832

mc11_7TeV.118508.RPV_emu650_jimmy_susy.merge.NTUP_SUSY.e1170_a131_s1353_a145_r2993_p832

mc11_7TeV.142557.RPV_emu2000_jimmy_susy.merge.NTUP_SUSY.e1170_a131_s1353_a145_r2993_p832

FULL Sim

mc11_7TeV.106486.RPV_emu100_jimmy_susy.merge.NTUP_SUSY.e1170_s1372_s1370_r3043_r2993_p832

mc11_7TeV.118508.RPV_emu650_jimmy_susy.merge.NTUP_SUSY.e1170_s1372_s1370_r3043_r2993_p832

mc11_7TeV.142557.RPV_emu2000_jimmy_susy.merge.NTUP_SUSY.e1170_s1372_s1370_r3043_r2993_p832

Appendix B

Auxiliary Plots

B.1 Auxiliary Plots ATLFast-II/Full Geant4 Simulation Comparison

- Electron Pseudorapidity

FIGURE B.1: Comparison of the electron pseudorapidity distribution for emu100 mass point

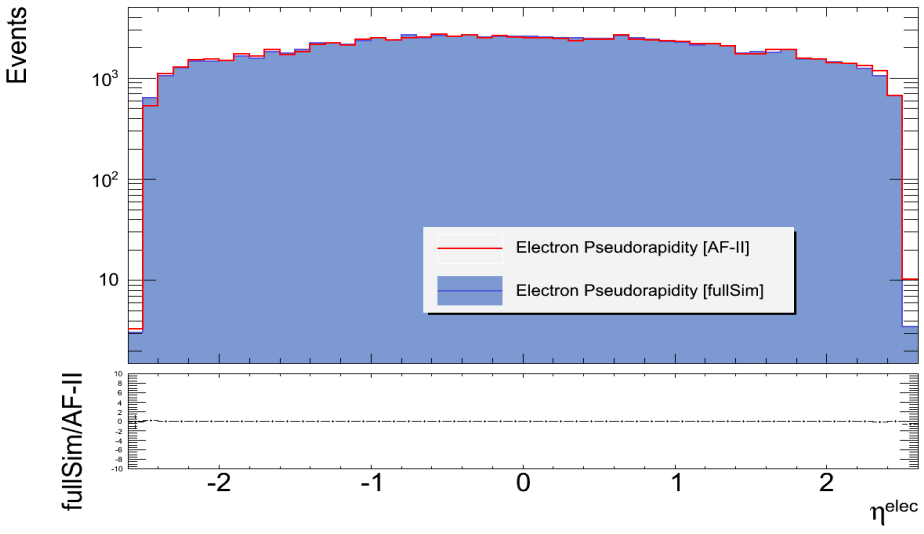

- Electron Azimuthal Angle

FIGURE B.2: Comparison of the electron pseudorapidity distribution for emu2000 mass point

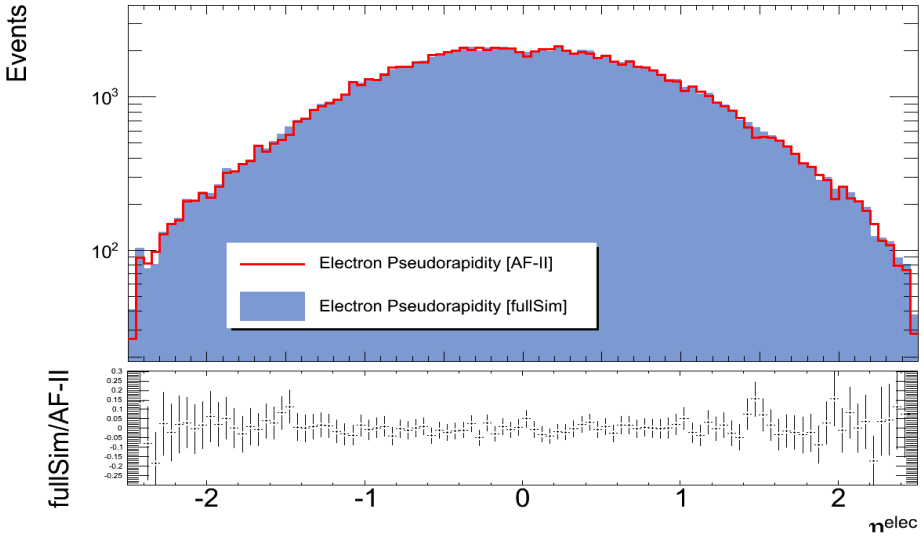

FIGURE B.3: Electron azimuthal angle distribution for emu100 mass point

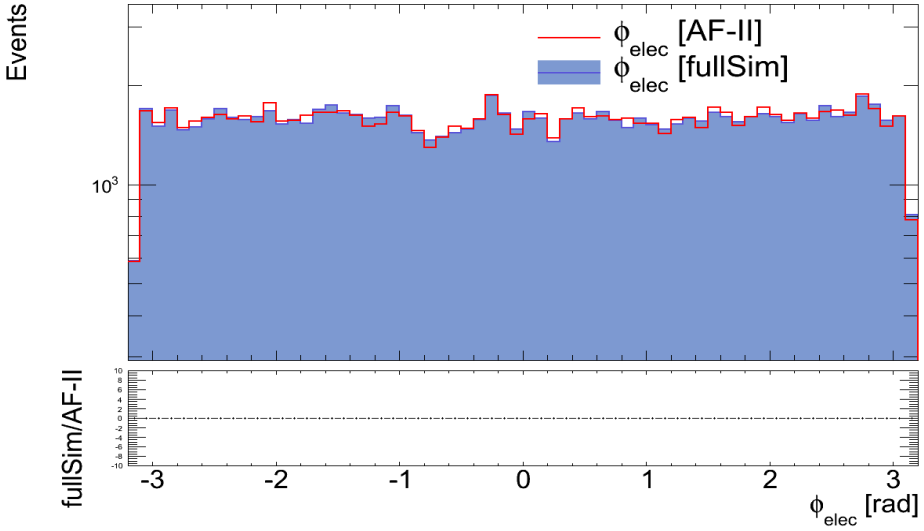

FIGURE B.4: Electron azimuthal angle distribution for emu2000 mass point

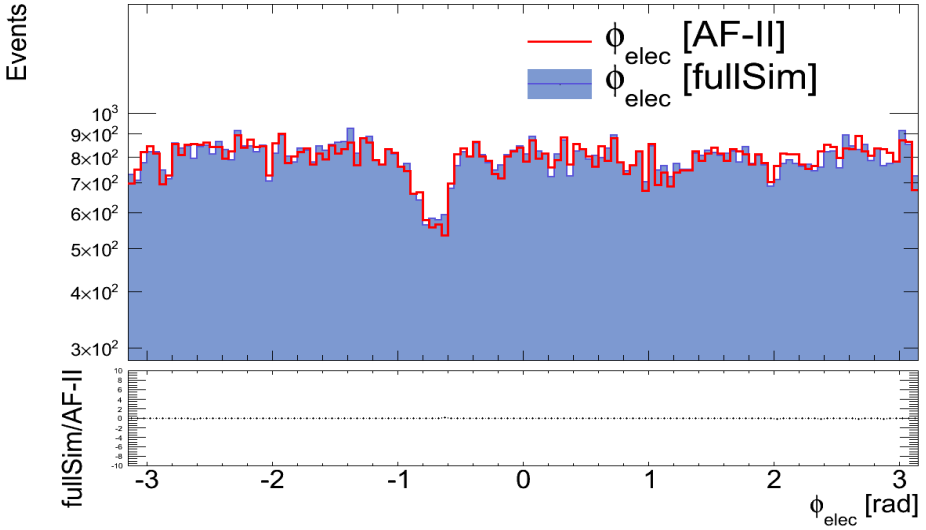

- Muon pseudorapidity

FIGURE B.5: Comparison of the muon pseudorapidity AF-II and fullSim distribution for emu100 mass point

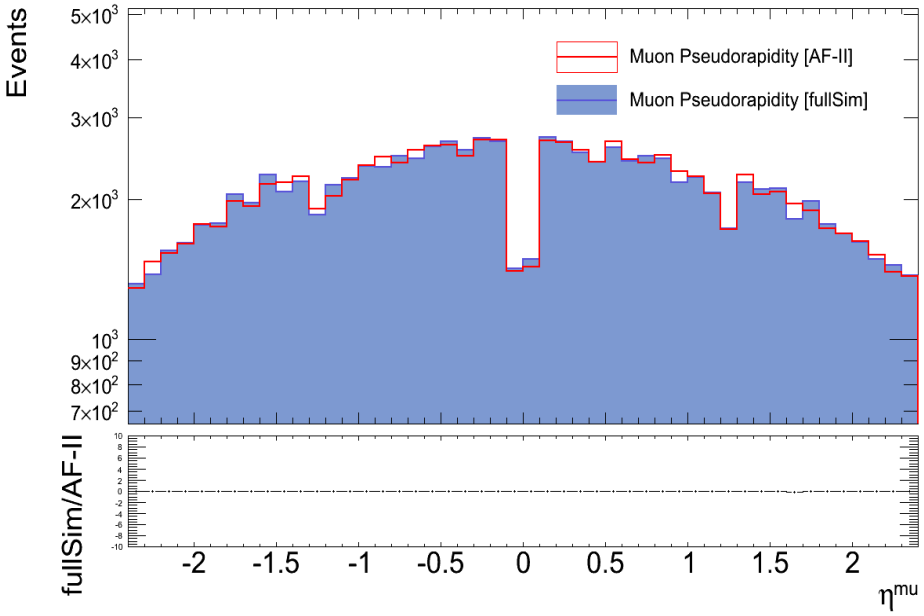

FIGURE B.6: Comparison of the muon pseudorapidity AF-II and fullSim distribution for emu2000 mass point

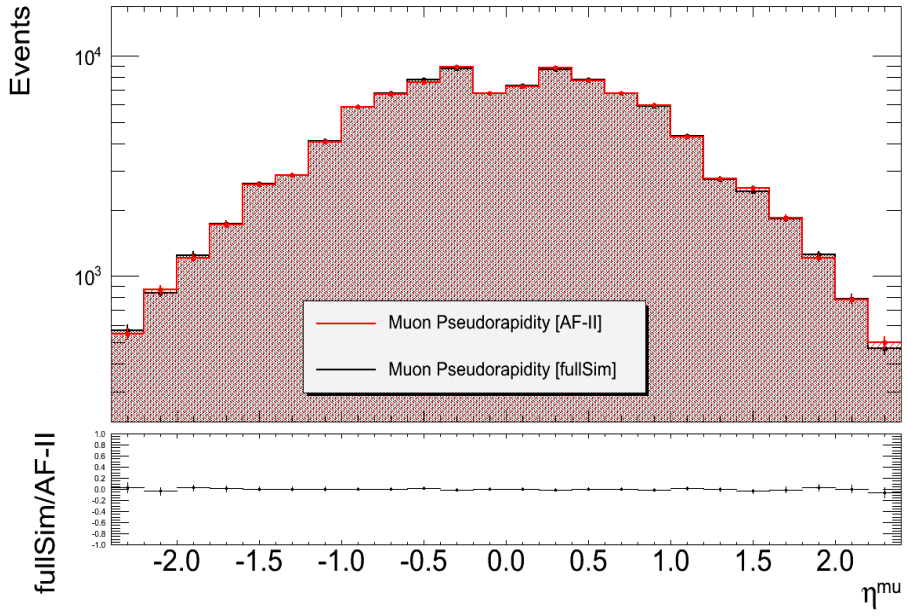

- Muon Azimuthal Angle

FIGURE B.7: Comparison of the muon ϕ AF-II and fullSim distribution for emu650 mass point

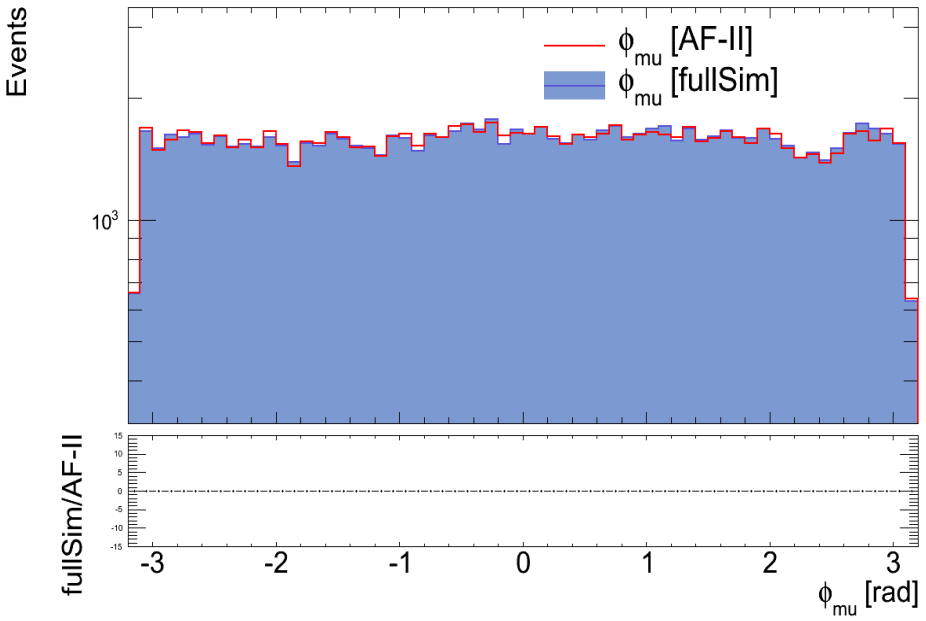

FIGURE B.8: Comparison of the muon ϕ AF-II and fullSim distribution for emu2000 mass point

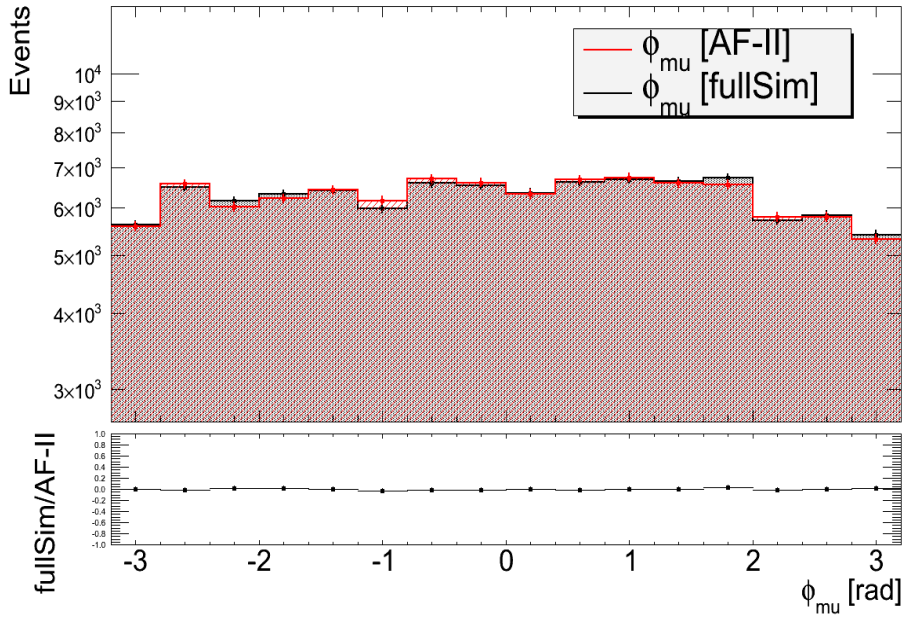

- Difference between the azimuthal angle of an electron and a muon

FIGURE B.9: Comparison of $\Delta\phi$ AF-II distribution and $\Delta\phi$ fullSim distribution for emu100 mass point

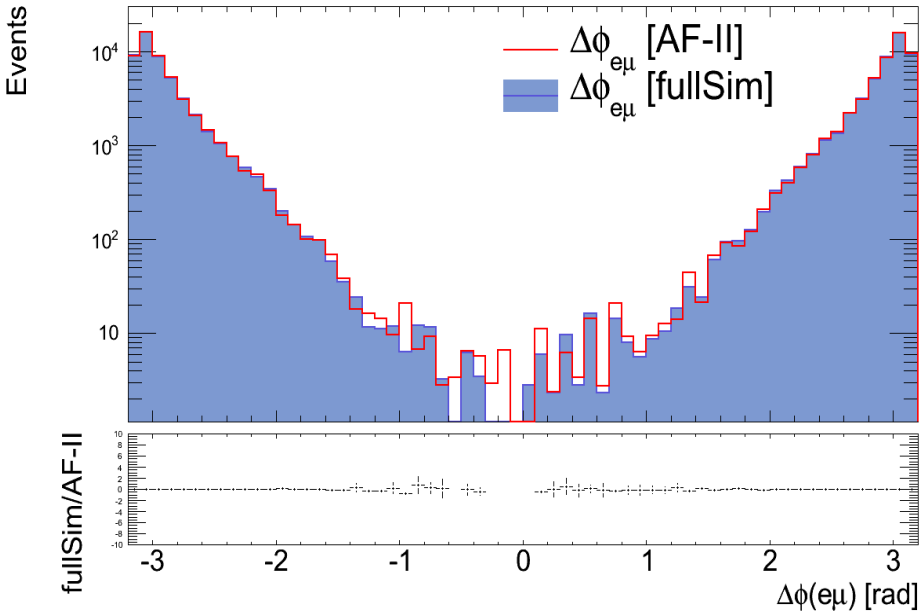

FIGURE B.10: Comparison of $\Delta\phi$ AF-II distribution and fullSim distribution for emu2000 mass point

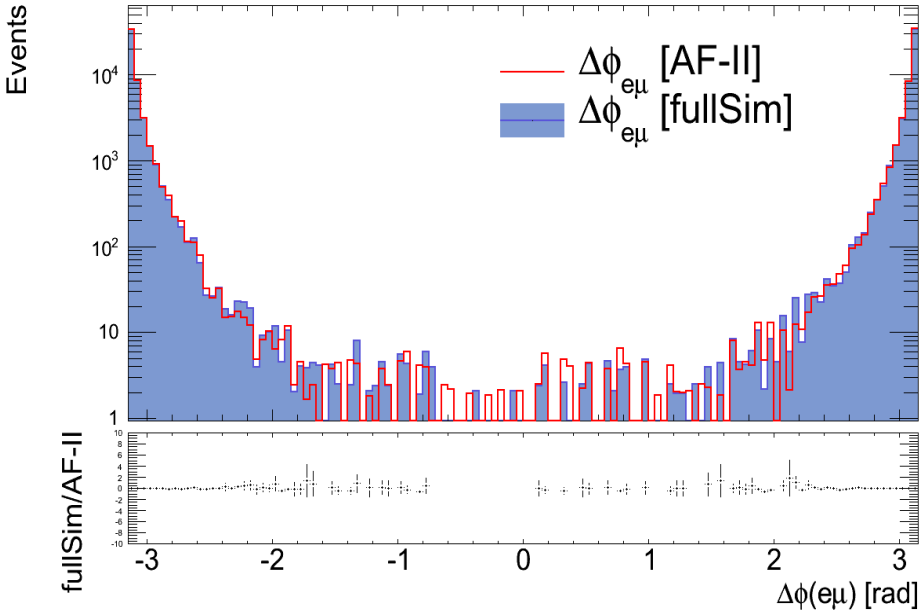

- True Missing Transverse Momentum, $E_T^{miss,true}$

FIGURE B.11: Validation of the reconstructed $E_T Miss$ with truth variables done for fullSim distribution with non-interacting particles for emu650 mass point

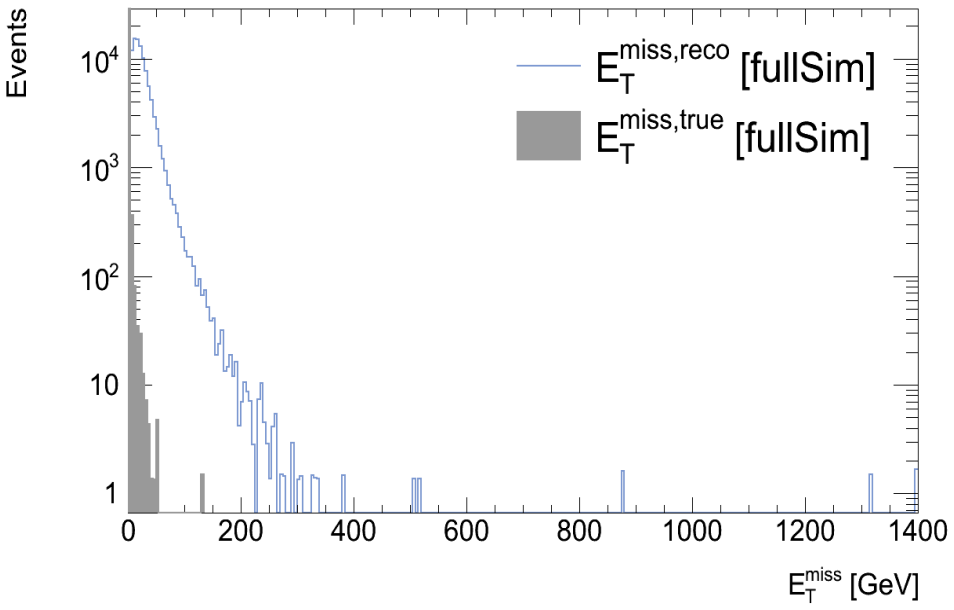

FIGURE B.12: Validation of the reconstructed $E_T Miss$ with truth variables done for AF-II distribution with non-interacting particles for emu650 mass point

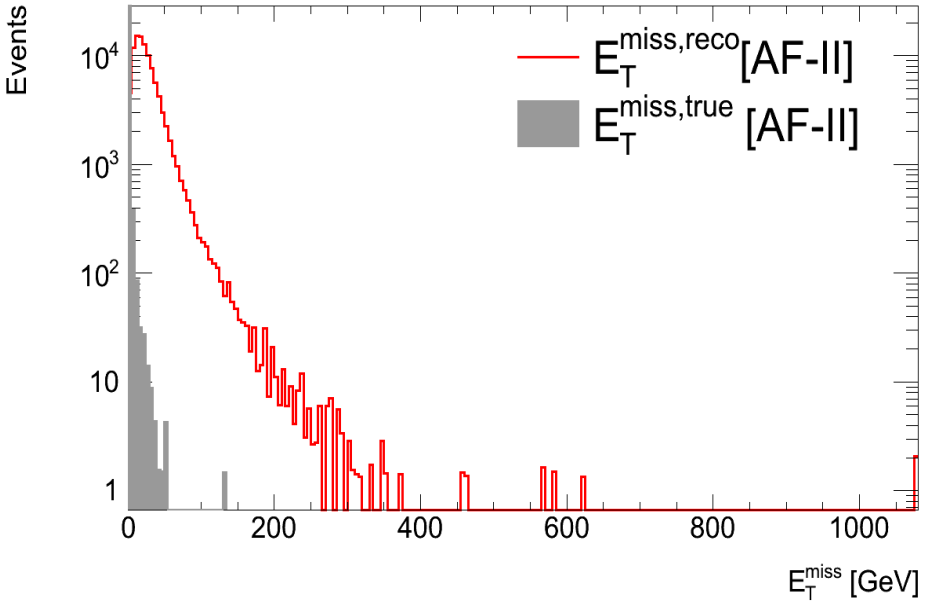

B.2 Auxiliary Plots Electron-Muon Resonance, ATLAS Results

The following plots are public results of the SUSY Group of ATLAS experiment, and the plots shown here are auxiliary plots from [5].

FIGURE B.13: "Observed and SM predicted electron p_T distributions. The signal simulation is shown for m_{snutau} = 650 GeV and $m_{Z'}$ = 700 GeV. The couplings $lambda'_{311}$ = 0.10 and $lambda_{312}$ = 0.05 are used for the RPV snutau model. The production cross section is assumed to be the current published limit of 0.178 pb for the LFV Z' model" [5], [39]. ATLAS Experiment © 2012 CERN.

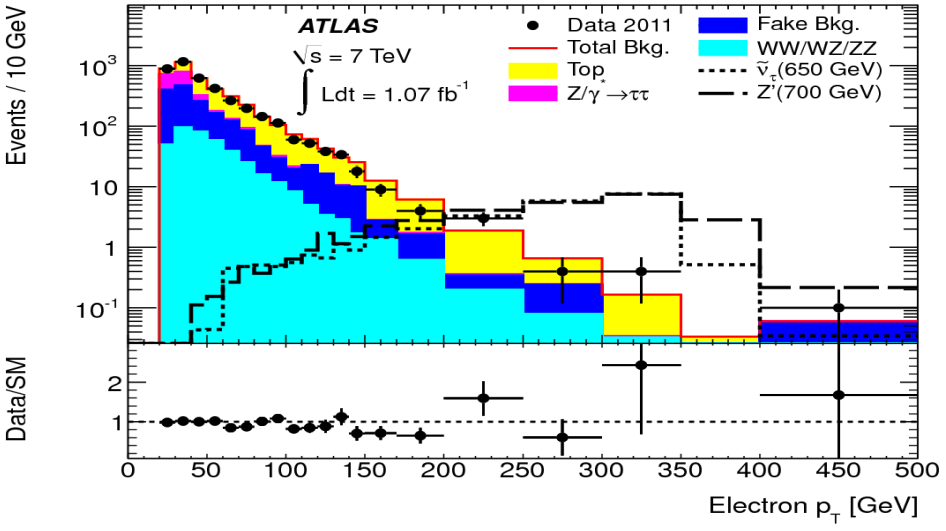

FIGURE B.14: "Observed and SM predicted muon p_T distributions. The signal simulation is shown for m_{snutau} = 650 GeV and $m_{Z'}$ = 700 GeV. The couplings $lambda'_{311}$ = 0.10 and $lambda_{312}$ = 0.05 are used for the RPV snutau model. The production cross section is assumed to be the current published limit of 0.178 pb for the LFV Z' model" [5], [39]. ATLAS Experiment © 2012 CERN.

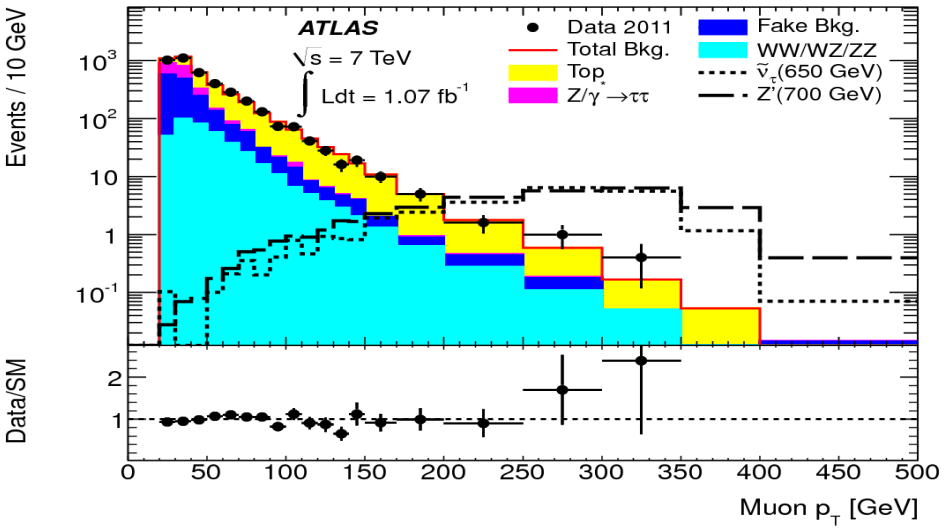

FIGURE B.15: "Observed and SM predicted MET distributions. The signal simulation is shown for m_{snutau} = 650 GeV and $m_{Z'}$= 700 GeV. The couplings $lambda'_{311} = 0.10$ and $lambda_{312} = 0.05$ are used for the RPV snutau model. The production cross section is assumed to be the current published limit of 0.178 pb for the LFV Z' model" [5], [39]. ATLAS Experiment © 2012 CERN.

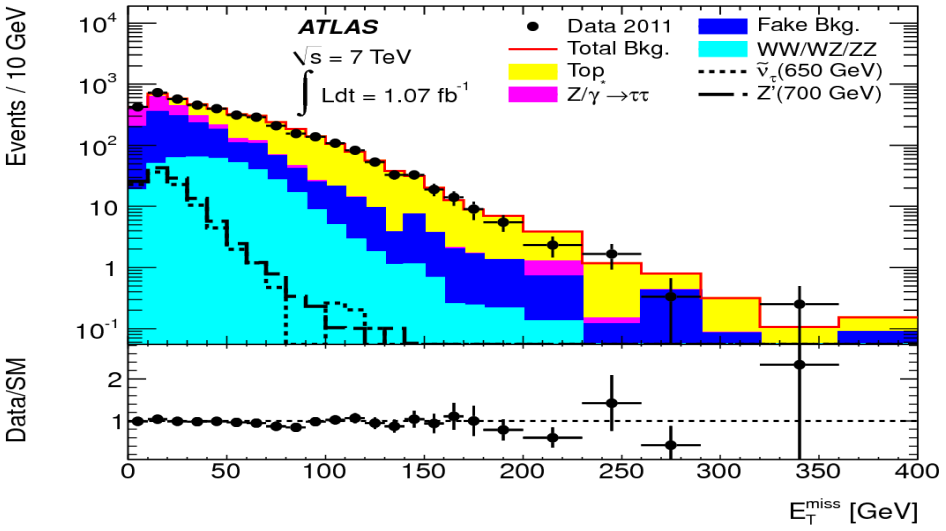

Appendix C

Object Definition Summary

These are the object definitions used during the analysis (summary of Chapter 6):

Electron :

- p_T > 25 GeV;
- Author: 1 || 3;
- Loose ID Electron: el_loose;
- $|\eta|$ <2.47;
- The electron isolation: Etcone40 < 10 GeV, where Etcone40 is defined as the transverse energy deposited in the calorimeter within a cone of radius $\Delta R = \sqrt{\Delta\eta^2 + \Delta\phi^2} = 0.4$ around the electron cluster, excluding the electron E_T.
- Signal Electron: Medium ID electron, el_medium.

Muon :

- Staco combined muon;
- Recommendations about the criteria for cuts to be done on the associated inner detector track, where the detector conditions and the failures in the Pixel detector are taken into account:
  - Require b-hits if expected.
  - Number of pixel hits + number of crossed dead pixel sensors > 1.
  - Number of SCT hits + number of crossed dead SCT sensors ≥ 6.
  - Number of pixel holes + number of SCT holes < 3.

  - For $|\eta| < 1.9$, require n > 5 and $n_{TRT}^{outliers} < 0.9$n; and for $|\eta| \geq 1.9$, require $n_{TRT}^{outliers} < 0.9$n if n > 5. Where, n $:= n_{TRT}^{outliers} + n_{TRT}^{hits}$ and $n_{TRT}^{outliers}$ denotes the number of TRT outliers on the muon track and n_{TRT}^{hits} denotes the number of TRT hits on the muon track.

- $p_T > 25$ GeV;
- $|\eta| < 2.4$.
- Isolated muon: ptcone40 < 10 GeV; where ptcone40 is the scalar sum of the p_T of tracks with $p_T > 1$ GeV within a cone of $\Delta R = 0.4$ around the muon track, excluding the muon p_T.

Jet :

- AntiKt4TopoNewEM jet;
- $p_T > 30$ GeV;
- $|\eta| < 2.5$.

Object Quality cleaning :

- Good electrons pass the following Object Quality flag: (el_OQ&1446)=0.

Overlap Removal :

Some objects tend to be identified as both electron and jets, or muon and jets for instance, so it is necessary to remove these overlaps:

- Remove jets in a cone of $\Delta R = 0.4$ around the selected electrons.
- Remove jets that overlapped in a cone of $\Delta R = 0.4$ with muons.

Primary vertex :

- At least 3 associated tracks.

E_T^{Miss} :

- MET_Simplified20_RefFinal.

Bibliography

[1] R. Barbier et al. R-parity violating supersymmetry. July 2005. URL http://arxiv.org/abs/hep-ph/0406039v2.

[2] Stephen Martin. A supersymmetry primer, September 2011. URL http://www.arxiv.org/abs/hep-ph/9709356v6.

[3] The ATLAS Collaboration. Search for a heavy neutral particle decaying into an electron and a muon using 1 fb^{-1} of atlas data, September 2011. URL https://atlas.web.cern.ch/Atlas/GROUPS/PHYSICS/PAPERS/SUSY-2011-11/. ATLAS Supersymmetry (SUSY) searches.

[4] E. Torro Pastor, D. Coté, and X. Portell Bueso. Validation of the atlfast-ii package for the simulation of supersymmetry events. ATLAS Internal Note, September 2011.

[5] The ATLAS Collaboration. Search for a heavy neutral particle decaying into an electron and a muon using 1 fb^{-1} of atlas data. *Eur.Phys.J.*, C(71):1809, September 2011. URL http://arxiv.org/abs/1109.3089v3.

[6] Gordon L. Kane. *Modern Elementary Particle Physics*. Westview Press, second edition edition, April 1993.

[7] The ATLAS Collaboration. Observation of a new particle in the search for the standard model higgs boson with the atlas detector at the lhc. July 2012. URL http://arxiv.org/abs/1207.7214.

[8] Sky Trillium French. *Searching for Supersymmetry with the ATLAS Detector at the Large Hadron Collider*. PhD thesis, University of Cambridge, May 2011.

[9] Herbi Dreiner. Hide and seek with supersymmetry, February 1999. URL http://arxiv.org/abs/hep-ph/9902347v1.

[10] The ATLAS Collaboration. Search for lepton flavour violation in the emu continuum with the atlas detector in $\sqrt{s}$= 7 tev pp collisions at the lhc. *Eur. Phys. J.*, C:19, May 2012. URL http://arxiv.org/abs/1205.0725.

[11] Marc Chemtob. Phenomenological constraints on broken r parity symmetry in supersymmetry models. *Prog. Part. Nucl. Phys.*, (54):91, June 2005. URL http://arxiv.org/abs/hep-ph/0406029.

[12] The ATLAS Collaboration. The atlas experiment photos, 2012. URL http://www.atlas.ch/photos/index.html.

[13] Lhc design report, 2004. URL https://ab-div.web.cern.ch/ab-div/Publications/LHC-DesignReport.html.

[14] Lhcb experiment, 2008. URL http://public.web.cern.ch/public/en/research/AccelComplex-en.html.

[15] Alice experiment, 2008. URL http://user.web.cern.ch/public/en/LHC/ALICE-en.html.

[16] Atlas experiment, 2008. URL http://user.web.cern.ch/public/en/LHC/ATLAS-en.html.

[17] Cms experiment, 2008. URL http://user.web.cern.ch/public/en/LHC/CMS-en.html.

[18] Lhcb experiment, 2008. URL http://user.web.cern.ch/public/en/LHC/LHCb-en.html.

[19] The ATLAS Collaboration. The atlas experiment at the cern large hadron collider. *JINST*, 3, August 2008.

[20] The ATLAS Collaboration. Atlas detector and physics performance, May 1999. Technical Design Report.

[21] Jacob Groth-Jensen. *Luminosity determination and simulation of the LUCID detector at the ATLAS experiment.* PhD thesis, Lund University, 2010.

[22] The ATLAS Collaboration. The atlas simulation infrastructure. *Eur.Phys.J.*, C, 2010.

[23] The ATLAS Collaboration. *Computing Technical Design Report*, 2005. URL http://atlas-proj-computing-tdr.web.cern.ch/atlas-proj-computing-tdr/Html/contents.html.

[24] J.M et al. Butterworth. *Multiparton interactions in photoproduction at HERA*, 1996. URL http://arxiv.org/abs/hep-ph/9601371. JIMMY Information.

[25] G. Corcella et al. *HERWIG 6.5*, 2001. URL http://hepwww.rl.ac.uk/theory/seymour/herwig/0011363.ps.

[26] J. et al. Allison. *Geant4 developments and applications*, 2006. URL http://ieeexplore.ieee.org/xpls/abs_all.jsp?isnumber=33833&arnumber=1610988&count=33&index=7. General information at http://geant4.cern.ch/index.shtml.

[27] Geant4 physics lists, 2011. URL http://geant4.cern.ch/support/proc_mod_catalog/physics_lists/physicsLists.shtml.

[28] Bertini cascade, geant4, 2006. URL http://geant4.web.cern.ch/geant4/support/proc_mod_catalog/models/hadronic/BertiniCascade.html.

[29] The ATLAS Collaboration. The simulation principle and performance of the atlas fast calorimeter simulation fastcalosim. ATLAS Public Note, ATL-PHYS-PUB-2010-013, October 2010.

[30] Tadashi Maeno on behalf of PANDA team and ATLAS collaboration. Panda: Distributed production and distributed analysis system for atlas. *J. Phys.*, 119(6), 2008. URL http://iopscience.iop.org/1742-6596/119/6/062036/.

[31] The ATLAS Collaboration. Electrons and photons, 2009. Expected performance of the ATLAS Experiment, Detector, Trigger and Physics.

[32] The ATLAS Collaboration. The atlas experiment at the cern large hadron collider, 2008.

[33] Wong Ming Liang. Supersymmetric searches in the 2-electron channel. Master's thesis, Lund University, February 2012.

[34] Matteo Cacciari, Gavin P. Salam, and Gregory Soyez. The anti-kt jet clustering algorithm. April 2008. URL http://arxiv.org/abs/0802.1189.

[35] The ATLAS Collaboration. Muon performance public figures from simulation, June 2009. URL https://twiki.cern.ch/twiki/bin/view/AtlasPublic/MuonPerformancePublicPlotsSimulation. Figure 4.

[36] Douglas William Schouten. *JET ENERGY CALIBRATION IN ATLAS*. PhD thesis, University of British Columbia, 2004.

[37] F. Ahles and B. Meirose. Studying suppression of beam-induced and cosmic background to physics analyses. ATLAS Internal Note, March 2010.

[38] The ATLAS Collaboration. Performance of missing transverse momentum reconstruction in atlas with 2011 proton-proton collisions at $\sqrt{s} = 7$ tev. ATLAS-CONF-2012-101, July 2012.

[39] The ATLAS Collaboration. Atlas event displays from papers: Search for a heavy neutral particle decaying into an electron and a muon using 1 fb-1 of atlas data (15 september 2011), 2011. URL https://twiki.cern.ch/twiki/bin/view/AtlasPublic/EventDisplayPapers#Search_for_a_heavy_neutral_parti.